PHOTOLUMINESCENCE OF CHROMIUM IN GALLIUM OXIDE AND ALUMINUM GALLIUM OXIDE UNDER PRESSURE

By

LAUREN MARGARET BARMORE

A dissertation submitted in partial fulfillment of
the requirements for the degree of

DOCTOR OF PHILOSOPHY

WASHINGTON STATE UNIVERSITY
Department of Physics and Astronomy

JULY 2023

To the Faculty of Washington State University:

The members of the Committee appointed to examine the dissertation of LAUREN MARGARET BARMORE find it satisfactory and recommend that it be accepted.

Matthew McCluskey, Ph.D., Chair

Yogendra Gupta, Ph.D.

John McCloy, Ph.D.

ACKNOWLEDGMENT

Stress and pressure are phenomena with which most grad students are intimately familiar. However, I had the somewhat more rare privilege of studying stress and pressure for my dissertation research – focusing solely on the mechanical definitions of these terms, of course. I would like to extend my sincere gratitude to the following people who helped me complete my PhD:

- My advisor Matt McCluskey for his mentorship, guidance, and support, and for sharing his knowledge and experience throughout the course of my degree.
- My committee members Dr. Gupta and John McCloy for their insightful contributions to this work.
- Anya Guy for DAC and GSAS training and heptane XRD measurements.
- Violet Poole and Jesse Huso at Klar Scientific for their knowledge and assistance with PL mapping.
- Jani Jesenovec and Benjamin Dutton for crystal growth and annealing.
- Cassandra Remple for gallium oxide temperature PL measurements and ambient PL and PLE.
- REU summer students Ben Whitfield and Fiona McLary White for FTIR media calibrations.
- My current and former lab mates, especially Cassi, Syeed, Chris, Maca, and Julie and Travis, Pritha, and Chelsea, for assisting with experiments and training and for their companionship during long days (and nights) in the lab.

- The physics and ISP administrative staff who make all things possible – special thanks to Robin, Andrea, Paula, Chelsea, and Sheila.
- My fellow grad students and the Physicists for Inclusion in Science group for their support and, at times, commiseration.
- My family, friends, and teammates for their encouragement and love over the past six years, particularly my parents who always supported me in pursuing my dream.
- My fiancé Mitch, who has been unwaveringly by my side for all of this.
- And my dog Soup, who has been by my feet for most of this.

This dissertation is based upon work supported by the U.S. Department of Energy, National Nuclear Security Administration under Award DE-NA0003957. Crystal growth was supported by Air Force Office of Scientific Research under award number FA9550-21-1-0078 monitored by Dr. Ali Sayir. Additional support was provided by the U.S. Department of Energy, Office of Basic Energy Sciences, Division of Materials Science and Engineering under Award No. DE-FG02-07ER46386. This research used resources of the Advanced Light Source, which is a DOE Office of Science User Facility under contract no. DE-AC02-05CH11231, beamline 12.2.2, with assistance from Katherine Armstrong and Martin Kunz.

PHOTOLUMINESCENCE OF CHROMIUM IN GALLIUM OXIDE AND ALUMINUM GALLIUM OXIDE UNDER PRESSURE

Abstract

by Lauren Margaret Barmore, Ph.D.
Washington State University
July 2023

Chair: Matthew McCluskey

This work examines the effects of pressure and temperature on single crystals of Cr-doped gallium oxide (β-Ga_2O_3:Cr^{3+}) and aluminum gallium oxide [$(Al_{0.1}Ga_{0.9})_2O_3$, called AGO] by measuring the wavelength shift and intensity of the spectral R lines.

R lines for both Ga_2O_3 and AGO showed a redshift with increasing temperature. At low temperatures, the R_1 line intensity is dominant due to thermal depopulation of the R_2 line. At temperatures greater than 50 K, the R_2/R_1 intensity ratio is strongly affected by nonradiative recombination. In Ga_2O_3, the nonradiative contribution is thermally activated, which results in strong emission at low temperatures, particularly for R_1. AGO has smaller thermal activation barriers, possibly due to the increased disorder of the alloy which provides more nonradiative recombination pathways.

Photoluminescence (PL) spectra of these materials were collected from samples in diamond anvil cells at pressures up to 9 GPa. The response of the Cr^{3+} R lines in β-Ga_2O_3 to hydrostatic pressure showed significant differences from ruby (Al_2O_3:Cr^{3+}). The R_1-R_2 splitting,

which arises due to the crystal field and spin-orbit coupling, is larger in β-Ga_2O_3 and increases further with applied pressure. A similar effect was observed in AGO. However, the R_1 line in AGO shows a smaller shift versus pressure. X-ray diffraction (XRD) measurements of AGO indicate that its equation of state is similar to that of β-Ga_2O_3. Nonradiative recombination contributes significantly to the pressure-dependent intensity of the R lines in both β-Ga_2O_3:Cr^{3+} and AGO.

β-Ga_2O_3:Cr^{3+} and AGO were examined under nonhydrostatic conditions by using mineral oil as a pressure-transmitting medium, which is nonhydrostatic above ~2.5 GPa. Similar to the case in ruby, the R_1 line is much more sensitive to nonhydrostatic stress than R_2. Spatially resolved PL of a β-Ga_2O_3:Cr^{3+} sample at 8 GPa in mineral oil showed significant variations in the R_1 emission wavelength across the sample. A sample under hydrostatic pressure, in contrast, showed very homogenous emission wavelengths. These results suggest that the R_1 line of β-Ga_2O_3:Cr^{3+} could serve as a sensitive indicator of nonhydrostatic stress, while the R_2 line is insensitive to these perturbations.

As part of this work, the hydrostatic limits of mineral oil and heptane were established, enabling their use as pressure-transmitting media. From synchrotron XRD experiments, a solid-to-solid phase transition was discovered in heptane with onset at 1.5 GPa. The phase transition resulted in discontinuous shifts in vibrational peaks in the IR spectra.

TABLE OF CONTENTS

LIST OF TABLES

LIST OF FIGURES

CHAPTER ONE: INTRODUCTION

1.1 Subject of this work

This work examines the temperature and pressure dependent optical properties of β-Ga_2O_3:Cr^{3+} and $(Al_{0.1}Ga_{0.9})_2O_3$ (AGO). Ga_2O_3 is an ultra-wide bandgap semiconductor that is a promising candidate for use in high power electronics. AGO is an alloy of Ga_2O_3 and Al_2O_3, with the benefit of a tunable bandgap depending on the percentage of Al incorporation. In order for these materials to be used in the development of future semiconductor devices, we need to understand the role of defects and impurities in influencing their electronic and optical properties.

This work focuses on the dopant chromium (Cr^{3+}) as a model impurity in order to compare the pressure dependent effects in Ga_2O_3 and AGO with those of the well-studied ruby (Al_2O_3:Cr^{3+}). The Cr^{3+} emission intensity may be used as a probe of *n*-type conductivity to provide insight into the electrical properties of these materials.[1] As 3+ is the optically active charge state of Cr ions, the stronger luminescence typically observed in insulating samples is a result of a Fermi level shift towards the middle of the bandgap, which makes Cr^{3+} the energetically favorable charge state.[1,2] In this work we present the results of photoluminescence spectroscopy and x-ray diffraction of β-Ga_2O_3:Cr^{3+} and AGO at ambient conditions, low temperatures, and elevated pressures. Complementary studies were also conducted on pressure-transmitting media for use in diamond anvil cell experiments, including X-ray diffraction of heptane under pressure.

The structure of this dissertation is as follows: Chapter 1 introduces the basics of semiconductors and reviews the present state of literature on gallium oxide under pressure.

Chapter 2 details the experimental methods and analysis techniques used in this work. Chapter 3 describes photoluminescence spectroscopy on gallium oxide and AGO as a function of temperature. Chapter 4 covers the experiments on gallium oxide and AGO under pressure and discusses the results. Chapter 5 contains the work on pressure-transmitting media, including results and discussion of heptane under pressure. Chapter 6 summarizes the findings and conclusions from this work and proposes directions for future work.

1.2 Introduction

Power electronic systems are ubiquitous in our world and found in virtually every electronic device. Rather than processing signal and data as in computer chips, power electronic systems process electrical energy. These devices range from a low power AC/DC converter in a phone charger to gigawatt-scale high voltage power transmission systems used in electrical grids.[3]

Before the advent of semiconductors, mercury arc valves – high-vacuum and gas-filled tubes that function as diode thermionic rectifiers – were widely used in power electronics.[3,4] These vacuum devices have since been replaced by solid-state semiconductor-based devices, which have improved significantly in voltage and current handling capacity.[5] Future improvements in high power electronics depend on scientists gaining a greater understanding of the materials used in these devices. One such material is gallium oxide, the characterization of which is the subject of this dissertation.

1.3 Semiconductors

Semiconductors are defined by their unique electrical conductivity behavior. A semiconductor is a material with tunable conductivity greater than that of an insulating material, but not high enough to be considered a conductor. Typical electrical resistivities for semiconductors are between 10^{-2} and 10^{-9} ohm-cm.[6] The electronic structure of a semiconductor features electron bands of allowed states with a bandgap of forbidden states. Commonly used semiconductors are single elements, such as silicon and germanium, binary compounds, such as gallium arsenide (GaAs) and gallium nitride (GaN), and oxides such as zinc oxide (ZnO) and gallium oxide (Ga_2O_3), the subject of this work.

Characterization of semiconductors is particularly important for improving advanced materials. Determining the properties of a novel semiconductor material is required before it can be incorporated into devices that can compete with state-of-the-art technologies.

1.3.1 Electrical and optical properties

According to the Pauli exclusion principle, discrete quantum states for electrons can be empty or occupied by one electron only. If a band of states is filled with electrons, it is inert since no electrons can pass through, and the material is insulating. Electrical conductivity occurs when electrons can flow by moving between unfilled states.

A defining feature of semiconductors is the bandgap. The bandgap is the energy needed to excite an electron from a bound state to a higher energy state where it can conduct electricity. Electrons occupy a group or band of states called the valence band, where they reside in covalent bonds. The conduction band is a group of unoccupied higher energy states above the valence band, separated by the bandgap (E_g), in which no states are available (Figure 1.1) Electrons in the conduction band are not bound to an atom and are free to conduct electricity. Electrons can be excited to the conduction band by raising the temperature or by an incident photon with energy greater than the bandgap ($hv \geq E_g$). When electrons transition to the conduction band, they leave behind a hole – the absence of an electron that acts as a quasiparticle with positive charge.

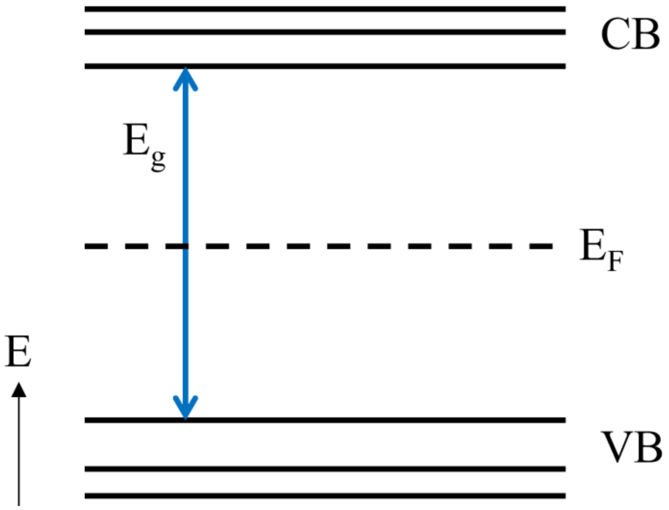

Figure 1.1: Conduction band (CB), valence band (VB) and bandgap (E_g), with the Fermi level (E_F) in between.

In an ideal semiconductor at 0 K, the valence band is entirely filled with electrons and the conduction band has no electrons. If an electric field is applied, the semiconductor is insulating since there are no available states in the valence band and no electrons can move to conduct electricity. At zero temperature, the states below the Fermi energy (E_F) are completely filled, and the states above are completely empty. At a higher temperature, some electrons are thermally excited into the conduction band, where they are free to conduct electricity. The free carrier concentration refers to the amount of available electrons or holes that can move freely.

A pure (intrinsic) semiconductor can absorb photons with energy higher than the bandgap ($h\nu \geq E_g$). For example, silicon has a bandgap of 1.1 eV and can absorb near-IR, visible, and UV light (energy > 1.1 eV). Gallium oxide has a bandgap of 4.8 eV, so it cannot absorb visible light. This is why silicon appears black while gallium oxide appears transparent.[7] The absorbed photons excite electrons from the valence band to the conduction band and leave behind a hole in the valence band (Figure 1.2).

An electron in an excited state can transition back to a lower level by recombining with a hole and emitting a photon through radiative decay. This process is known as photoluminescence (PL). There are also mechanisms which allow for nonradiative recombination, which do not emit light. The energy in these cases is typically dissipated in the form of phonons (lattice vibrations of a solid).[7] Nonradiative recombination is usually an undesirable effect in semiconductors used in devicessince it leads to lower light-generation efficiency and increased heating in lasers and light emitting diodes.[8] PL spectroscopy by definition only measures radiative decay.

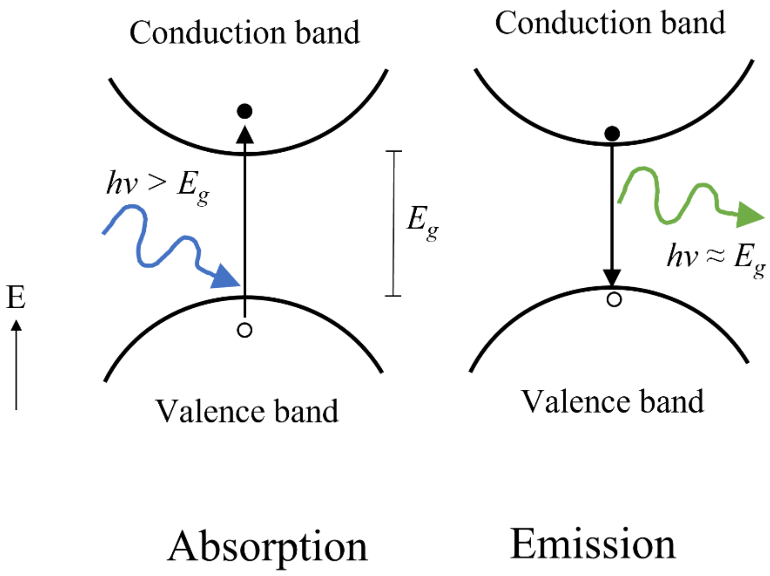

Figure 1.2: Absorption and emission processes.

Electronic band structure can be plotted as energy versus momentum (E versus wave vector k, where photon momentum is $p = \hbar k$). A semiconductor has a direct bandgap when the valence band maximum and the conduction band minimum are both located at the same k value (often zero). In some semiconductors like silicon, the conduction band minimum occurs at a nonzero k value. This is an example of an indirect bandgap. An incident photon can only change the energy of an electron, not its momentum, so in order for an electron to be excited to the conduction band across an indirect bandgap, interaction with a phonon is also required.[7] Direct bandgap semiconductors require only photons to excite an electron, so the process is more efficient. When a photon is absorbed by an electron, the electron's energy is increased by the photon energy (hv). A phonon will change the electron energy by $\hbar\Omega$ and its momentum by the phonon momentum K.[9] Recombination of an electron and a hole also requires a phonon in indirect bandgap semiconductors, so these are not as efficient at emitting light as a direct gap semiconductor.

1.3.2 Crystal structure and growth

A crystal is a lattice of atoms at regular repeated distances that continues indefinitely. In reality, crystals are not infinite, but their surfaces and boundaries can be ignored when considering bulk properties. The unit cell is the repeated structure block in a crystal and the lattice constants are the lengths of the edges of the unit cell. Directions within the unit cell point from the origin in a direction [*hkl*]. The class of all directions equivalent to [*hkl*] by symmetry is written as <*hkl*>. The Miller indices *h*, *k*, and *l* describe the atomic plane perpendicular to the direction [*hkl*], denoted (*hkl*). The class of all equivalent planes by symmetry are written as {*hkl*}.[7] A simple example is a simple cubic crystal, in which the unit cell has one atom at the origin (the other atoms belong to neighboring cells). In Figure 1.3, the direction [111] and the plane (001) are shown.

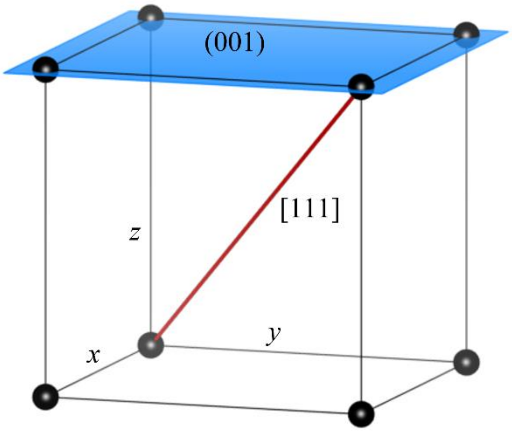

Figure 1.3: Simple cubic structure.

There are several techniques that can be used to grow bulk and thin film semiconductor crystals. The materials used in this work were grown at the Washington State University Institute for Materials Research using the Czochralski method, so only this technique will be discussed here. In this method, a melt of the constituent components is contained in a crucible and heated. A seed crystal of known orientation is dipped into the melt. Then the seed crystal is slowly drawn out of the melt as new material solidifies onto the seed in a larger single crystal. The seed is rotated to maintain cylindrical symmetry, and the heat flow is controlled to determine the crystal growth rate and diameter.[6]

1.3.3 Defects and dopants

In pure semiconductors, electrons in the conduction band may be donated by native defects, not an outside source. However, the conducting properties of semiconductors can be altered by deliberately introducing impurities into the crystal in a process known as doping.

A donor is an impurity that has more valence electrons than the atom it replaces, so it "donates" a free electron to the conduction band. Semiconductors that have more electrons than holes are called *n*-type since electrons have negative charge. An acceptor is an impurity that has fewer valence electrons than the atom it replaces. An acceptor accepts an extra electron from the valence band, leaving behind a hole. Semiconductors that have holes as a majority of charge carriers are called *p*-type, because holes have a positive charge. A semiconductor with electrical conduction dominated by either donor or acceptor dopants is called an extrinsic semiconductor, since the conductivity relies on atoms not native to the crystal.[6]

Doping a semiconductor changes the Fermi energy. In an *n*-type semiconductor, the Fermi level is near the conduction band minimum, so there is a high likelihood that conduction band levels will be occupied by electrons. In a *p*-type semiconductor, the Fermi level is near the valence band maximum, so there is a high density of holes in the valence band.

Extrinsic defects such as dopants or impurities involve atoms that are not present in the pure crystal. Impurities can occupy substitutional sites, where they replace a host atom in the crystal lattice, or interstitial sites between atomic sites. Intrinsic or native defects only involve the atoms present in the ideal crystal. A few examples of native defects include the lattice vacancy, where a host atom is missing, and self-interstitial, where a host atom is located between atomic sites in the crystal. In compound semiconductors, an antisite defect occurs when an atom is located on the site of a different host atom, i.e. in GaAs when As is located on a Ga site.[7] In addition to these point defects that affect a single atom or two, there are also extended defects. Examples of extended defects include line dislocations, where the lattice is disrupted by a series of atoms out of place, and screw dislocations, where shear deformation causes a spiral of atoms around the dislocation line.[10]

It is impossible to grow a perfectly pure semiconductor – impurities are always present in the crystal, whether by design or accident. Thus “undoped” semiconductors are often referred to as unintentionally doped, or UID. When growing using the Czochralski method, dopants can be incorporated uniformly into the crystal by adding the dopant in pure form to the melt.

Useful electrical properties in a semiconductor can be tuned through doping or applying light or electric fields. An interface between two differently doped regions creates a semiconductor junction. The behavior of charge carriers (electrons or holes) at a junction forms the basis of most modern electronic devices such as diodes and transistors.

1.4 Stress and anisotropic elasticity

In a crystal, properties depend on relations between measurable quantities, which may have both magnitude and direction. For example, the elasticity of a crystal depends on the deformation and mechanical stress applied, both of which have a magnitude and direction. Thus, a physical property of a crystal may depend on the direction in which it is measured. Crystals may be anisotropic, and we use tensors to mathematically define their properties.[11]

Stress is defined as force per unit area and can be compressive (squeezing) or tensile (stretching). Stress is measured in gigapascals (1 GPa = 10^9 Pa). The Cauchy stress tensor σ is the force applied to an infinitesimal cube within a solid and defines the direction of the force as well as the orientation of the face the force is applied to. The Cauchy stress tensor is a second rank tensor that completely defines the stress state at a point inside the material.[12]

For coordinates x_1, x_2, x_3, the Cauchy stress tensor (Figure 1.4) is written as

$$\begin{bmatrix} \sigma_{11} & \sigma_{12} & \sigma_{13} \\ \sigma_{21} & \sigma_{22} & \sigma_{23} \\ \sigma_{31} & \sigma_{32} & \sigma_{33} \end{bmatrix} \tag{1}$$

In order to have no net torque on the solid, the terms across the diagonal must be equal ($\sigma_{ij} = \sigma_{ji}$), so there are six independent terms in the stress tensor.

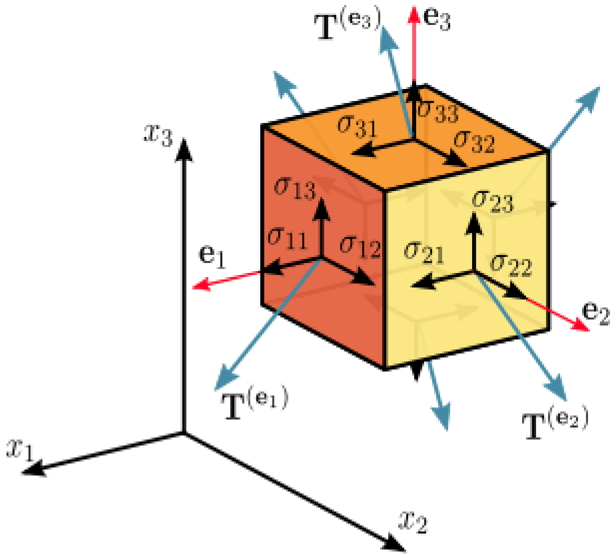

Figure 1.4: Components of the Cauchy stress tensor.[13]

Pressure or hydrostatic stress is a special case of stress in which the compressive or tensile stresses on all surfaces are equal. The off-diagonal (shear) terms are zero and the diagonal terms are all equal. This is the stress experienced by a material in a fluid where it is being squeezed equally from all sides. Hydrostatic pressure causes volume compression but no deformation of the unit cube (Figure 1.5) for a linear elastic material with isotropic elastic constants. Hydrostatic loading is preferred in many high pressure physics studies for predictable material behavior and straightforward stress calculations.

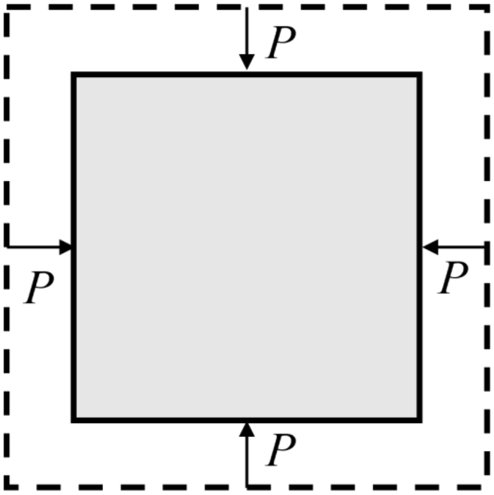

Figure 1.5: Hydrostatic pressure causes volume compression of the material.

When the diagonal terms in the stress tensor are not equal or there are non-zero shear terms present, the stress is said to be nonhydrostatic. Nonhydrostatic phenomena can be studied in specific simplified cases such as uniaxial strain as in inertially confined shock loading.[14,15] However, nonhydrostatic conditions in uncontrolled loading, as in a diamond anvil cell without a hydrostatic pressure-transmitting medium, can lead to unpredictable material behavior.

1.4.1 Hooke's law

Strain is a measure of the deformation of a material as a response to stress. In linear elasticity, the strain induced in a solid is proportional to the stress applied. Since both stress and strain are second rank tensors with nine terms, the proportionality constants are expressed as a fourth rank tensor called the stiffness tensor with 81 terms. The generalized Hooke's law is[11]

$$\sigma_{ij} = c_{ijkl}\,\varepsilon_{kl} \tag{2}$$

where we are using the Einstein summation convention. The inverse of the stiffness tensor is the compliance tensor s, such that $\varepsilon_{ij} = s_{ijkl}\,\sigma_{kl}$. Since stress and strain are symmetric tensors, they are commonly expressed as just six matrix elements. The stress and strain tensors can be expressed using the matrix notation

$$\begin{bmatrix}\sigma_{11}\\ \sigma_{22}\\ \sigma_{33}\\ \sigma_{23}\\ \sigma_{13}\\ \sigma_{12}\end{bmatrix} \equiv \begin{bmatrix}\sigma_{1}\\ \sigma_{2}\\ \sigma_{3}\\ \sigma_{4}\\ \sigma_{5}\\ \sigma_{6}\end{bmatrix} \quad \text{and} \quad \begin{bmatrix}\varepsilon_{11}\\ \varepsilon_{22}\\ \varepsilon_{33}\\ \varepsilon_{23}\\ \varepsilon_{13}\\ \varepsilon_{12}\end{bmatrix} \equiv \begin{bmatrix}\varepsilon_{1}\\ \varepsilon_{2}\\ \varepsilon_{3}\\ \tfrac{1}{2}\varepsilon_{4}\\ \tfrac{1}{2}\varepsilon_{5}\\ \tfrac{1}{2}\varepsilon_{6}\end{bmatrix} \tag{3}$$

The ½ terms in the shear strain components come from the symmetry across the diagonal in the tensor form, since shear components always appear together in pairs:[12]

$$\sigma_{ij} = c_{ij12}\,\varepsilon_{12} + c_{ij21}\,\varepsilon_{21} = 2c_{ij12}\,\varepsilon_{12} \rightarrow \sigma_{i} = c_{i6}\,\varepsilon_{6}$$

The symmetry of the Cauchy stress tensor and Hooke's law implies that $c_{ijkl} = c_{jikl}$. Similarly, the symmetry of the infinitesimal strain tensor implies that $c_{ijkl} = c_{ijlk}$. This reduces the number of independent elastic constants from 81 to 36. Since Hooke's law can be derived from the strain energy density functional and the order of differentiation is arbitrary, this implies that $c_{ijkl} = c_{klij}$. Thus, there are only 21 unique components in the stiffness tensor[12] and the generalized Hooke's law may be written

$$\begin{bmatrix}\sigma_{11}\\ \sigma_{22}\\ \sigma_{33}\\ \sigma_{23}\\ \sigma_{13}\\ \sigma_{12}\end{bmatrix} = \begin{bmatrix} c_{1111} & c_{1122} & c_{1133} & c_{1123} & c_{1131} & c_{1112}\\ c_{1122} & c_{2222} & c_{2233} & c_{2223} & c_{2231} & c_{2212}\\ c_{1133} & c_{2233} & c_{3333} & c_{3323} & c_{3331} & c_{3312}\\ c_{1123} & c_{2223} & c_{3323} & c_{2323} & c_{2331} & c_{2312}\\ c_{1131} & c_{2231} & c_{3331} & c_{2331} & c_{3131} & c_{3112}\\ c_{1112} & c_{2212} & c_{3312} & c_{2312} & c_{3112} & c_{1212} \end{bmatrix} \begin{bmatrix}\varepsilon_{11}\\ \varepsilon_{22}\\ \varepsilon_{33}\\ \varepsilon_{23}\\ \varepsilon_{13}\\ \varepsilon_{12}\end{bmatrix} \tag{4}$$

or using the two suffix notation $\sigma_i = c_{ij}\,\varepsilon_j$,

$$\begin{bmatrix}\sigma_1\\\sigma_2\\\sigma_3\\\sigma_4\\\sigma_5\\\sigma_6\end{bmatrix}=\begin{bmatrix}c_{11}&c_{12}&c_{13}&c_{14}&c_{15}&c_{16}\\c_{21}&c_{22}&c_{13}&c_{24}&c_{25}&c_{26}\\c_{31}&c_{32}&c_{33}&c_{34}&c_{35}&c_{36}\\c_{41}&c_{42}&c_{43}&c_{44}&c_{45}&c_{46}\\c_{51}&c_{52}&c_{53}&c_{54}&c_{55}&c_{56}\\c_{61}&c_{62}&c_{63}&c_{64}&c_{65}&c_{66}\end{bmatrix}\begin{bmatrix}\varepsilon_1\\\varepsilon_2\\\varepsilon_3\\½\varepsilon_4\\½\varepsilon_5\\½\varepsilon_6\end{bmatrix} \quad (5)$$

It should be noted that in order to transform these equations to a different axis, it is necessary to go back to the full tensor notation, for example[11]

$$c'_{ijkl} = a_{im}a_{jn}a_{ko}a_{pn}c_{mnop} \quad (6)$$

where a_{im} is the cosine of the angle between the new axis x'_i and the old axis x_m.

Equation 5 is the most general form of Hooke's law, but symmetry relations in higher-symmetry crystals further reduce the number of independent elastic constants. For example, a cubic crystal has only three independent elastic constants.[11]

For isotropic materials, symmetry relations yield only two independent elastic constants, so the compliance matrix becomes[12]

$$\begin{bmatrix}s_{11}&s_{12}&s_{12}&0&0&0\\s_{12}&s_{11}&s_{12}&0&0&0\\s_{12}&s_{12}&s_{11}&0&0&0\\0&0&0&2(s_{11}-s_{12})&0&0\\0&0&0&0&2(s_{11}-s_{12})&0\\0&0&0&0&0&2(s_{11}-s_{12})\end{bmatrix} \quad (7)$$

Hooke's law for isotropic materials can be expressed in terms of the more familiar elastic moduli: Young's modulus *E*, bulk modulus *K*, shear modulus *G*, and Poisson's ratio *v*. These are related to the compliance components by the following relations:[11,12]

$$s_{11}=\frac{1}{E},\ s_{12}=\frac{-\nu}{E},\ 2(s_{11}-s_{12})=\frac{1}{G} \quad (8)$$

and the four constants are related by

$$E = 2G(1 - \nu) = 3K(1 - 2\nu) \tag{9}$$

Then the generalized Hooke's law for an isotropic linear elastic material can be written[12]

$$\varepsilon_{ij} = \frac{1}{E}\left[\sigma_{ij}(1 + \nu) - \nu\delta_{ij}\sum_k \sigma_{kk}\right] \tag{10}$$

where δ_{ij} is the Kronecker delta function.

Young's modulus *E* describes the material's strain response to uniaxial stress in the direction of loading. The bulk modulus *K* describes the material's response to uniform hydrostatic pressure, and the shear modulus *G* describes the material's response to shear stress. *E*, *K*, and *G* are measured in GPa and must be positive. Poisson's ratio, which measures the deformation perpendicular to the loading direction, must be between 0 and 0.5 (unitless) for an homogeneous isotropic linear elastic material.[11] Sometimes it is convenient to approximate anisotropic crystals as isotropic in order to measure the bulk elastic constants.[16]

1.5 Gallium oxide

Gallium oxide (Ga_2O_3) is a semiconductor that has been gaining attention due to its potential as a material for high power electronic applications.[17,18] Past research on high voltage power switching systems has been focused on silicon carbide or gallium nitride.[19–21] Gallium oxide has promising properties such as high breakdown voltage, tunable conductivity, and low cost melt-based bulk growth[22] that make it a candidate to replace the semiconductors currently in use, but its properties need to be better understood in order to realize that potential. That possibility motivated this research, which focuses on characterization of gallium oxide under pressure. Specifically, this work examines the optical spectrum of chromium dopants in gallium oxide and aluminum-gallium oxide alloy.

1.5.1 Properties

Gallium oxide is classified as an ultrawide bandgap semiconductor with a direct bandgap of 4.8 eV, which leads to a high breakdown field of 8.7 MV/cm.[17] With the addition of extrinsic dopants such as Si, Zr, Hf, and Ge, Ga_2O_3 can be made *n*-type conducting for use in field effect transistor (FET) devices.[18,23] Dopants such as Fe, Mg, N, and Zn behave as deep acceptors and make Ga_2O_3 semi-insulating.[17,18,24–27]

Ga_2O_3 can exist in many phases ($\alpha, \beta, \gamma, \delta, \varepsilon$)[28] and this work focuses on the β phase, which is the stable phase at room temperature and pressure. β-Ga_2O_3 has a monoclinic crystal structure (space group $C2/m$, Figure 1.6).[29] The Ga atoms exist in either a distorted octahedral Ga(II) arrangement bound to six neighboring O atoms or a tetrahedral Ga(I) arrangement bound to four O atoms.[17] The lattice parameters at ambient conditions are a = 12.233 Å, b = 3.038 Å, c = 5.807 Å, β = 103.821°, with cell volume V = 209.56 Å^3 and density d = 5.941 g/cm^3.[30] Unless otherwise noted in the remainder of this work, Ga_2O_3 will refer to β-Ga_2O_3.

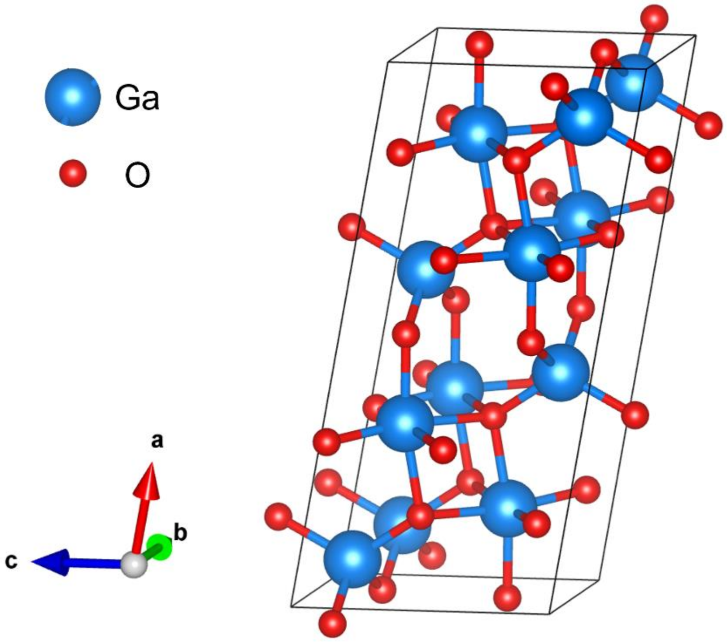

Figure 1.6: Monoclinic crystal structure of β-Ga_2O_3*. Figure made with VESTA.*[31]

In recent years, gallium oxide has become an exciting material in the field of semiconductors. Research on Ga_2O_3 generally falls into the categories of growth, characterization, or devices. Thin films can be produced by metal-organic chemical vapor deposition[32] and other deposition methods[33–35]. Bulk gallium oxide crystals can be grown with many techniques as well including float zone,[36] edge defined film fed,[37] vertical gradient freeze[2,38] or Czochralski.[38–40] Gallium oxide monoclinic single crystals used in this work were grown at the Washington State University Institute for Materials Research by the McCloy research group using the Czochralski method.[41] Cr-doped Ga_2O_3 was grown with Cr concentration batched at 0.05 at.% from a 3N7 (99.97%) purity Cr_2O_3 precursor and 5N

(99.999%) purity Ga_2O_3. Glow discharge mass spectrometry (GDMS) indicated that the incorporation of Cr was 7×10^{19} atoms/cm^3.[42]

Gallium oxide characterization has been performed to understand the properties of this material, including luminescence,[43,44] band structure,[45] and defect level modeling for many dopants.[26,27,46–49] Device research has shown the high breakdown voltage, wide bandgap, and inexpensive growth make gallium oxide an ideal material for power electronics. Devices such as metal-semiconductor field-effect transistors (MESFETs) and Schottky barrier diodes have been created from gallium oxide.[18]

1.5.2 Chromium

Ga_2O_3 can be doped with the optically active ion Cr^{3+}, which is also a common contaminant.[50] Cr^{3+} has the d^3 electronic configuration and preferentially occupies the Ga(II) octahedral site in Ga_2O_3.[51,52] Crystal field splitting from the distorted octahedral site results in multiple non-degenerate energy levels, which give rise to red luminescence[53,54] commonly called *R* lines due to their presence in the well-studied ruby spectrum.

β-Ga_2O_3:Cr^{3+} has defect absorption bands at 430 nm (2.88 eV) and 600 nm (2.07 eV), which correspond to the to $^4A_2 \rightarrow {}^4T_1$ and $^4A_2 \rightarrow {}^4T_2$ transitions, respectively.[1,44,55–57] The emission spectrum consists of two sharp peaks, the R_1 line at 696 nm and the R_2 line at 689 nm, and a broad emission at 710 nm. The sharp *R* lines are due to $^2E \rightarrow {}^4A_2$ transitions, while the broad peak arises from the $^4T_2 \rightarrow {}^4A_2$ transition (Figure 1.7).[1,55,58–62] The absorption and emission spectra are similar to ruby (Al_2O_3:Cr^{3+}),[53,63,64] which has R_1 and R_2 lines at 694 and 693 nm (1.787 and 1.789 eV).[53,58,65,66] Ga_2O_3 has a larger R_1-R_2 splitting than ruby due to differences in spin-orbit coupling and lower symmetry fields.[51,53] The luminescence of β-Ga_2O_3:Cr^{3+} has been studied as a candidate for tunable lasers.[60,62]

Photoluminescence spectroscopy of the Cr^{3+} emissions as a function of temperature and pressure provides information about the electronic population, temperature, and pressure dependence of the energy levels. Changes in peak parameters such as wavelength, intensity, or width can also provide insight into the response of β-Ga_2O_3:Cr^{3+} at elevated temperatures and pressures.[67–69] This response has been thoroughly studied for Cr^{3+} in ruby.[63,70–78] In this work, the behavior of Cr^{3+} in Ga_2O_3 was investigated.

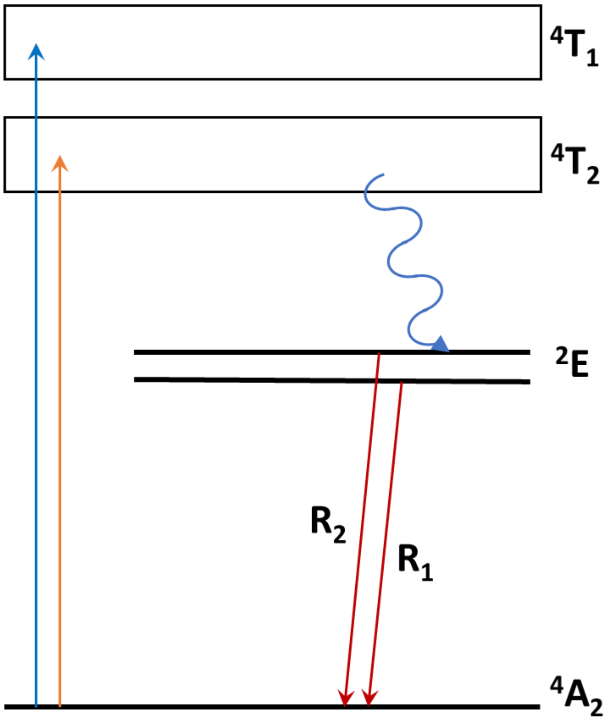

Figure 1.7: Electronic transitions in β-Ga_2O_3:Cr^{3+} *that result in R line luminescence.*

1.5.3 Gallium oxide under pressure

In ruby, the *R* lines redshift with increasing pressure and are used as a calibrant in high pressure experiments.[79–82] The chromium lines in gallium oxide powder have also been found to shift linearly with pressures up to 5 GPa at low temperature (85 K), and gallium oxide was proposed as an alternative high pressure calibrant for cryogenic temperatures.[69] The Cr^{3+} emission was later used to monitor pressure in a diamond anvil cell at 85 K.[83] Density-functional theory (DFT) simulations on orthorhombic Ga_2O_3 found that uniform strain decreases the lattice constants and increases the bandgap.[84]

The 13 elastic constants of monoclinic gallium oxide have been found by Adachi et al. using resonant ultrasound spectroscopy and DFT.[16] These elastic constants are required to evaluate stress fields in Ga_2O_3 devices. Their results reveal unusual elastic properties including strong anisotropy in Young's modulus ($E_1 \ll E_2$, E_3), longitudinal elastic moduli ($C_{11} \ll C_{22}$, C_{33}), and shear elastic moduli ($C_{44} \ll C_{55}$, C_{66}). Also reported were Poisson's ratios exceeding 0.5 (ν_{21} and ν_{31}) and nearly zero Poisson's ratios (ν_{23} and ν_{32}). Note that although the authors refer to these elastic moduli as Young's modulus and Poisson's ratio, these moduli by definition only have meaning for isotropic materials. Similar elastic anomalies appear in θ-Al_2O_3, which has the same monoclinic structure and space group $C2/m$ as β-Ga_2O_3. Other monoclinic materials do not share these anomalous elastic properties, indicating that the higher binding energy in the tetrahedral-octahedral linkage structure present in materials with the $C2/m$ space group is responsible for the exceptional elastic anisotropy. In particular, β-Ga_2O_3 is more compressible along the a^* axis (perpendicular to the b-c plane).[16]

A phase transition from monoclinic β-Ga_2O_3 to a corundum-like α phase at high pressures has been reported, with the onset of phase change beginning at 7-20 GPa.[30,83,85,86] This transition is computationally predicted to occur at 2.6-9.5 GPa[85,87] and experimentally reported at 6.5-7 GPa[30] or 19-22 GPa.[86,88] The phase transition was reported at approximately 10 GPa in Ga_2O_3:Mn.[83] This β to α phase transition has been studied using synchrotron x-ray diffraction[30,86,88] and Raman spectroscopy.[86] One paper[89] reported a phase transition from "monoclinic α-Ga_2O_3" to "tetragonal β-Ga_2O_3" at 13 GPa, but the x-ray diffraction pattern of the starting material more closely resembled monoclinic β-Ga_2O_3 than the α phase.[86] No explanation has been given in literature for the large variation in the onset of phase transition.

1.6 Aluminum-gallium oxide alloy

A useful property of gallium oxide is the ability to tune the bandgap through alloying. One example of this is the aluminum oxide - gallium oxide alloy $(Al_xGa_{1-x})_2O_3$, referred to as AGO. Here, aluminum oxide is referred to as an alloy component instead of a dopant due to its high percentage (> 1%). β-Ga_2O_3 has a bandgap of 4.8 eV and α-Al_2O_3 has a bandgap of 8.8 eV.[90] The bandgap of AGO can thus be tuned by varying the amount of Al_2O_3.[41,91] AGO can be used in place of β-Ga_2O_3 to achieve carrier confinement, increase the bandgap, or modify the lattice parameters.[92]

Al and Ga are in the same group on the periodic table and so have the same number of valence electrons. α-Al_2O_3 has the corundum (trigonal) structure ($R\bar{3}c$)[90,92] in contrast to the monoclinic structure of β-Ga_2O_3 (space group $C2/m$). AGO is a stable semiconductor alloy despite the different ground state crystal structures of the two end members. In the monoclinic phase, two cation environments are available: the octahedral Ga(II) and tetrahedral Ga(I) sites. Only octahedrally coordinated cation sites are available in the corundum phase.[92] The monoclinic phase is energetically preferable for AGO up to 70 atomic% of Al on the cation sites.[90,92] It is energetically favorable for Al to occupy the octahedrally coordinated Ga(II) sites, although experimentally Al was shown to incorporate on the tetrahedral Ga(I) site up to 35%.[90,93,94]

The AGO crystals used in this work were grown at the Washington State University Institute for Materials Research by the McCloy research group using the Czochralski method.[41] From X-ray fluorescence (XRF), Al incorporation is 11.7 mol.% Al_2O_3 in β-Ga_2O_3 ($x = 0.117$).[93] This alloy has a bandgap of approximately 5.0 eV, and polarization-dependent light absorption was observed.[41,95] AGO used in this work was UID and had the monoclinic β-Ga_2O_3 crystal structure.

Few PL spectroscopy studies have been performed on AGO. The *R* lines have been observed in AGO crystal doped with Cr^{3+} by Chen et al.[96] This group observed crystal lattice contraction with increasing concentrations of Al^{3+}, as Al has a smaller atomic radius than Ga (Al^{3+} has 0.39 Å; coordination number (CN) = 4; 0.54 Å, CN = 6, while Ga^{3+} has 0.47 Å, CN = 4; 0.62 Å, CN = 6).[97] With increasing Al percentages, the R_1 line shifted to longer wavelength and the R_2 line shifted to shorter wavelength. This increase in *R* lines splitting is a result of the lowered crystal field symmetry[51] and was accompanied by a change in the relative intensity of the R_1 and R_2 lines. At $x = 0.8$, the alloy underwent a phase transition from the monoclinic β-Ga_2O_3 phase to the triclinic α-Al_2O_3 phase, confirmed by XRD data.[96]

Additional UV and blue emission features have been identified in the $x = 0.1$ $(Al_xGa_{1-x})_2O_3$ bulk crystal and were attributed to defects such as self-trapped holes (STHs), other dopants, or extended defects.[95] An additional channel of nonradiative decay was proposed for $(Al_xGa_{1-x})_2O_3$:Mn to account for a rapid increase in emission rates at high temperatures.[83]

1.6.1 Aluminum-gallium oxide under pressure

For sintered powder AGO in the monoclinic *β* phase under pressure in a diamond anvil cell, the low-symmetry crystal field component increased with increasing pressure, causing an increase in the *R* line splitting accompanied by a change in relative *R* line intensity.[96] The *β* to *α* phase transition was observed in $x = 0.1$ AGO powder at 14.5 GPa and at a slightly lower pressure of ~13.5 GPa for $x = 0.8$. Above the phase transition in the *α* phase, the $^2E \rightarrow {}^4A_2$ emission appears as a single *R* line.[96]

After the phase transition in both $x = 0.1$ and 0.8 samples, a new PL band appeared at 750-800 nm. Both the *R* line and the new band shift to higher wavelengths as pressure is increased, with the new band exhibiting a stronger shift. This new band is tentatively ascribed to the emission of exchange-coupled Cr^{3+} pairs under high pressure, and was not observed in β-Ga_2O_3 with no Al present.[96]

CHAPTER TWO: EXPERIMENTAL AND ANALYTICAL TECHNIQUES

This chapter describes the experimental methods and analysis techniques used in this work.

2.1 Photoluminescence Spectroscopy

2.1.1 Background

Photoluminescence (PL) is a process that occurs when a molecule or crystal absorbs an incident photon, which excites an electron to a higher energy state. When the electron returns to a lower energy level, a photon is emitted, resulting in PL.[98] Photoluminescence spectroscopy is a measurement technique in which a fixed wavelength excitation source (often a laser) irradiates a sample to stimulate PL. The emitted photons pass through a monochromator and into a detector such as a photomultiplier tube. The resulting spectrum is a plot of the luminous intensity as a function of wavelength or energy. Properties of the PL spectrum, such as peak energies and intensities, reveal intrinsic and defect properties of the studied material.[98,99]

The PL spectroscopy in this work was performed using 405 nm laser and Ocean Optics Maya 2000 Pro spectrometer. Laser light is incident on the sample after passing through a dichroic mirror. Emitted light reflects off the dichroic mirror to the spectrometer (Figure 2.1). A camera allows the user to view the position of the sample.

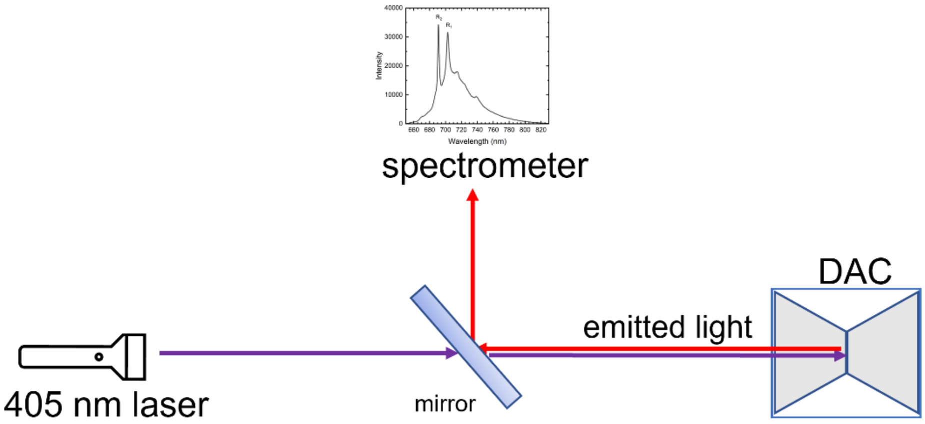

Figure 2.1: PL microscope and spectrometer.

Photoluminescence excitation (PLE) is a similar technique but instead of using a fixed wavelength excitation source as in PL, in PLE the excitation source wavelength is varied using a broadband source with a monochromator grating. The detector then measures the intensity of a single wavelength emission. PLE gives information about the excitation and absorption of the sample being studied.

PLE and low temperature PL spectra were measured by a Horiba Jobin-Yvon FluoroLog-3 spectrometer with double-grating monochromators and a photomultiplier tube. The excitation source is a broadband 450 W xenon continuous-wave gas discharge lamp. An excitation wavelength of 405 nm was selected by passing light through a monochromator. The light propagated at approximately a 30-degree angle to the (100) plane of the crystal.

2.1.2 Photoluminescence Mapping

Photoluminescence mapping is a technique used to measure the spatially resolved PL spectra of a sample across an area of the surface. A confocal laser microscope system is used to scan the sample in a raster pattern and measure the PL spectrum at each point. These spectra can then be analyzed with a custom model to fit the spectral peaks, and false-color image maps of the fitted spectra parameters can be plotted. The PL mapping in this work was performed using a Klar Scientific Mega Pro Prototype microscope equipped with a 405 nm CW laser and Ocean Optics Maya 2000 Pro spectrometer. This system is able to scan both ambient samples and samples inside a diamond anvil cell. Maps inside the diamond anvil cell used a spatial step size of 2 μm.

2.2 Fourier transform infrared spectroscopy (FTIR)

FTIR is a spectroscopic technique that measures the intensity of infrared radiation transmission as a function of frequency. This is useful for measuring free carrier absorption and local vibrational modes in semiconductors. FTIR uses interferometry based on a Michelson interferometer.[99] The infrared source beam is split by a beam splitter to reflect off both a fixed mirror and a moving mirror (Figure 2.2). The moving mirror is controlled to precisely vary the path length, and the path length difference induces a phase change in that beam. After reflection, the beams are recombined by the beam splitter and the different phases cause the beams to interfere constructively or destructively with each other, resulting in an interferogram signal. This signal passes through the sample where some of the energy is absorbed. The signal transmitted through the sample is measured by a detector. The detected interferogram signal is digitized and converted to an intensity vs wavenumber spectrum using a fast Fourier transform (FFT).

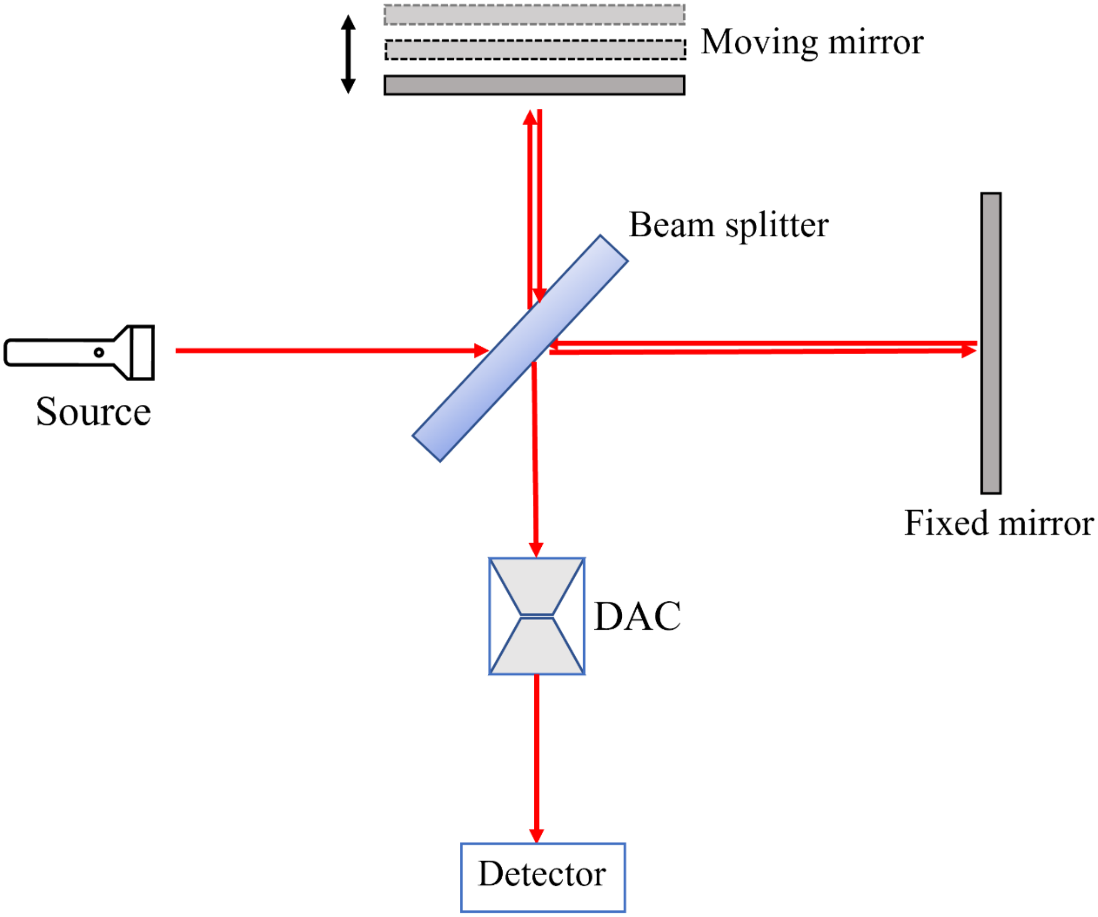

Figure 2.2: Simplified beam path of the FTIR spectrometer.

The FTIR measurements in this work were performed using a Bomem DA8 FTIR spectrometer. The infrared source is a silicon carbide globar that emits blackbody radiation between 200 and 4000 cm^{-1}. The beam splitter is potassium bromide (KBr) and the detector is a liquid nitrogen cooled indium antimonide (InSb) detector. All FTIR measurements were performed at room temperature.

2.3 Diamond anvil cell

A diamond anvil cell (DAC) is a handheld device used to create sustained static high pressure conditions.[100] The sample is compressed between the flattened tips, or culets, of two diamonds, and the pressure is adjusted by tightening the screws on the cell (Figure 2.3). Since pressure is force divided by area, a moderate amount of force applied results in a large pressure increase inside the cell, due to the small area of the diamond culets.

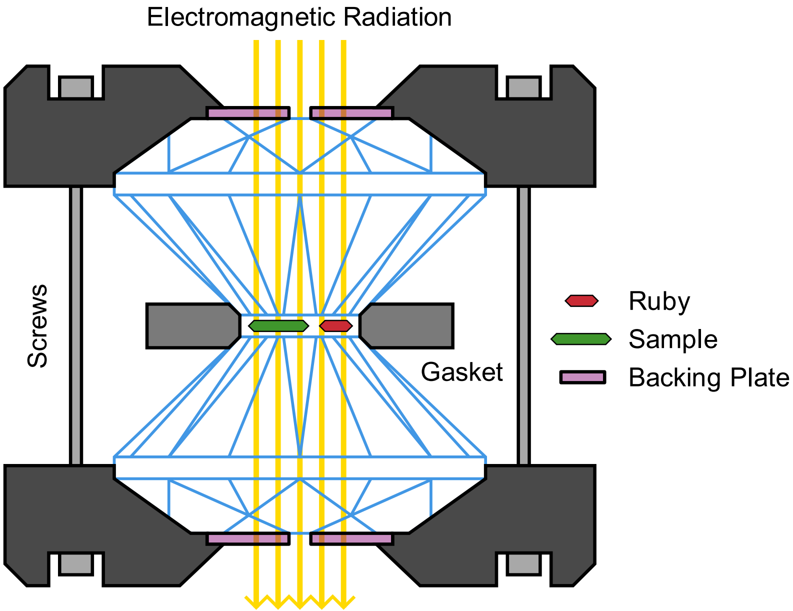

Figure 2.3: Diamond anvil cell cross section.[101]

DACs were developed in the 1950s at the National Bureau of Standards.[102] Diamonds were used as the anvils since they have high mechanical hardness and their optical transparency allows for direct observation of material properties while under pressure.[103] DACs can be used with a cryostat or laser heater for experiments with varying temperatures, and electrical measurements can be made with electrodes inside the cell.[104–107]

The DACs used in this work are piston-cylinder type DACs (Figure 2.4) with a diamond culet face size of 0.6 or 1.0 mm depending on the desired maximum pressure. Diamond anvils were obtained from Almax EasyLab. The sample is held in place between the diamond culets by a precompressed metal gasket with a 0.3-0.5 mm hole drilled in the center. The sample is loaded into the chamber along with a pressure sensor, typically ruby, and a pressure-transmitting medium to ensure that the chamber is at a uniform hydrostatic pressure. After sealing, optical or X-ray measurements of the sample *in situ* under pressure can be performed. All DAC experiments in this work were performed at room temperature.

Figure 2.4: Piston-cylinder type DAC.

2.3.1 Gasket Preparation

Before use in a high-pressure experiment, the diamonds must be aligned to ensure the diamond culet faces are flush and overlapping. Misalignment can cause the diamonds to fracture. The diamonds are attached to the backing plate with epoxy, then attached into the DAC body with set screws. After ensuring the diamonds are clean (small particles on the culets can cause misalignment), the top and bottom of the DAC are put together and the culets can be viewed through a microscope to check alignment. The set screws can be adjusted to align the diamond culets. Interference fringes should be visible on the culet. Empty DAC alignment is determined by monitoring the interference fringe pattern on the culet faces while tightening the DAC screws until the fringes disappear off the edge of the culet. Then the diamond faces are parallel. A dial indicator is used to measure the height at three locations on the top surface of the DAC.

A preindented gasket is used between the diamonds to hold the sample and pressure-transmitting fluid in the sample chamber between the diamonds. The gasket itself is a piece of 0.01” thick stainless steel cut to fit inside the DAC. Preindentation of the gasket ensures that the sample chamber remains roughly the same size under pressure. The gasket is placed between the diamonds and supported by clay. The gasket is then indented by tightening the DAC screws and monitoring the height via the dial indicator until the gasket is the correct thickness (0.002” or less). The DAC screws must be tightened in a star pattern to maintain diamond alignment during tightening.

After preindentation, the gasket is removed from the DAC and a hole is drilled in the center of the indentation. This hole forms the sample chamber. A Betsa electrode discharge drill was used for drilling as it cuts cleanly at this small scale. If necessary, the hole can be finished or widened with a manual hand drill. The gasket should be cleaned ultrasonically after drilling. For 0.6 mm diamond culet sizes, 0.3 mm diameter holes were drilled to allow indented space around the hole (Figure 2.5). For 1.0 mm diamond culets, the hole was 0.5 mm diameter.

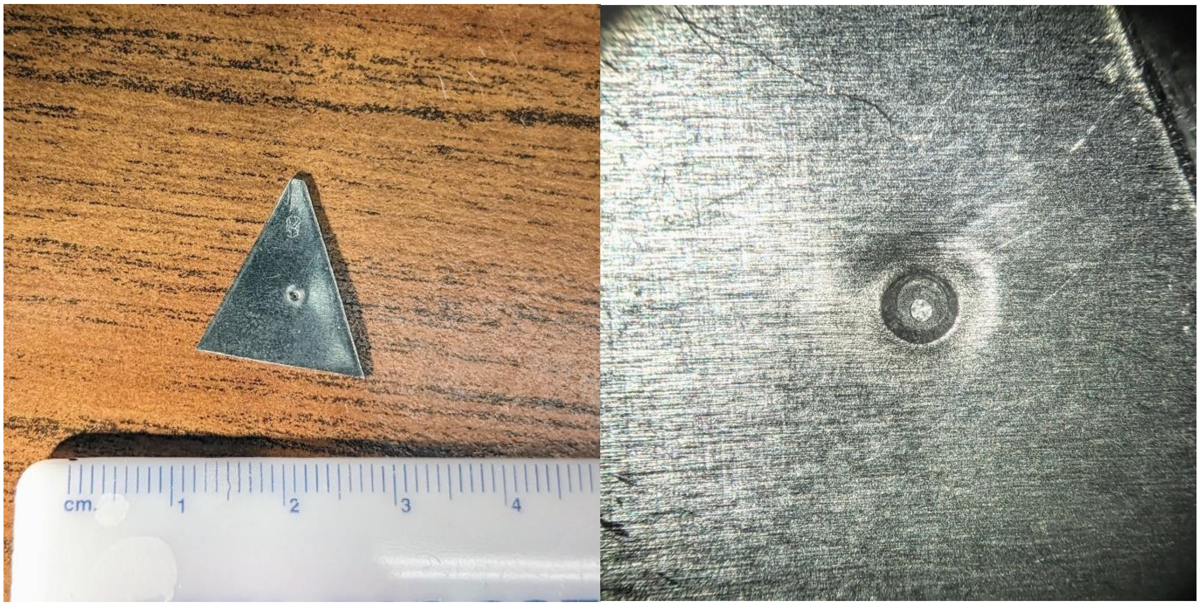

Figure 2.5: (a) Preindented gasket. Note the mark on the top corner to maintain the gasket orientation when it is replaced in the DAC. (b) Close up of the 0.6 mm diameter indentation with 0.3 mm hole drilled.

2.3.2 DAC loading

After the gasket is prepared, the DAC can be assembled for sample loading. Under the microscope, the preindented gasket with hole is aligned over the bottom diamond anvil. Using a needle, 1-3 ruby microspheres are placed into the sample chamber for pressure monitoring. Next the sample is placed into the sample chamber with a needle or tweezers. For powder samples, about ¾ of the gasket hole should be covered with powder. For single crystal samples (discussed further below), the sample should not be touching the sides of the gasket hole. The gasket indentation outside the hole must be free from stray sample pieces or ruby spheres.

Next, the gasket is filled with a pressure-transmitting medium, which transforms the uniaxial stress of the diamond anvils to uniform hydrostatic pressure on the sample chamber.

Hydrostatic pressure is preferred for high pressure experiments as nonhydrostatic pressure can cause variations in strain across the sample and lead to distorted behavior.[15,108,109] Three pressure-transmitting media were used in this work: mineral oil, heptane, and a 4:1 mixture of methanol:ethanol. These pressure media are discussed in more detail in Chapter 5.

Two methods were used to load the sample chamber with a pressure medium. A syringe can be used to place drops of the fluid onto the gasket hole before closing the DAC and tightening the screws to seal. This is the preferred method for mineral oil and heptane. However, for a pressure-transmitting medium such as methanol:ethanol that evaporates quickly, submersion loading is preferred. In this method the DAC is closed after loading the sample, but the screws are not tightened. The DAC is placed in a beaker which is filled with the methanol:ethanol mixture. The holes in the bottom cylinder of the DAC allow the medium to flow into the DAC and sample chamber. The sample chamber should be monitored under a microscope during this procedure to ensure the fluid reaches the sample chamber, no bubbles form, and that the sample remains in the chamber. If there is a bubble, the top of the DAC can be gently lifted a few mm and replaced to reset the liquid inside, but one must ensure the sample or ruby do not escape the chamber. Once the DAC is flooded with the medium, the screws are tightened to seal the DAC. With both loading methods, the pressure inside the DAC should be checked promptly after closure. The pressure inside the DAC should be above ambient (~0.2-0.5 GPa) to ensure the DAC is fully sealed.

2.3.3 Single crystal sample preparation

Single crystal samples must be cut from a larger sample in order to fit into the DAC. Loading the DAC with AGO was especially challenging due to its low and spatially dependent photoluminescence intensity, which was further attenuated by the diamonds. The most effective sample preparation for single crystal samples was:

1. Examine the entire crystal in the spectrometer microscope and find a brightly luminescent spot.

2. Under the viewing microscope, cut that spot from the sample with a razor blade. Ensure the cut sample is sized correctly for the gasket hole. The sample should not touch the sides of the hole. If possible, keep the orientation of the cut sample the same as the entire crystal.For gallium oxide, it was possible to use the natural cleavage planes of the material to separate small slivers and only make one cut to separate an appropriately sized section of sample, and the cleavage planes allow the orientation of the cut sample to be determined by eye.

3. Take the cut sample back to the spectrometer microscope and remeasure the spectra. Check that the intensity is strong enough, remembering that the diamonds will attenuate some of the signal.

4. Load the ruby spheres first and then the cut sample into the DAC using a needle or sharp tweezers to transfer the sample, taking care to maintain its correct orientation.

5. Fill with pressure-transmitting medium through the submersion method and seal the DAC (Figure 2.6).

When working with the tiny single crystal samples used in these experiments, it was helpful to eliminate forces that could dislodge the sample. The needle and tweezers can be grounded from static electricity by touching the gasket metal before touching the sample, and a face mask can be worn during sample loading to avoid breathing on the sample. A microscope slide is useful as a base for cutting the sample and measuring its spectra. Care should be taken to avoid contamination with dust or other particles by cleaning the culets, gasket, and tools with acetone before DAC assembly.

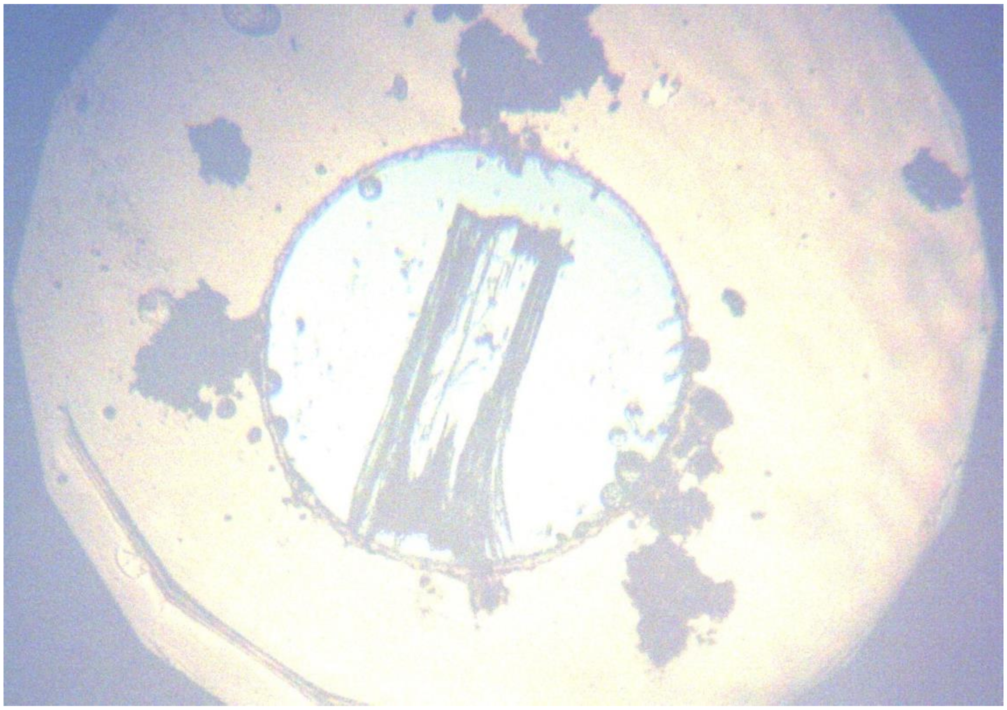

Figure 2.6: Example of a single crystal sample loaded in a DAC, viewed through a microscope. The whole illuminated area is the 0.6 mm diamond culet and the central circular area is the 0.3 mm gasket hole. The gallium oxide sample is in the center of the sample chamber and the ruby spheres are visible around the edge of the sample chamber.

2.4 Pressure sensor

2.4.1 Ruby fluorescence

Ruby fluorescence is a widely used method for determining the pressure inside a diamond anvil cell. The ruby R_1 and R_2 fluorescence peaks are the result of $^2E \rightarrow {}^4A_2$ electronic transitions from chromium ions and are known to shift linearly with pressure from 0-20 GPa.[79,80]

In this work, ruby microspheres were loaded into the DAC along with the sample for *in situ* pressure measurements. A 405 nm laser is focused on the ruby sphere inside the sample chamber and the resulting fluorescence is measured with a spectrometer. The Ruby2020 pressure calibration[81] is used to determine the pressure in the cell based on the shift in the ruby fluorescence peaks compared to the position of the peaks at ambient pressure. Ruby spectra are measured both before and after each experimental sample measurement, and the resulting pressures are averaged to obtain the experimental pressure. The ruby pressure scale was used for all experiments in this work except for experiments on powder gallium oxide, which used alternate pressure sensors as described in the following section.

Multiple ruby spheres can be used in a DAC to determine the hydrostatic limit of a pressure medium. This method was introduced by Klotz et al. as a more accurate way to determine the onset of nonhydrostatic behavior as compared to other methods such as changes in peak splitting or broadening.[110] For these experiments, a DAC is loaded with several (at least six) ruby spheres spaced out around the sample chamber. The cell is filled with pressure-transmitting medium. At each pressure increment, the position of the fluorescence peaks is measured for all ruby spheres. When the pressure-transmitting medium behaves hydrostatically, the standard deviation of pressures for all the ruby spheres will be near zero. When the pressure medium becomes nonhydrostatic, the standard deviation of pressures will increase.

2.4.2 Alternate pressure sensor calibration with FTIR

Powdered gallium oxide was a challenging material to work with in the DAC. This work studies the chromium lines in gallium oxide, which posed a problem with using the chromium lines in ruby as a pressure sensor, as these lines overlap (this was not an issue with single crystal samples as the sample and ruby can be spatially separated in the DAC to allow measurement of one or the other). In addition, the powdered gallium oxide was not intentionally doped with chromium, so the Cr^{3+} luminescence was weak and further attenuated by the diamonds.

To avoid using brightly luminescing ruby, which interfered with the gallium oxide signal, an alternative pressure sensor was needed. We developed a method to use the pressure-transmitting medium as a pressure sensor. Absorption peaks in the infrared (IR) shift with pressure in these materials. These peaks can be calibrated with the ruby pressure scale to provide a measurement of the pressure inside the DAC. Initial experiments on the IR absorption peak shift of mineral oil and heptane were conducted by Ben Whitfield. I performed the subsequent FTIR experiments on mineral oil and heptane under pressure, and fitting to the peak shifts. Calibration experiments and curve fitting for 4:1 methanol:ethanol was conducted by Fiona McLary White.

2.4.2.1 Mineral oil

IR absorption spectra were obtained with an FTIR spectrometer. At near-ambient conditions (0.1 GPa), mineral oil has two major absorption peaks in the infrared at 4259 and 4330 cm^{-1}, called Peak 1 and Peak 2, respectively (Figure 2.7). These peaks are combinations of vibrational modes and shift linearly with pressure up to 3.7 GPa. The linear fits to determine DAC pressure P from the mineral oil IR absorption peaks are given by:

$$P = 0.1475\, k_1 - 628.09$$

$$P = 0.0839\, k_2 - 363.20,$$

where k_1 and k_2 are the wavenumbers of peaks 1 and 2, respectively (Figure 2.8).

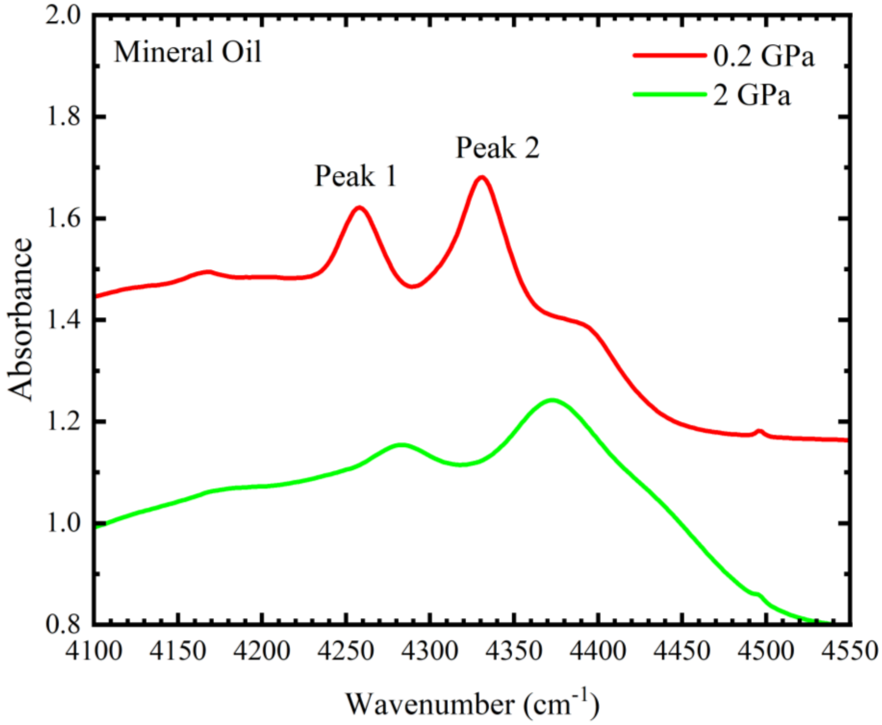

Figure 2.7: IR absorption peaks in mineral oil.

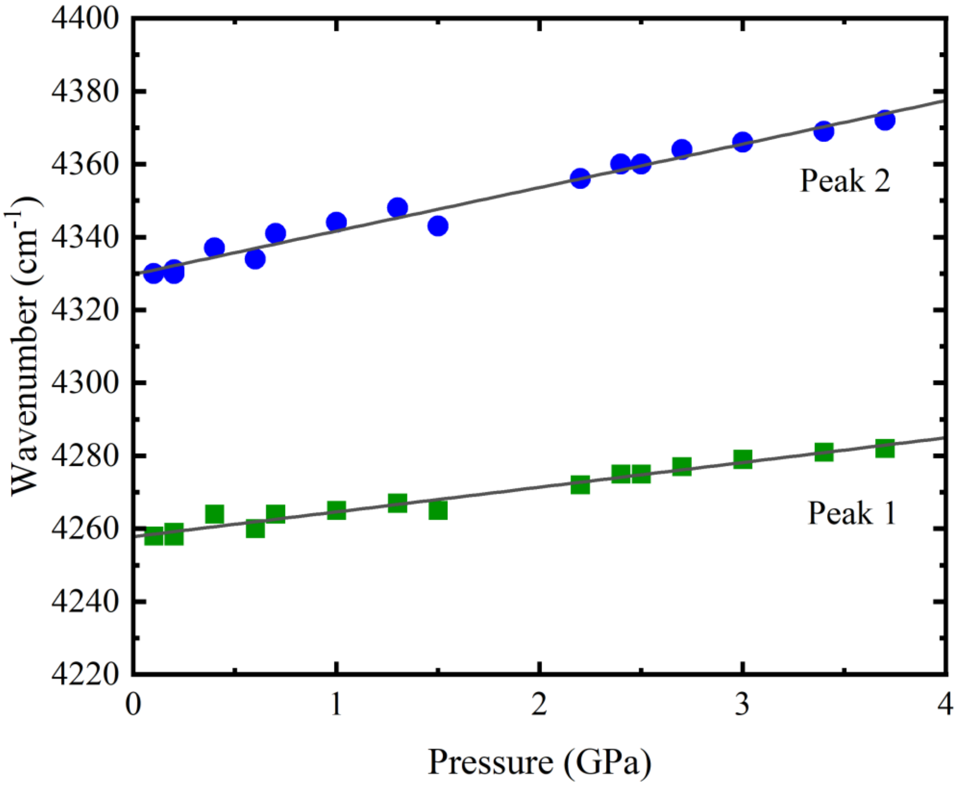

Figure 2.8: Mineral oil IR absorption peaks shift linearly with pressure.

2.4.2.2 Heptane

At near-ambient conditions (0.1 GPa), heptane has two major absorption peaks in the infrared at 4262 and 4334 cm^{-1}, called Peak 1 and Peak 2, respectively (Figure 2.9). These peaks were found to increase in wavenumber with increasing pressure up to 8 GPa. Heptane undergoes a liquid to solid phase transition at 1.2 GPa.[111] The peak shift is linear below 1.5 GPa, with the linear fits found to be

$$k_1\ (\mathrm{cm}^{-1}) = 4257.4(8) + 10.9(2)\ P\ (\mathrm{GPa})$$

$$k_2\ (\mathrm{cm}^{-1}) = 4331.7(6) + 14.0(2)\ P\ (\mathrm{GPa})$$

and follows a third-order polynomial curve above 2.0 GPa, with the nonlinear fit equations

$$k_1\ (\mathrm{cm}^{-1}) = 4265(1) - 1(1)P + 3.6(4)P^2 - 0.29(4)P^3$$

$$k_2\ (\mathrm{cm^{-1}}) = 4334(1) + 9(1)P + 1.8(5)P^2 - 0.18(4)P^3$$

above the discontinuity, where k_1 and k_2 are the wavenumber of peaks 1 and 2, respectively. Note the small dip in peak position around 2.0 GPa (Figure 2.10), which occurs at the same pressure as a potential heptane phase change observed in XRD data. This is discussed in more detail in Chapter 5.

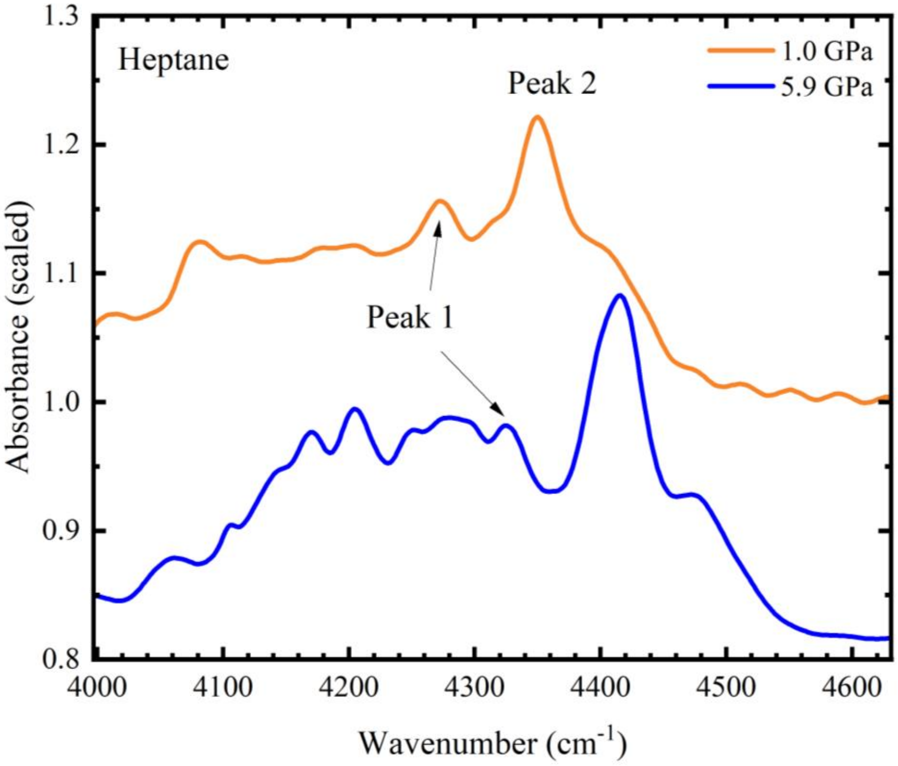

Figure 2.9: IR absorption peaks in heptane.

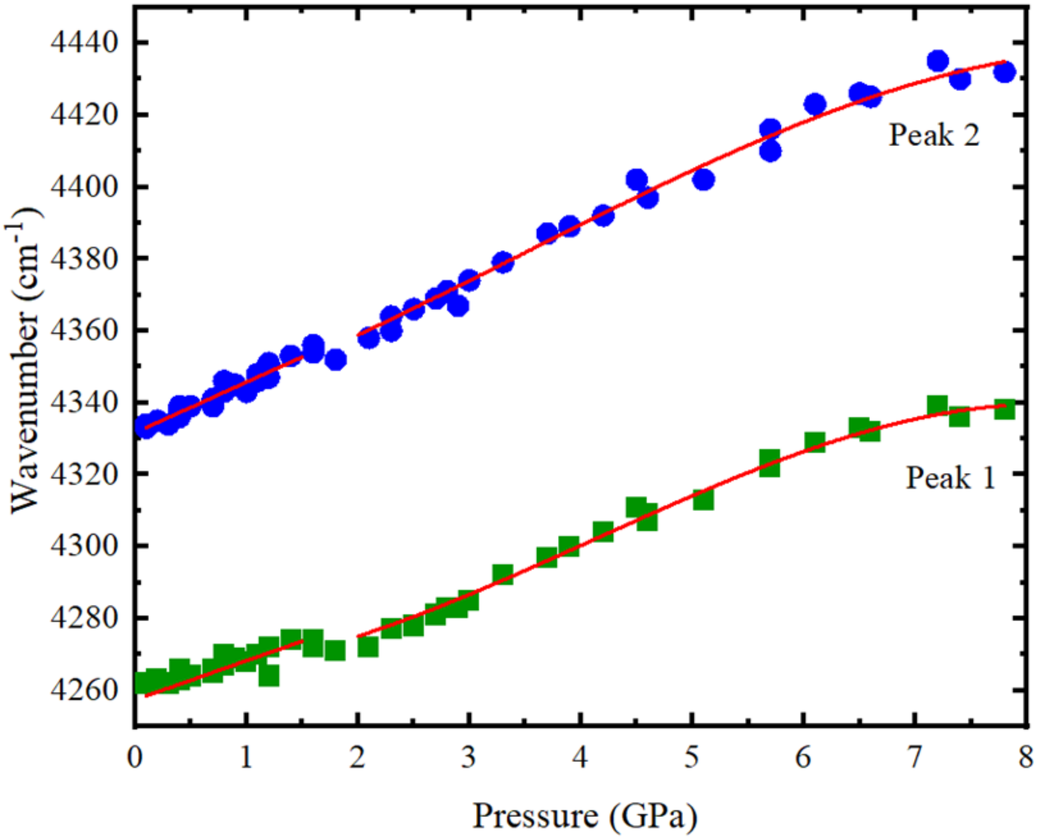

Figure 2.10: Heptane IR absorption peak shifts versus pressure.

2.4.2.3 Methanol:ethanol

At 0.26 GPa, a 4:1 mixture of methanol:ethanol has two absorption peaks in the infrared at 3995.8 cm^{-1} (Peak 1) and 4404.6 cm^{-1} (Peak 2) (Figure 2.11). Peak 2 shifts approximately linearly with pressure up to 9 GPa, while Peak 1 follows a second order polynomial shift up to 5 GPa and linear shift above 5 GPa. The relationship with pressure P follows the equations

$$k_1(P) = \begin{cases} -2.6P^2 + 29.0P + 3986.3, & P < 5\text{ GPa} \\ 15.1P + 3997.0, & P \geq 5\text{ GPa} \end{cases}$$

$$k_2(P) = 13.38P + 4405.1$$

where k_1 and k_2 are the wavenumber of the first and second absorption peaks, respectively (Figure 2.12).

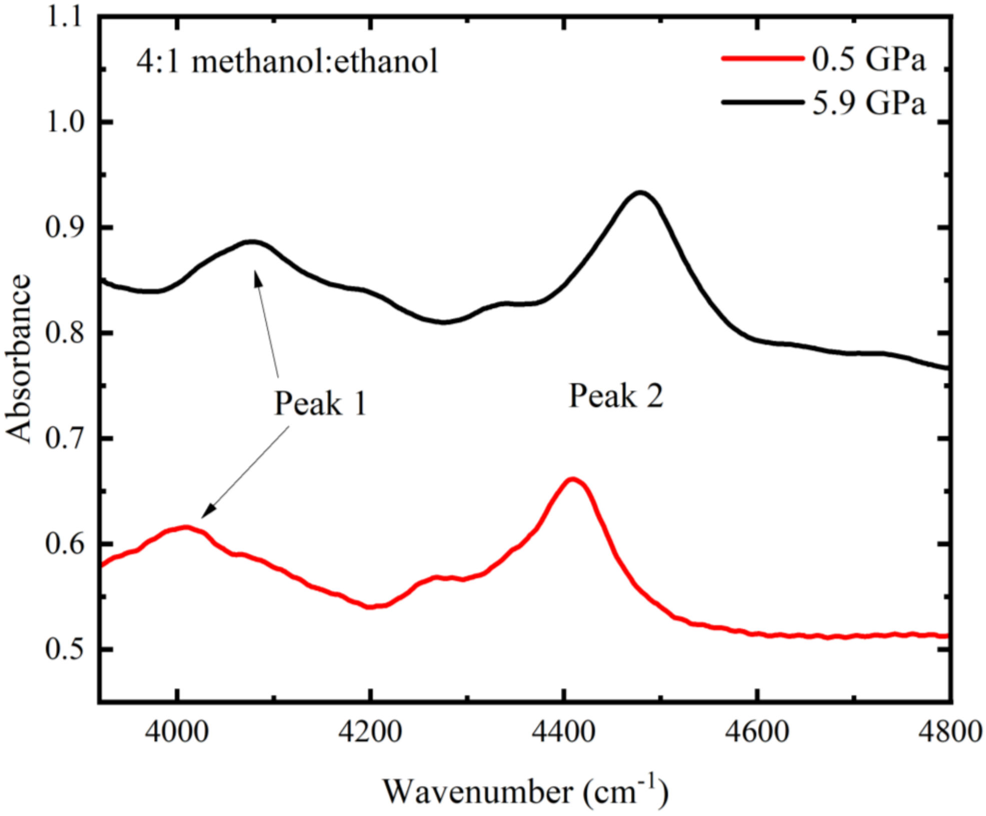

Figure 2.11: IR absorption peaks in 4:1 methanol:ethanol.

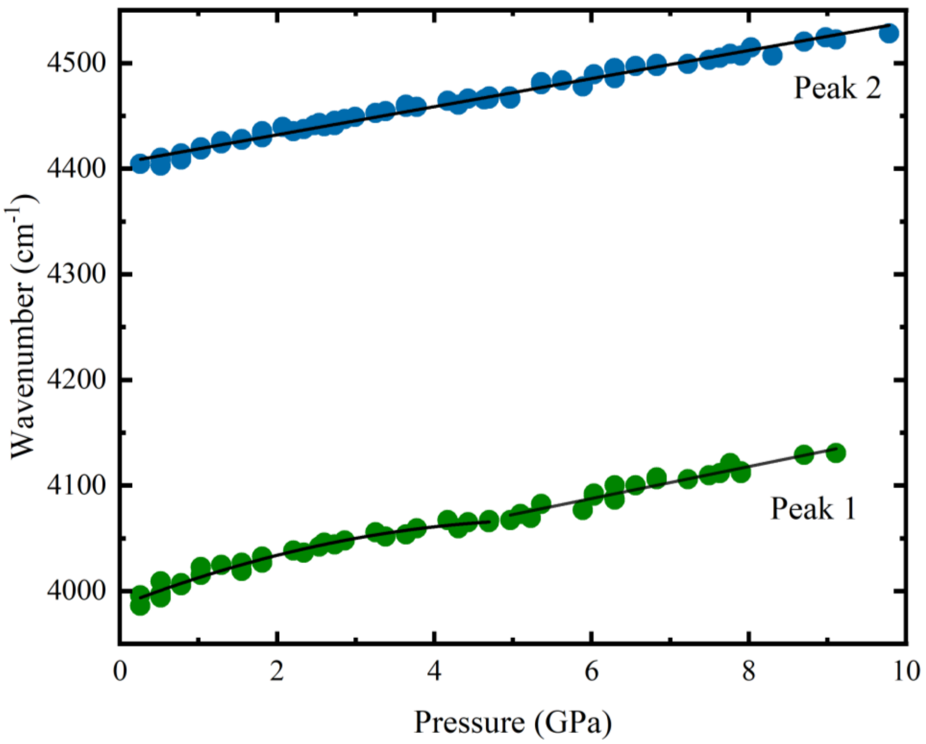

Figure 2.12: Methanol:ethanol IR absorption peaks shift with pressure.

2.5 X-ray diffraction

2.5.1 Synchrotron radiation

When relativistic charged particles travel in a curved path, electromagnetic radiation is emitted. This is called synchrotron radiation or Bremsstrahlung[112] ("braking radiation" in German due to the change in acceleration). Circular electron accelerators like the Advanced Light Source at Lawrence Berkeley National Lab produce intense beams of synchrotron radiation for conducting research.[113]

Synchrotrons produce a high energy electron beam that is accelerated around a storage ring. Bending magnets and insertion devices supply a strong magnetic field perpendicular to the electron beam, which produces beams of synchrotron radiation tangential to the electron storage ring. The radiation is captured at beamline end stations where a variety of laboratory experiments can be performed. Synchrotron light is notable for its high intensity, tunable wavelength, collimation, and polarization.

X-ray diffraction (XRD) is one type of experiment commonly conducted at synchrotron facilities for structural analysis of crystalline materials. A beam of X-rays incident on a crystal is diffracted in many directions. By measuring the specific angles and intensities of the diffracted beams, the crystal structure and position of atoms in the unit cell can be determined. Synchrotron XRD is particularly useful for DAC experiments due to the high resolution, high intensity, and small spot size of the beam.

2.5.2 Bragg diffraction

When incident radiation has a wavelength on the same order as the interatomic distances of a crystal, the scattered beams will interfere constructively at specific angles, resulting in bright peaks. This constructive interference occurs when beams scattered off different atomic planes separated by distance d reach the detector in phase. The second beam travels a distance $2d\sin\theta$ farther than the first beam (Figure 2.13), which causes bright peaks at angles that satisfy the Bragg diffraction condition: when the path length difference is equal to an integer multiple of the wavelength.[9] Thus, the equation for Bragg diffraction is

$$2d\sin\theta = n\lambda.$$

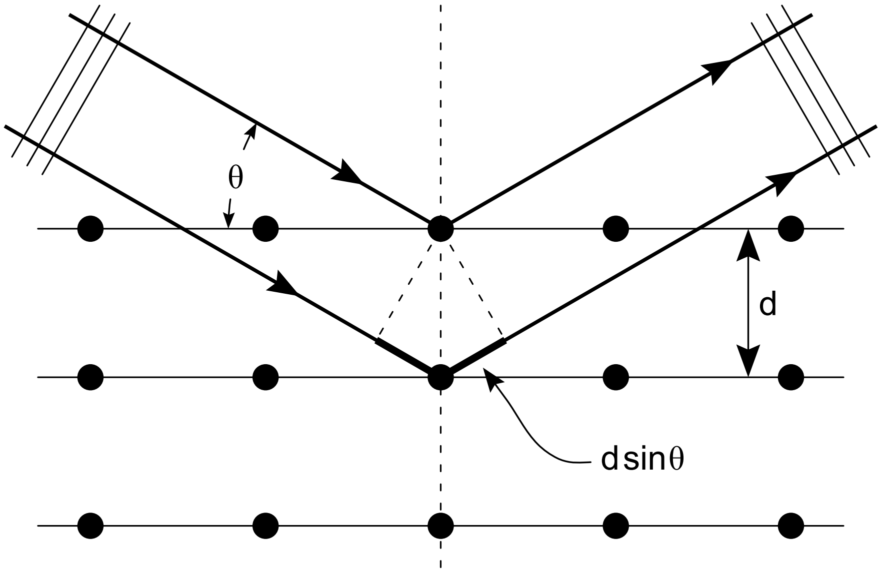

Figure 2.13: Bragg diffraction from a crystal lattice. Plane waves incident on a crystal lattice at angle θ are reflected by parallel crystal planes of spacing d. The superposed reflected waves interfere constructively if the Bragg condition is satisfied.[114]

In XRD, the position of a Bragg diffraction peak is measured by the angle 2θ, where θ is the incident angle of the incoming X-ray beam relative to the atomic planes of the crystal. In powder diffraction, a crystalline sample is crushed into a powder, resulting in a sample comprised of numerous small randomly oriented crystals. The resulting diffraction pattern represents all possible crystal orientations, resulting in concentric circles called Debye-Scherrer rings on the detector (Figure 2.14). Each ring corresponds to a particular reciprocal lattice vector in the sample crystal.[9]

The XRD experiments in this work were performed at the Advanced Light Source at Lawrence Berkeley National Laboratory, beamline 12.2.2.[115] A tunable crystal monochromator is used to select the X-ray energy and mechanical slits control the beam size. I performed XRD experiments on gallium oxide and AGO, which used an energy of 30 keV (0.4133 Å) and beam width of 20 μm. The XRD spectra were collected on a flat plate detector. The distance between the sample and detector was measured using a calibration spectrum from CeO_2, which allows us to calculate the 2θ spacings of the Debye-Scherrer rings on the detector image.

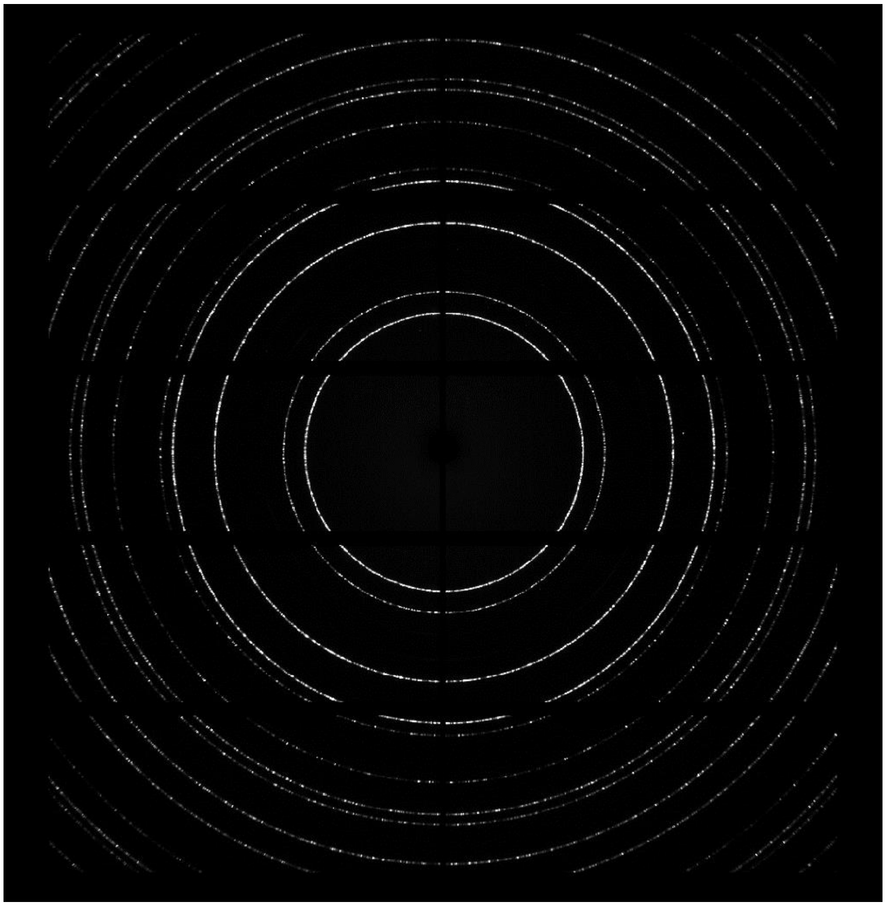

Figure 2.14: Debye-Scherrer rings from CeO_2.

2.5.3 Le Bail refinement

Diffraction images are integrated using the Dioptas program.[116] From the integrated spectrum the Le Bail refinement method[117] is used to obtain the unit cell parameters and determine the atomic structure of the crystalline sample. The Le Bail method fits the measured powder diffraction data by refining the unit cell, profile parameters, and peak intensities.

Le Bail refinement is based on the Rietveld decomposition of the total intensity profile of the powder diffraction data. It follows the formula

$$I_K = \sum_j \{w_{j,K} \cdot S_K^2 \cdot y_j(obs)/y_j(calc)\}$$

where the Bragg peak at position $2\theta_K$ contributes intensity $w_{j,K}$ to the powder diffraction profile y_j at position $2\theta_j$. The structure factor $S^2{}_K$ is calculated from the atomic coordinates, and the total calculated intensity profile at position $2\theta_j$ from all contributing peaks is $y_j(calc)$. The overall intensity I_K is the sum over all $y_j(obs)$ that contribute to the profile. This equation gives the contribution of a single Bragg peak at $2\theta_K$ to the total observed intensity profile.[118,119] In Le Bail refinement, this decomposition formula is used iteratively to approximately determine the structure factor when the atomic positions are unknown.[117] The structure factors S_K are initially set to an arbitrary value and the decomposition formula is used to obtain intensity values I_K for each peak, which are then iterated to determine the next S_K values. Then the unit cell parameters can be refined using the Rietveld refinement method.[118] For this, the decomposition formula is used to decompose the total intensity profile into individual intensities from each Bragg peak based on the structure factor S_K, which are then refined using least-squares refinement. The process is repeated until a good fit is obtained (low R values from least-squares fitting). This method is effective at approximating unit cell parameters even in cases where the intensity profiles from two or more Bragg peaks overlap.

Le Bail refinement was performed using the GSAS-II program.[120] Background fitting used a Chebyschev polynomial fit to selected points on the spectrum. Refinement began with an appropriate space group for the phase and initial unit cell parameters from literature. For sequential increasing or decreasing pressure experiments, the parameters from the previous step were used as the starting point for the refinement of the following step.

2.6 Curve fitting

Nonlinear curve fitting was performed in Python using the scipy.optimize.curve_fit library. This algorithm uses nonlinear fitting to optimize parameters of a given function to input data such that the sum of the squared residuals is minimized using the Levenberg-Marquardt algorithm.[121] Errors on fit parameters are one standard deviation errors on the variance of the parameter estimates. The code written for this work is included in Appendix C.

CHAPTER THREE: TEMPERATURE DEPENDENCE OF CHROMIUM EMISSION

This chapter describes the experiments, analysis, and results of the study of the Cr^{3+} emission of gallium oxide and AGO at varying temperatures. Portions of this work have been published in Ref. 42.

3.1 Experiments

PL spectra of Cr^{3+} in monoclinic single crystal β-Ga_2O_3 and AGO were collected using a Horiba Jobin-Yvon FluoroLog-3 spectrometer with double-grating monochromators and a photomultiplier tube. Temperature-dependent PL properties were examined for these materials and spectra were collected from 295 K to 16 K by Cassandra Remple.

R lines in β-Ga_2O_3 and AGO exhibit redshift with increasing temperature (Figure 3.1) due to interactions between the Cr^{3+} electronic levels and lattice vibrations.[65,122] For both materials, the lower energy R_1 line was found to display stronger intensity at lower temperatures (Figure 3.2), indicating a thermal depopulation of the higher energy ^2E excited state component that results in the R_2 line.[122,123] Above ~100 K, the R_2 line is stronger than R_1. The R lines in AGO exhibit inhomogeneous broadening. This is called alloy broadening due to the incorporation of Al, as a result of the aluminum substitutional atoms distorting bond lengths in the crystal.The R line peaks were fit using the Origin Peak Analyzer peak fitting capabilities.

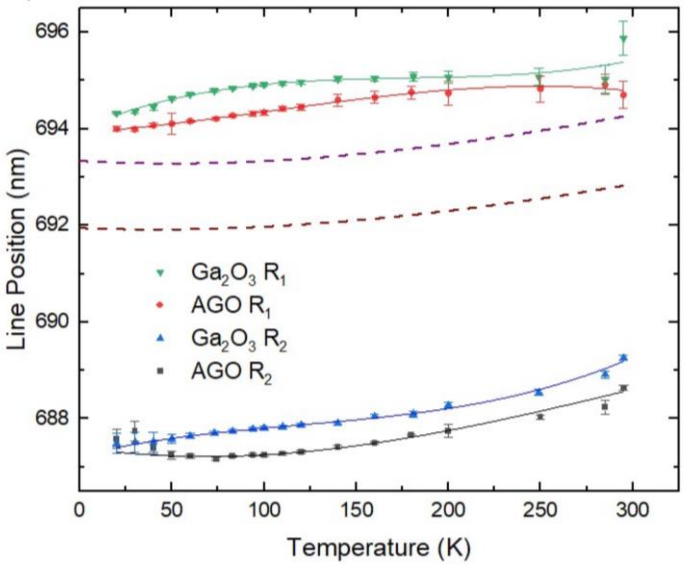

Figure 3.1: R line positions from 20 K to 295 K for both AGO and β-Ga_2O_3. Solid lines correspond to cubic fitting performed on each R line. Dotted lines between 692 and 694 nm correspond to ruby R lines from Ragan et al.[73] *From Ref. 42.*

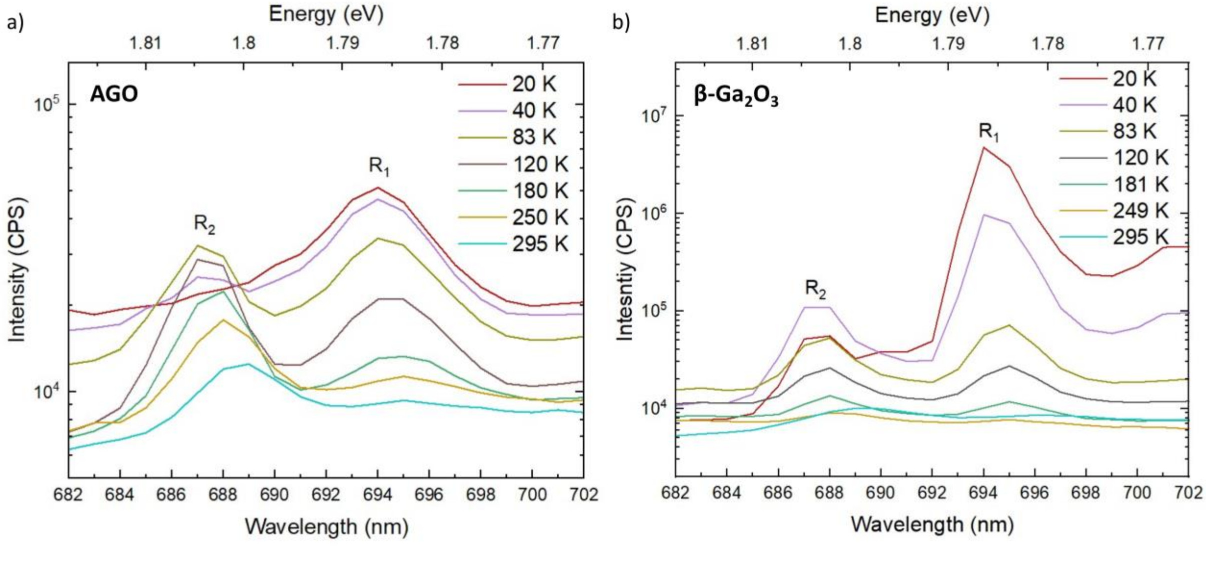

Figure 3.2: Selected PL spectra from 20 K to 295 K at 300 nm excitation for (a) AGO and (b) β-Ga_2O_3. From Ref. 42.

3.2 Peak intensities

To further investigate the change in intensities of the *R* lines as a function of temperature, the peak intensity ratios were modeled. The R_1 and R_2 peak intensities do not follow a simple thermally dependent Arrhenius behavior. Instead, they are strongly affected by nonradiative recombination.

When an electron is excited to a higher energy level, it leaves behind a hole – a quasiparticle with a net positive charge that represents the missing electron and can function as a charge carrier in the crystal. An electron in an excited state can transition to a lower level by recombining with a hole and emitting a photon through radiative decay, but there are also mechanisms which allow for nonradiative recombination which do not emit light. The energy in these cases is typically dissipated in the form of phonons (lattice vibrations of a solid) or heat.[7] Nonradiative recombination can lead to lower light-generation efficiency and increased heating in lasers.[8] As discussed in Chapter 2, PL spectroscopy only measures radiative decay since no light is emitted in nonradiative decay. The measured PL intensity can be modeled as the fraction of electron-hole recombinations that are radiative.

The total electron recombination rate is the sum of the radiative and nonradiative recombination rates:[124]

$$\frac{1}{\tau} = \frac{1}{\tau_{rr}} + \frac{1}{\tau_{nr}} \qquad (1)$$

Radiative recombination, which is measured in these PL experiments, is assumed to be temperature-independent.[67] The nonradiative recombination frequency is thermally activated and can be represented by an Arrhenius function. With these assumptions, the total recombination rate is given by

$$\frac{1}{\tau} = C + De^{-E/kT} \tag{2}$$

The measured intensity (total peak area) of the R_1 line is proportional to the fraction of all decays that are radiative,

$$I_{R_1} = \frac{I_1 C_1}{C_1 + D_1 e^{-E_1/kT}} \tag{3}$$

where E_1 is the activation energy of the nonradiative channel and k is the Boltzmann constant.[67] The R_2 line intensity is described by a similar function. The ratio of the intensity of R_2 to the intensity of R_1 is then given by

$$I_{\frac{R_2}{R_1}} = A\, e^{\frac{-E}{kT}} \left(\frac{1 + A_1 e^{\frac{-E_1}{kT}}}{1 + A_2 e^{\frac{-E_2}{kT}}} \right) \tag{4}$$

where the $e^{-E/kT}$ term represents the thermal population and E_1 and E_2 are the nonradiative recombination activation energies for R_1 and R_2, respectively. Taking a ratio highlights the difference between the two lines and eliminates overall changes in intensity. The experimental intensity ratio is plotted against temperature (Figure 3.3) and fit to Eq. (4). The fit parameters are the activation energies (E_1 and E_2) and the scaling factors (A, A_1, A_2). E is held constant and is equal to the R_1-R_2 splitting (19.82 meV), similar to the value from Tokida and Adachi.[122] Table 3.1 lists the fit parameters.

Dotted lines in Figure 3.3 represent the thermal population fit only, using only the Arrhenius $Ae^{-E/kT}$ term, which clearly do not fit the data above 50 K. The trends of these lines demonstrate that nonradiative recombination dominates the peak intensities for temperatures above 50 K. The curves approach zero in the low temperature limit, due to the depopulation of the higher energy state of the ^2E level, which is the upper level for the R_2 line emissions. The fit parameters (Table 3.1) show significant differences for the two materials. Nonradiative recombination in β-Ga_2O_3 is thermally activated. At low temperatures, the R_1 line becomes very strong as the nonradiative effect goes to zero and all emission is radiative. In AGO, however, the nonradiative recombination for the R_1 line is temperature independent. This means that the R_1 line in AGO does not experience the large intensity increase at low temperature that was observed in β-Ga_2O_3.[42]

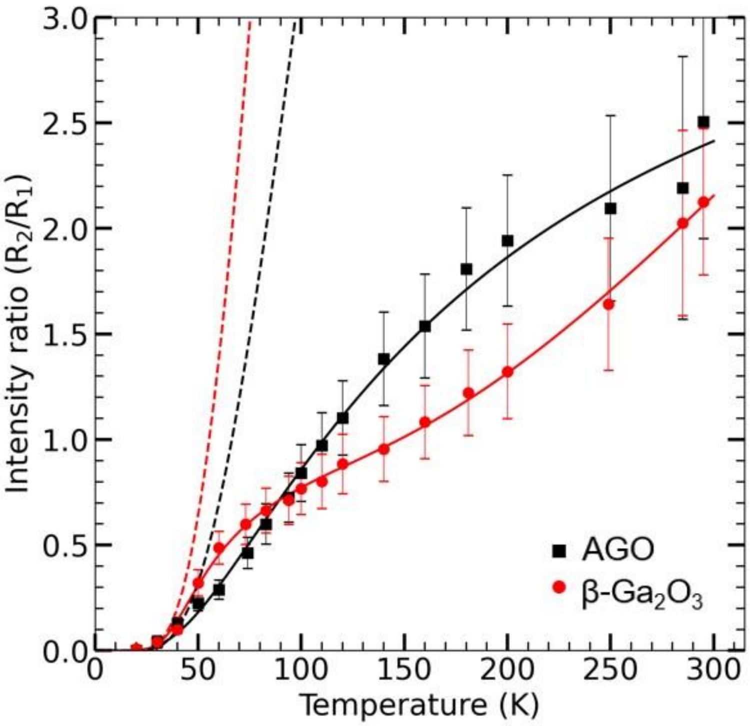

Figure 3.3: PL intensity ratio (R_2/R_1) versus temperature for β-Ga_2O_3 and AGO. Solid lines represent the least-squares fitting to Equation 4 with the parameters in Table 3.1. Dotted lines represent the thermal population Arrhenius fit only.

	***β*-Ga₂O₃:Cr³⁺**	**AGO**
A	63.6	31.9
E (meV)	19.8 (held constant)	
A_1	9.9	37.4
A_2	302.2	50.2
E_1 (eV)	0.0593	0
E_2 (eV)	0.0166	0.0065

Table 3.1: Fit parameters

3.3 Power independence

Slight differences (~0.5 nm) were noted in the position of the AGO R_1 line between the Horiba PL spectrometer system and the laser and spectrometer PL system. The Horiba PL uses a xenon lamp with a monochromator to select 405 nm wavelength light as an excitation source, while the laser PL system uses a 405 nm laser to excite the sample. An optical power meter was used to determine the power received by the sample for each system.

To establish if the peak position depends on the source power, a 532 nm variable power laser source was used to excite the sample at powers ranging from 0.2 to 45 mW. No differences in peak position were detected for the either Ga_2O_3 or AGO samples at various power excitations. The initial AGO R_1 line position differences were attributed to the different collection methods of the two systems – the Horiba PL has a larger spot size and collects an average luminescence across the sample, while the laser PL system excites and collects photons from a small focused spot on the sample. The AGO sample had larger variance in luminescent intensity across the sample than Ga_2O_3, which is why this difference was only apparent for AGO.

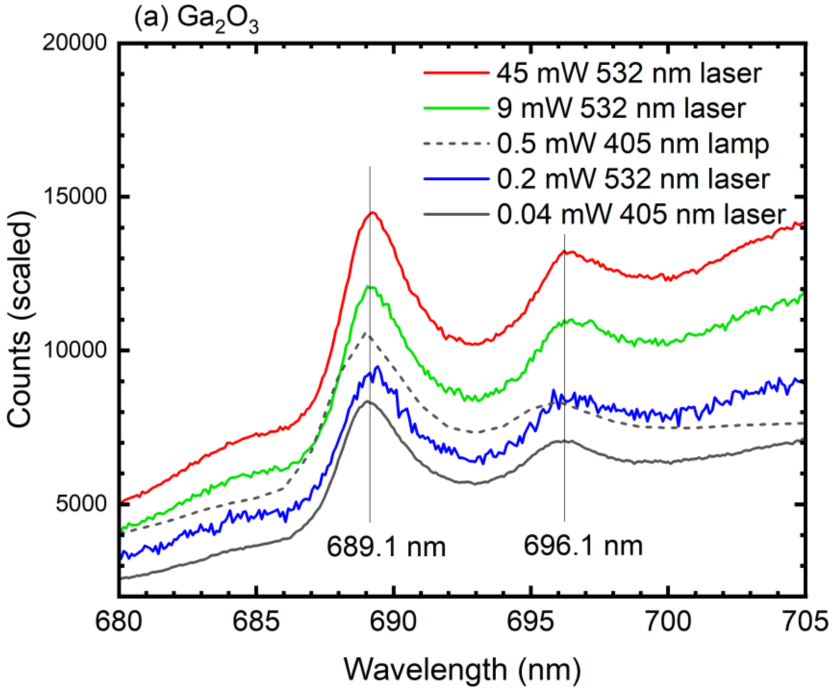

Figure 3.4: Ga_2O_3 R lines with varying excitation power and source.

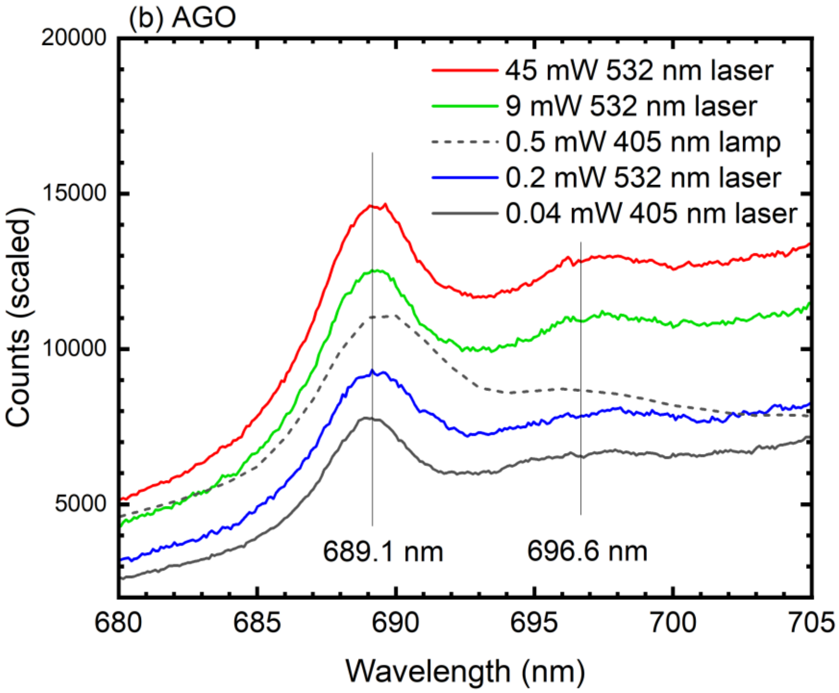

Figure 3.5: AGO R lines with varying excitation power and source.

3.4 Discussion

R lines for both Ga_2O_3 and AGO showed a redshift with increasing temperature. The AGO peak displayed inhomogeneous broadening due to the aluminum inclusions distorting atomic bond lengths. At low temperatures, the R_1 line intensity is dominant due to thermal depopulation of the R_2 line. At temperatures greater than 50 K, the R_2/R_1 intensity ratio is strongly affected by nonradiative recombination. In Ga_2O_3, the nonradiative contribution is thermally activated, which results in strong emission at low temperatures, particularly in R_1. AGO has smaller thermal activation barriers, possibly due to the increased disorder of the alloy which provides more nonradiative recombination pathways. The position of the R lines for both materials is independent of the excitation source power.

CHAPTER FOUR: GALLIUM OXIDE AND ALUMINUM GALLIUM OXIDE UNDER PRESSURE

This chapter describes the experiments, analysis, and results of the study of gallium oxide (β-Ga_2O_3:Cr^{3+}) and aluminum gallium oxide $(Al_{0.1}Ga_{0.9})_2O_3$ (AGO) under static pressure. Portions of this chapter have been published in Reference 125.

4.1 Hydrostatic compression of single crystal gallium oxide

The effects of pressure on single crystals of Cr-doped gallium oxide (β-Ga_2O_3:Cr^{3+}) were examined by measuring the wavelength shift in the spectral *R* lines. Gallium oxide was measured under hydrostatic pressure using 4:1 methanol:ethanol as a pressure-transmitting medium, which is hydrostatic to 10.5 GPa.[110]

4.1.1 Photoluminescence

PL spectra were measured for β-Ga_2O_3:Cr^{3+} in methanol:ethanol under pressure using diamond anvil cells at pressures up to 9 GPa (Figure 4.1). The background was not subtracted from the spectra to avoid introducing artifacts into the data. The background also provides information from transitions involving other electronic states besides those that give rise to the *R* lines (Section 4.5).

These experiments provide a measure of the peak shift of the *R* lines versus hydrostatic pressure. Under hydrostatic pressure, the position of the red chromium emission peaks shift linearly with increasing pressure. The linear fits of peak position versus pressure are given by (Figure 4.2)

$$\lambda_{R_1}(\text{nm}) = 695.93(6) + 0.86(1)\, P\ (\text{GPa}) \qquad (1)$$

$$\lambda_{R_2}(\text{nm}) = 688.82(4) + 0.270(7)\,P\ (\text{GPa}). \qquad (2)$$

The position of the chromium *R* lines in ruby ($Al_2O_3:Cr^{3+}$) increase approximately linearly with pressure up to 20 GPa with constant line splitting.[79,81] In gallium oxide, the *R* line positions also shift linearly with pressure, but the splitting is larger and increases with increasing pressure (Figure 4.2). Additionally, the broad background of the chromium emission is much more evident in gallium oxide than ruby, though this broad background is suppressed with increasing pressure[44] (Figure 4.1).

The spectral differences between gallium oxide and ruby can be ascribed to the different structures of these two materials, which lead to different crystal field effects on the chromium ions. In particular, the lower site symmetry in gallium oxide results in a large, pressure-dependent splitting of the R_1 and R_2 lines.[126] In ruby, R_1 has higher intensity. In β-$Ga_2O_3:Cr^{3+}$, however, R_2 has a higher intensity than R_1 at ambient pressure, but R_1 grows in intensity as pressure is increased. This effect can be attributed to pressure-dependent nonradiative recombination as discussed Section 4.5. No discontinuity or new peaks that may be evidence of a phase transition were observed up to 9 GPa.

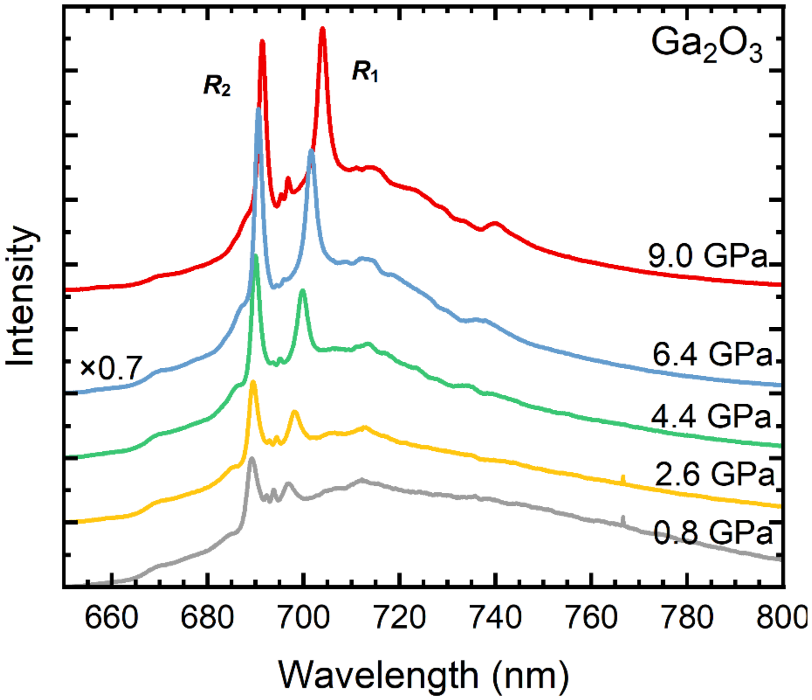

Figure 4.1: Representative spectra of β-Ga_2O_3*:*Cr^{3+} *at multiple pressures, offset vertically for clarity. The smaller peaks between the gallium oxide R lines are the ruby R lines.*

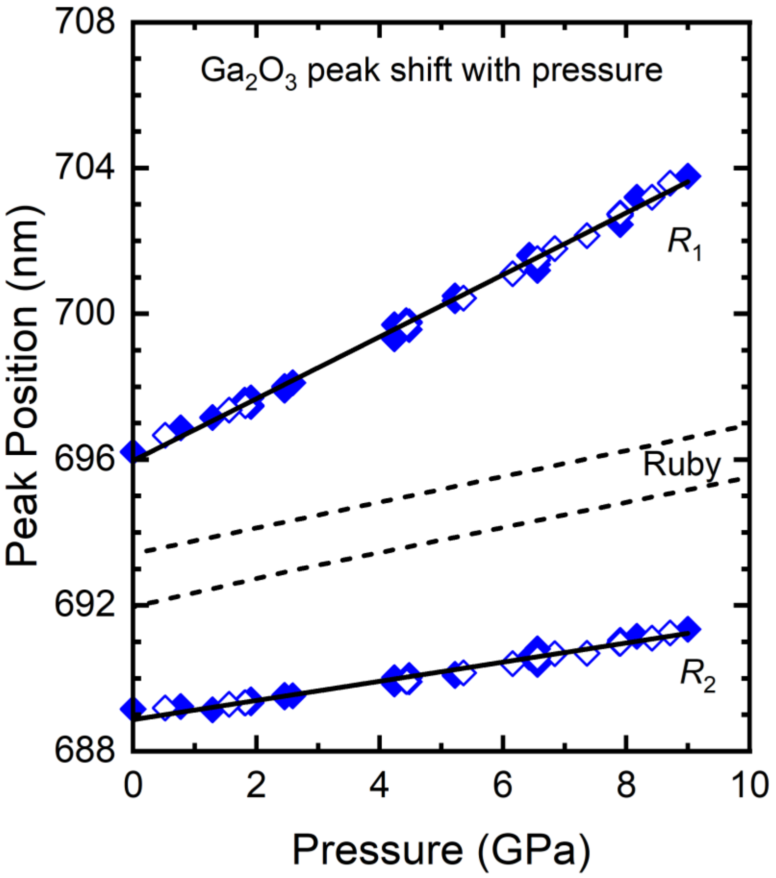

Figure 4.2: Peak position of R lines versus pressure in β-Ga_2O_3*:*Cr^{3+} *in methanol:ethanol (multiple experimental runs shown). Dashed lines are the peak positions for ruby.*[80] *Solid and open symbols refer to data collected after increasing or decreasing the pressure, respectively.*

4.1.2 Photoluminescence mapping

PL mapping was used to measure the PL spectra at many points across the sample.[127] This method allows changes in the spectra to be observed with high spatial resolution. By measuring the position of the *R* lines across the entire gallium oxide sample under pressure, we can gain insight into the internal stresses in the sample. Under hydrostatic stress, the sample showed minor stress deviations within the crystal (the *b* direction is the growth direction).

Figure 4.3 shows PL maps of a DAC experiment. The DAC was loaded with β-Ga_2O_3:Cr^{3+}, ruby spheres, and the pressure-transmitting medium methanol:ethanol. The cell was compressed to 7.9 GPa and PL mapping was performed. Image (a) shows the energy of R_1 under hydrostatic stress, while image (b) shows the energy of R_2. The sample under hydrostatic stress shows minimal variation in the energy of R_1 or R_2.

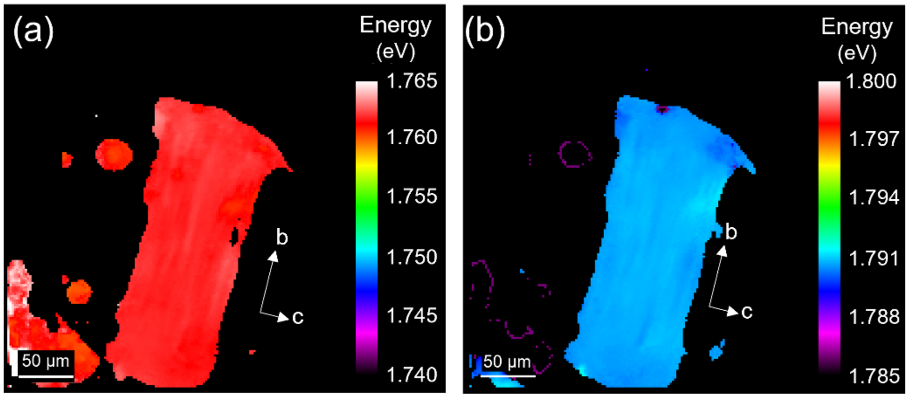

Figure 4.3: PL maps of β-Ga_2O_3:Cr^{3+} at 7.9 GPa with 4:1 methanol:ethanol (hydrostatic) as pressure medium. (a) map shows energy of R_1 peak. (b) map shows energy of R_2 peak.

4.1.3 X-ray diffraction

To further investigate the compression of Ga_2O_3, X-ray diffraction (XRD) was performed on a sample of powdered Ga_2O_3:Cr^{3+} crystal under pressure in methanol:ethanol. The XRD experiments were performed at the Advanced Light Source at Lawrence Berkeley National Laboratory, beamline 12.2.2.[115] These experiments used an energy of 30 keV (0.4133 Å) and beam width of 20 μm. Diffraction images were integrated using the Dioptas program.[116] From the integrated spectra (Figure 4.4), the Le Bail refinement method[117] in the GSAS-II program[120] was used to obtain the unit cell parameters and determine the atomic structure of the crystalline sample. The Le Bail method fits the measured powder diffraction data by refining the unit cell, profile parameters, and peak intensities. The DAC failed at a peak pressure of 6 GPa so only increasing pressure data was obtained for this experiment. No discontinuity in the volume versus pressure relationship or appearance of new peaks that may be evidence of a phase transition in Ga_2O_3 were observed up to 6 GPa. Ambient powder diffraction data were also obtained outside of the DAC.

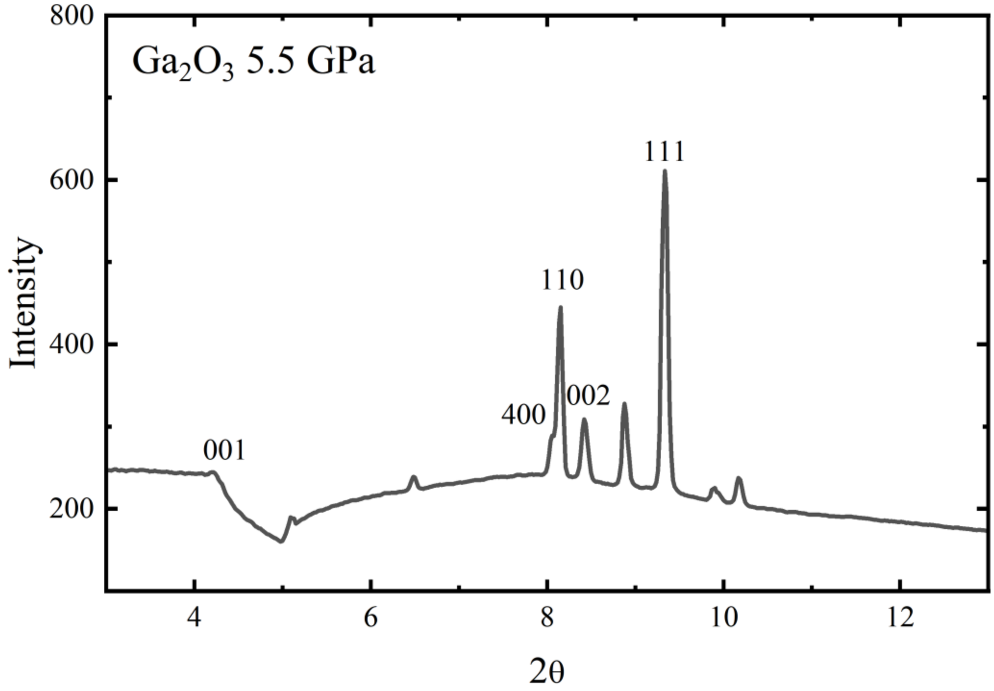

Figure 4.4: Integrated XRD peaks for Ga2O3 at 5.5 GPa

The unit cell volume *V* versus pressure *P* relationship was fit with a third-order Birch-Murnaghan[128–130] equation of state,

$$P = \frac{3}{2}K_0\left[\left(\frac{V_0}{V}\right)^{7/3} - \left(\frac{V_0}{V}\right)^{5/3}\right]\left\{1 + \frac{3}{4}(K'_0 - 4)\left[\left(\frac{V_0}{V}\right)^{2/3} - 1\right]\right\} \tag{3}$$

where V_0 is the unit cell volume at zero pressure, K_0 is the bulk modulus at zero pressure, and K'_0 is the pressure derivative of the bulk modulus at zero pressure. In this case, the Birch-Murnaghan fit was carried out with K'_0 constrained to 4, so the fit equation is

$$P = \frac{3}{2}K_0\left[\left(\frac{V_0}{V}\right)^{7/3} - \left(\frac{V_0}{V}\right)^{5/3}\right] \tag{4}$$

Fitting the Ga_2O_3 XRD data with this equation of state results in fit parameters of V_0 = 213.76 Å^3 ± 0.72 Å^3 and K_0 = 141.1 GPa ± 17.4 GPa. These results are different from the published equation of state for gallium oxide[30] (V_0 = 209.4 Å^3, K_0 = 184 GPa) and both are plotted in Figure 4.5. Differences in these equations of state are likely due to fitting over different pressure ranges as well as possible differences in the Ga_2O_3 crystal – the sample used in Reference 30 was only partially crystalline and was annealed to transform it into fully crystalline material, while my sample was a uniform single crystal of Ga_2O_3 that was crushed into a powder for XRD experiments. The ambient powder measurement is shown on the plot but not included in the fit due to the different data collection method for that point (ambient powder was not measured inside the DAC).

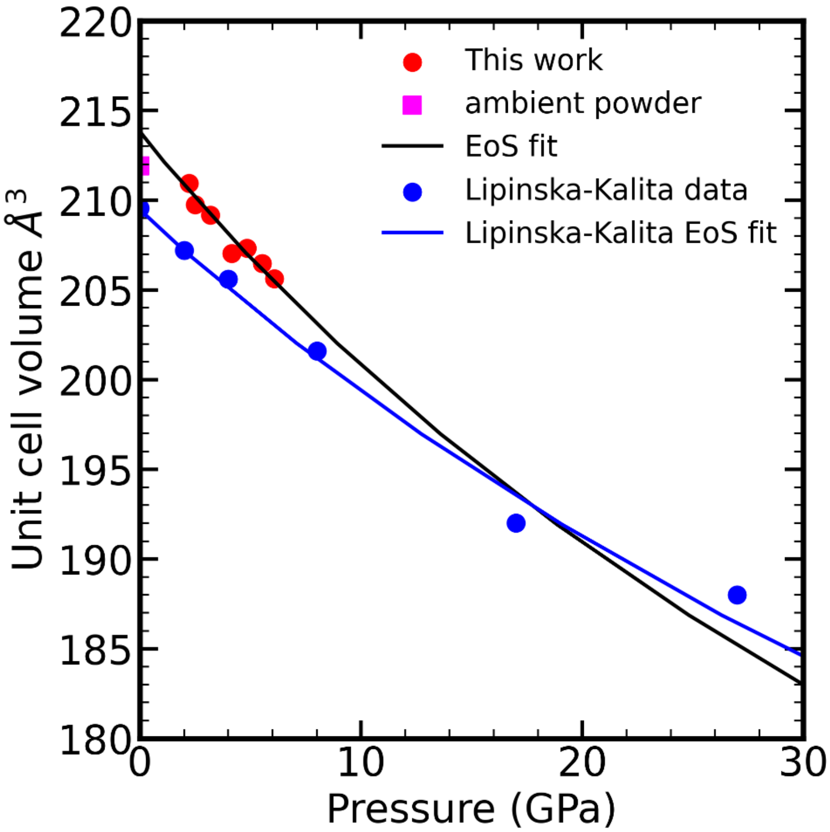

Figure 4.5: Unit cell volume versus pressure for Ga_2O_3 *with the Birch-Murnaghan equation of state fit.*

4.2 Hydrostatic compression of single crystal AGO

DAC experiments were performed on single crystal AGO up to 9 GPa using 4:1 methanol:ethanol as a pressure-transmitting medium, which is hydrostatic to 10.5 GPa.[110] Experiments on as-grown AGO in the DAC were not successful because the intensity of the chromium emission lines was too weak to measure. To address this problem, some AGO samples were annealed in oxygen at 1300 °C for 15 h. Annealing in oxygen shifts the Fermi level toward the middle of the bandgap and changes the charge state of the chromium ions to 3+, which increases the R line intensity.[1] Chromium diffusion was another technique used in this work to increase Cr^{3+} luminescence in AGO. An AGO sample was placed in contact with chromium metal and heated in air at 1000 °C for 15 h. Both O_2 anneal and and chromium diffusion AGO samples were used in these experiments and no difference in sample behavior was detected between these two methods.

4.2.1 Photoluminescence

The effects of pressure on single crystals of AGO were examined by measuring the wavelength shift in the spectral R lines in methanol:ethanol up to 9 GPa. Since AGO is an alloy of Al_2O_3 and Ga_2O_3, it would be reasonable to predict that the R lines of AGO would lie between those of its constituent components. However, the line splitting in AGO is wider than both ruby and β-Ga_2O_3, with ambient peaks at 689.1 and 696.6 nm. Additionally, the R_1 peak in AGO is notably broader than that of β-Ga_2O_3:Cr^{3+} (Figure 4.6). This difference is likely due to the perturbation of the aluminum atoms on the crystal field around the chromium impurities, leading to lower symmetry and inhomogeneous broadening. The perturbation affects the R_1 line more strongly than R_2. Evidently the R_1 line is more sensitive to crystal field effects in addition to nonhydrostaticity.[15]

The R lines (Figure 4.6) shift linearly versus pressure and are described by the following fits:

$$\lambda_{R_1}(\mathrm{nm}) = 697.17(7) + 0.70(1)\, P\ (\mathrm{GPa}) \tag{5}$$

$$\lambda_{R_2}(\mathrm{nm}) = 688.88(4) + 0.261(7)\, P\ (\mathrm{GPa}) \tag{6}$$

As shown in Figure 4.7, while the R_2 line shift is the same as that for β-Ga_2O_3:Cr^{3+}, the R_1 line shows a smaller shift. Both O_2 annealed and Cr-diffused AGO samples displayed this same behavior. As discussed in Section 4.2.2, this difference in the peak shift cannot be accounted for by the AGO equation of state.

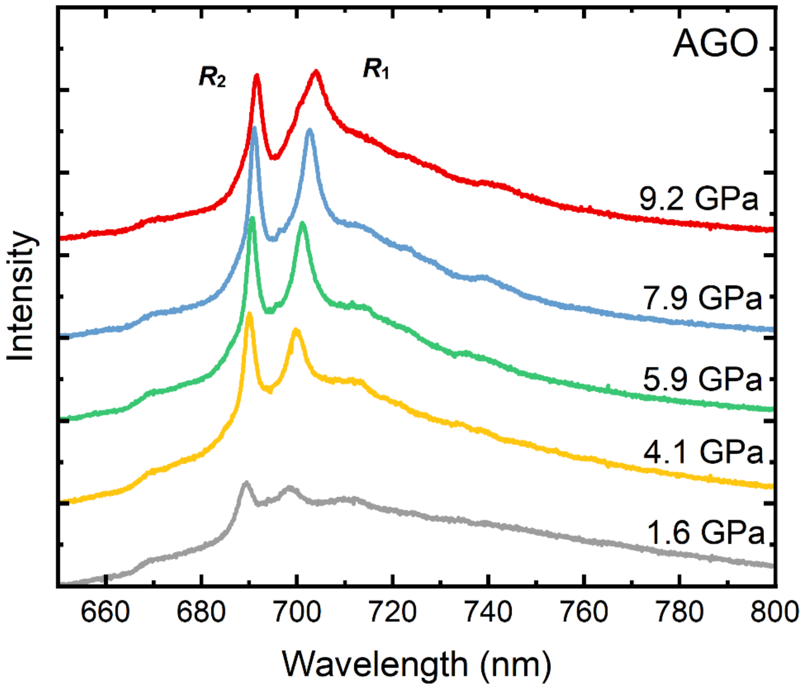

Figure 4.6: Representative spectra of AGO at multiple pressures, offset vertically for clarity.

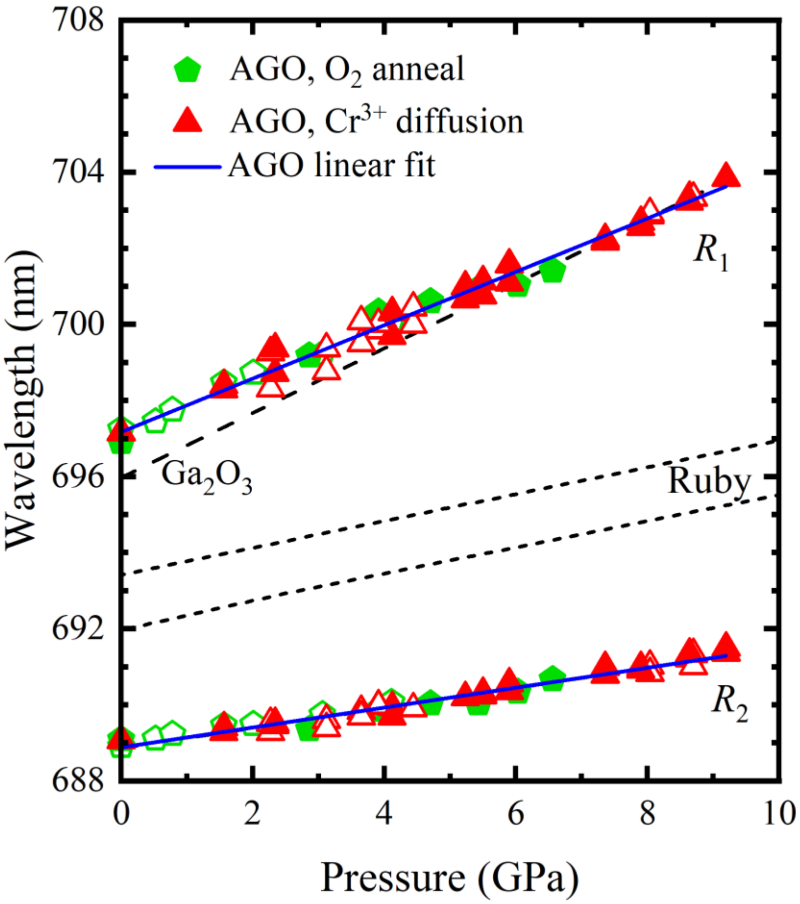

Figure 4.7: Peak position versus hydrostatic pressure for AGO in methanol:ethanol. Solid and open symbols refer to data collected after increasing or decreasing the pressure, respectively. For reference, shifts are plotted for β-Ga_2O_3:Cr^{3+} (black dashed line) and ruby (black dotted line).[80]

The peak energy splitting ($E_{R_2} - E_{R_1}$) (Figure 4.8) is fit well with a linear fit for both Ga_2O_3 and AGO. These linear fits are:

$$\mathrm{Ga_2O_3}\colon E\ (\mathrm{eV}) = 0.00146(2) * P\ (\mathrm{GPa}) + 0.0184(1) \tag{7}$$

$$\mathrm{AGO}\colon E\ (\mathrm{eV}) = 0.00110(4) * P\ (\mathrm{GPa}) + 0.0211(2) \tag{8}$$

The *R* line splitting in AGO shows a smaller shift than the splitting in Ga_2O_3. Since this difference cannot be accounted for solely by differences in volume compression (Section 4.2.2), the variation in line splitting between the two materials is due to the alloy composition and differences in atomic bonding caused by the aluminum atoms.

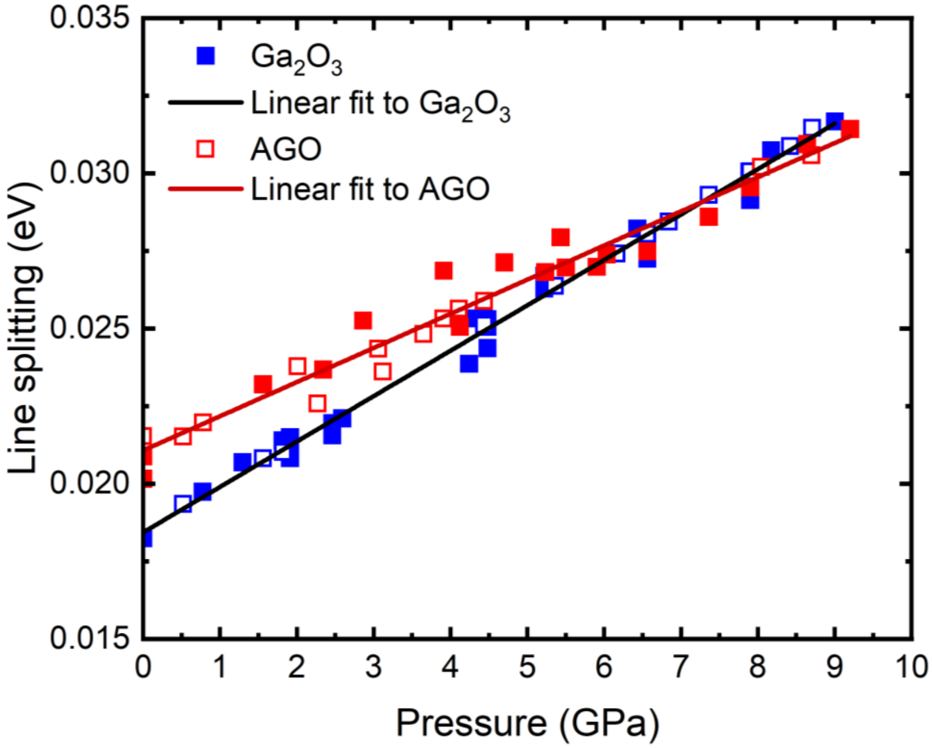

Figure 4.8: R line splitting ($E_{R_2} - E_{R_1}$) and linear fits for Ga_2O_3 (blue) and AGO (red). Solid and open symbols refer to data collected after increasing or decreasing the pressure, respectively.

4.2.2 X-ray diffraction

To further investigate the compression of AGO, X-ray diffraction (XRD) experiments were performed on AGO single crystal crushed into a powder in a DAC under hydrostatic pressure with methanol:ethanol. The data collection and analysis performed for AGO were the same as those described in Section 4.1.3 for Ga_2O_3. A representative integrated spectrum is shown in Figure 4.9 and a plot of the XRD data and fitted curve is shown in Figure 4.10 to demonstrate how well the fitted curve matches the data. Ambient powder diffraction data were also obtained outside of the DAC.

A second XRD experimental run was performed on AGO under hydrostatic pressure. However, the angle of the DAC baseplate opening was narrower than Run 1, so fewer diffraction peaks are visible. Fewer peaks cause higher uncertainties in the unit cell parameters obtained from the Le Bail refinement process, which may contribute to uncertainty in the EoS fit.

The unit cell volume V versus pressure P relationship was fit with a third-order Birch-Murnaghan[128–130] equation of state (EoS) with K'_0 constrained to 4 (Eqn. 4). Fitting the AGO XRD data (all data points in Figure 4.11) with this EoS results in fit parameters of V_0 = 209.9(2) Å^3 and K_0 = 194(8) GPa. These results are similar to the equation of state for β-Ga_2O_3, 209.4(2) Å^3 and 184(3) GPa;[30] however, the high scatter in AGO data did not allow quantitative comparison between Ga_2O_3 and AGO.

The bulk moduli K_0 of AGO and β-Ga_2O_3 are the same to within experimental error, so the two materials have approximately the same compressibility. Within the standard errors, the bulk modulus of AGO is at most ~10% greater than that of β-Ga_2O_3. However, the AGO R_1 line shift versus pressure is ~20% lower than β-Ga_2O_3. Hence, the difference in R_1 line behavior cannot be attributed solely to differences in volume under pressure. We note that the R_1 line is sensitive to nonhydrostatic stress while the R_2 line is not (Section 4.1.1). Similarly, the R_1 line is sensitive to *alloy composition*, whereas the R_2 line shows identical behavior for β-Ga_2O_3 and AGO. The R_1 line can be used as a sensitive indicator of alloy composition in Ga_2O_3 and AGO.

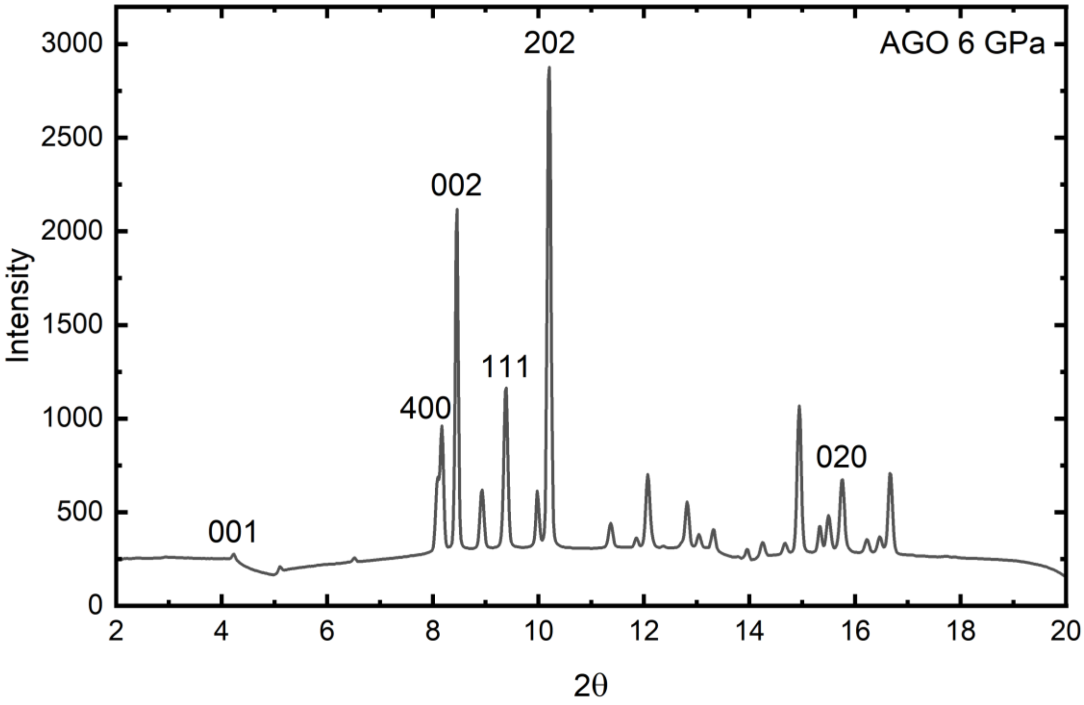

Figure 4.9: Labeled integrated XRD peaks for AGO at 6 GPa in methanol:ethanol.

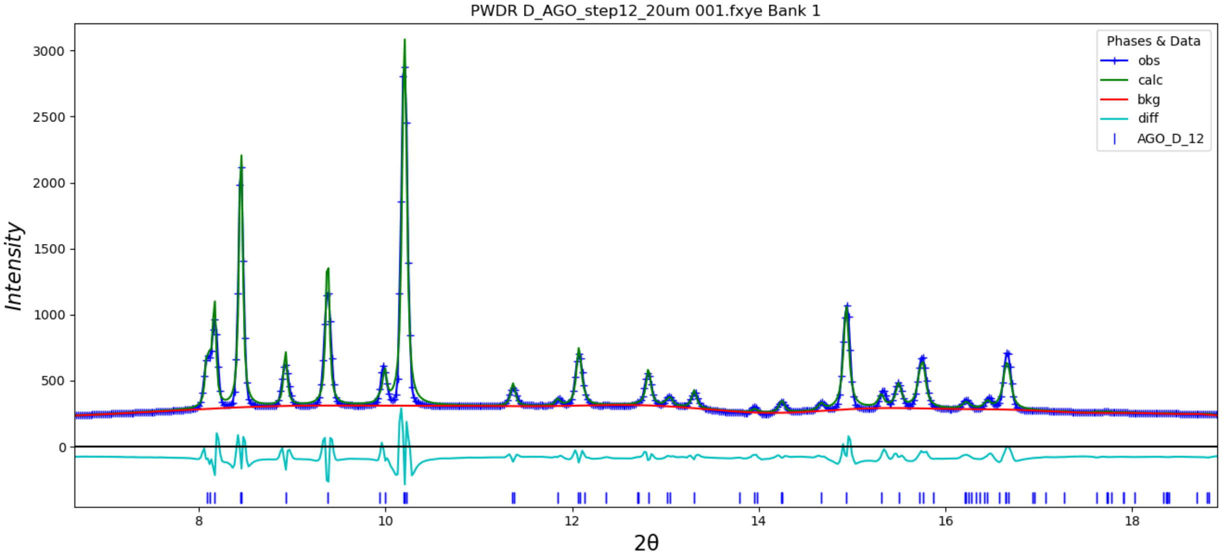

Figure 4.10: XRD data (obs), fitted curve (calc), and difference curve (diff) for AGO sample at 6 GPa in methanol:ethanol.

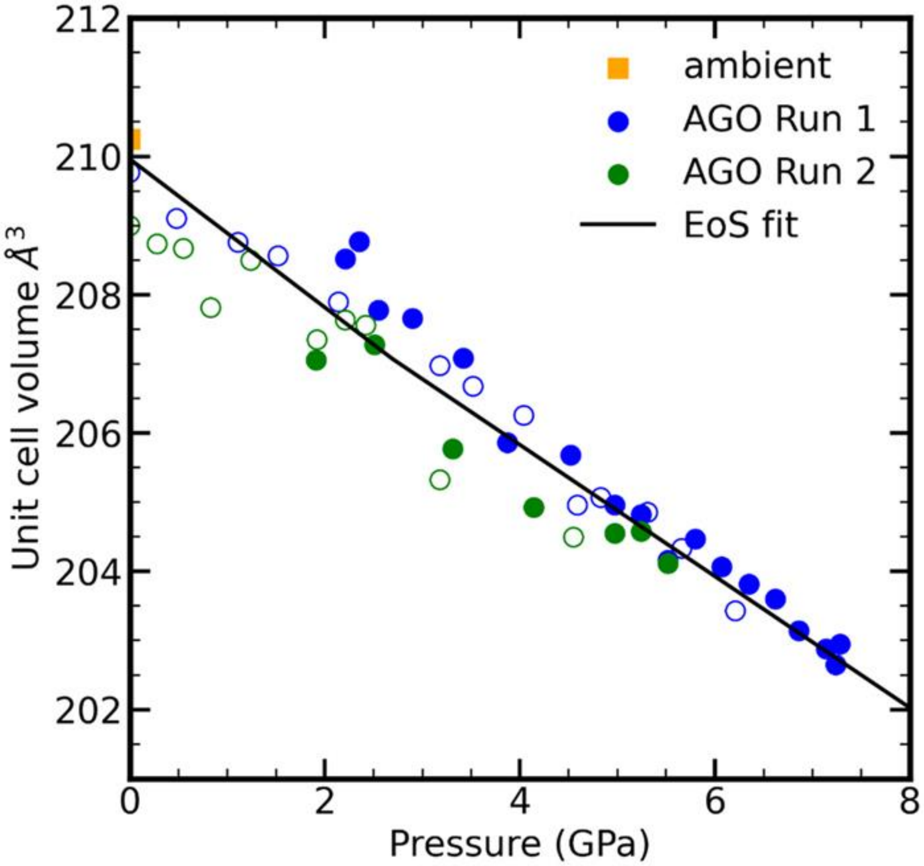

Figure 4.11: Unit cell volume versus pressure for both AGO experimental runs with the Birch-Murnaghan equation of state fit. Filled symbols are increasing pressure, open symbols are decreasing pressure. Ambient data point was acquired from AGO outside the DAC.

4.3 Nonhydrostatic compression of single crystal gallium oxide

4.3.1 Photoluminescence

Nonhydrostatic measurements were performed on Ga_2O_3 using mineral oil as a pressure-transmitting medium up to 11 GPa. While the R_2 line of Ga_2O_3 is relatively insensitive to nonhydrostatic stress, as is the case with ruby,[15] the R_1 line varies significantly within the Ga_2O_3 sample. Figure 4.12 shows data for spectra taken at several different locations on the sample. The large scatter for pressures above 2.5 GPa indicates the sensitivity of the R_1 line to nonhydrostatic stress.

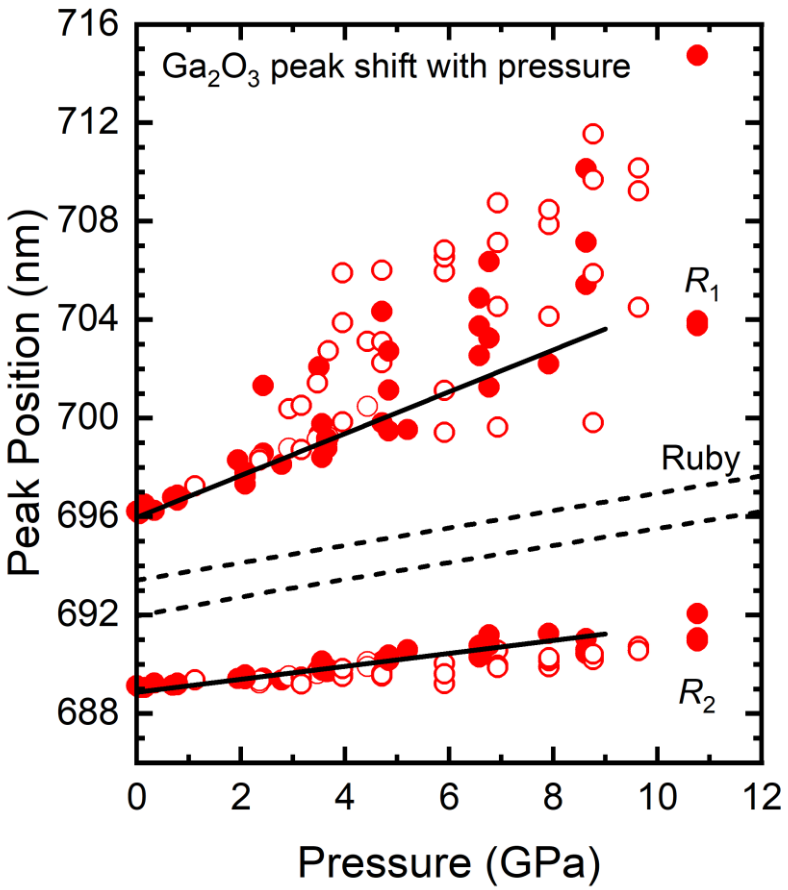

Figure 4.12: Peak position of R lines versus pressure in β-Ga_2O_3*:*Cr^{3+} *in mineral oil (multiple experimental runs shown). Dashed lines are the peak positions for hydrostatic compression of ruby.*[80] *Solid and open symbols refer to data collected after increasing or decreasing the pressure, respectively.*

4.3.2 Photoluminescence mapping

To further investigate the sensitivity of the R_1 line to nonhydrostatic stress, PL mapping was used to measure the PL spectra at many points across the sample. Under nonhydrostatic stress, these deviations were much more pronounced, resulting in large variations in the *R* line energy across the sample.

Figure 4.13 shows PL maps of a nonhydrostatic DAC experiment. The DAC was loaded with β-Ga_2O_3:Cr^{3+}, ruby spheres, and mineral oil as a pressure-transmitting medium. The cell was compressed to 7.9 GPa and PL mapping was performed. It should be noted that since the compression was nonhydrostatic, 7.9 GPa is an approximation obtained by measuring the ruby fluorescence lines inside the cell.

Figure 4.13(a) shows the energy of R_1 under nonhydrostatic stress, while image (b) shows the energy of R_2. The sample under nonhydrostatic stress shows significant variation in the energy of R_1 and some variation in the energy of R_2. Figure 4.14 shows representative spectra from the map in Figure 4.13(a), in which the energy of R_1 varies by 0.025 eV (10 nm) between spectra taken at the center and edge of the sample. Regions of equal stress are oriented along the *b* direction, which is the growth direction of the crystal. The stress gradients oriented perpendicular to the *b* direction are far more pronounced in the R_1 map than the R_2 map; i.e, the R_1 line is more sensitive to nonhydrostatic stress, as is the case with ruby.[15] These PL maps have much more inhomogeneity than those shown in Figure 4.3, which is the same material at the same pressure under hydrostatic stress.

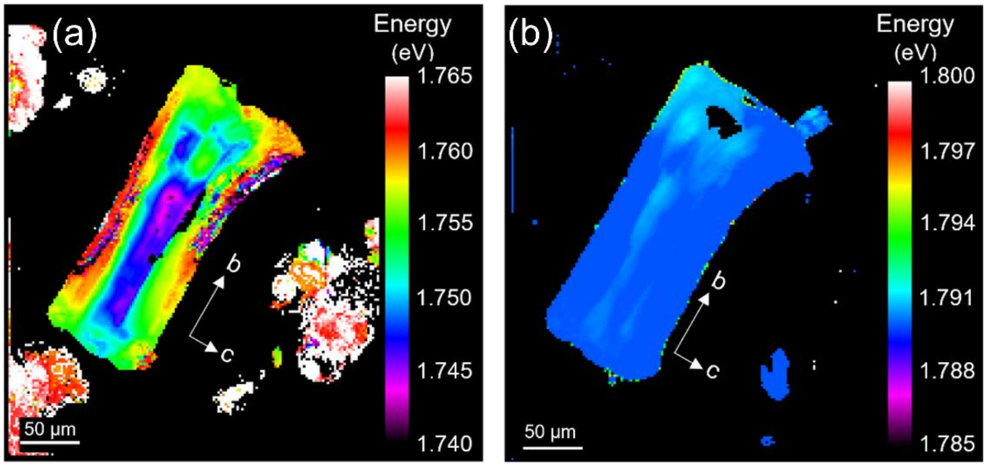

Figure 4.13: PL maps of β-Ga_2O_3:Cr^{3+} at 7.9 GPa with mineral oil (nonhydrostatic) as pressure medium. (a) map shows energy of R_1 peak. See spectra detail in Figure 4.14. (b) map shows energy of R_2 peak.

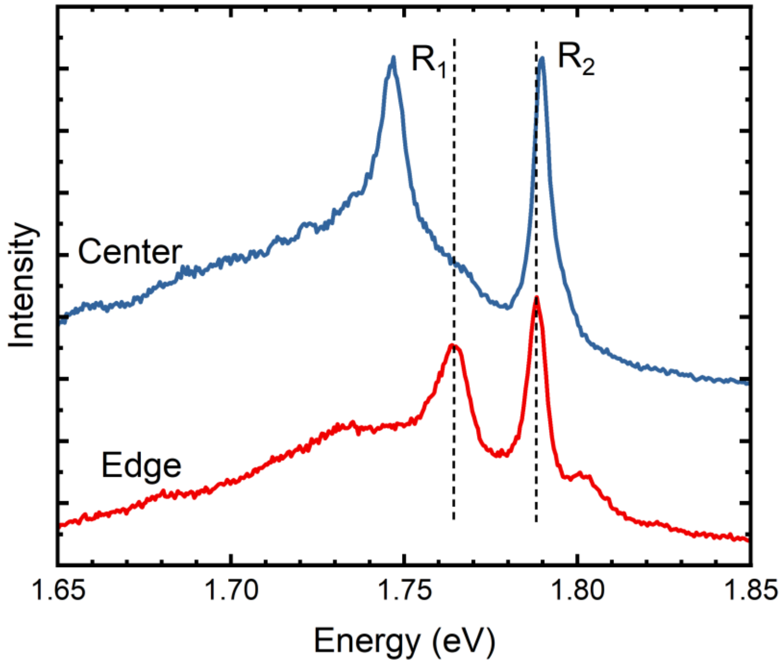

Figure 4.14: PL spectra detail from Figure 4.13(a) showing the variation in peak position from the center to the edge of the sample along the c axis under nonhydrostatic stress. Spectra offset vertically for clarity.

4.4 Nonhydrostatic compression of single crystal AGO

4.4.1 Photoluminescence

DAC experiments were performed on single crystal AGO up to 4.5 GPa using mineral oil as a pressure-transmitting medium, which is nonhydrostatic above 2.5 GPa. When examined under nonhydrostatic compression, AGO behaves similarly to β-Ga_2O_3:Cr^{3+}, with a linear peak shift below the hydrostatic limit and a large scatter for higher pressures (Figure 4.15). As is the case with Ga_2O_3, the R_1 line shift is more sensitive to nonhydrostatic stress than R_2, indicated by the larger change in peak position as the sample enters the nonhydrostatic regime.

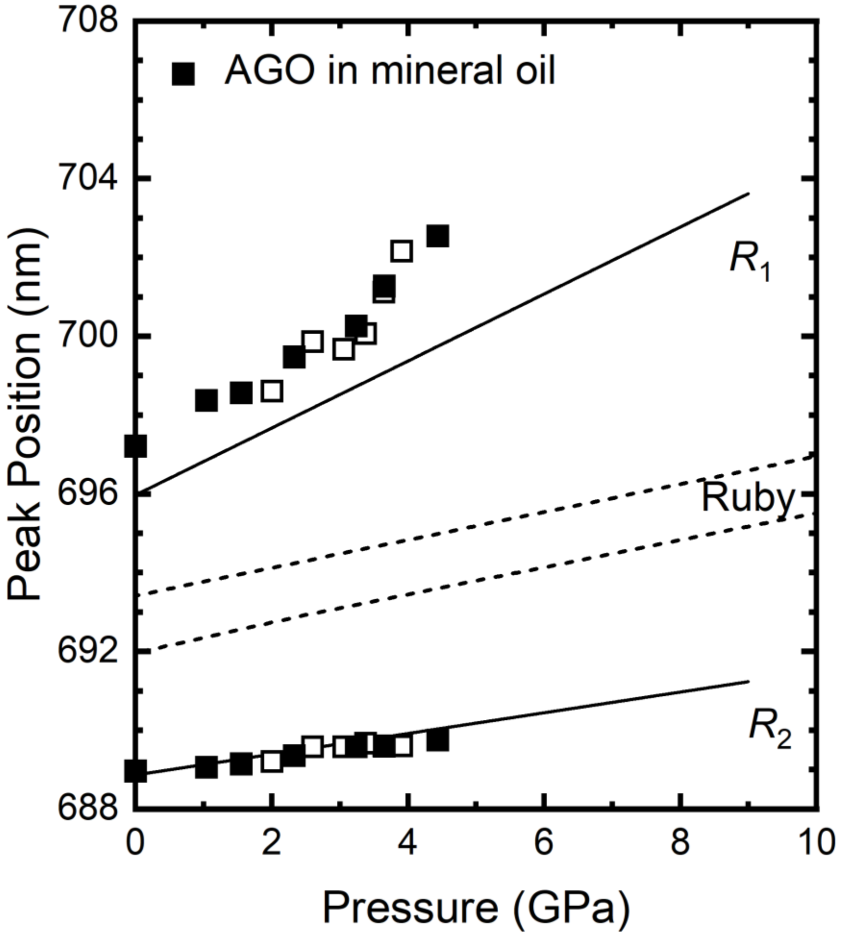

Figure 4.15: Peak position versus pressure for AGO in mineral oil. Solid black lines show the peak shift for Ga_2O_3*. Filled and open symbols represent measurements taken after increasing or decreasing pressure, respectively.*

4.4.2. Ambient photoluminescence mapping

As-grown AGO showed significant inhomogeneity in the Cr^{3+} emission intensity (Figure 4.16). To investigate this, PL mapping was performed on a sample of O_2-annealed AGO under ambient conditions. The *R* lines showed the highest intensity along grain edges and defects on the surface of the sample.Figure 4.16 shows the intensity of the R_2 peak only since it displays stronger intensity at ambient pressure than R_1. It is possible that these locations have higher concentrations of chromium ions in the 3+ charge state if the oxygen introduced during the anneal was better able to penetrate the sample at these defect locations. Samples for DAC experiments were chosen from brightly emitting regions for both O_2-annealed and Cr-diffused AGO samples.

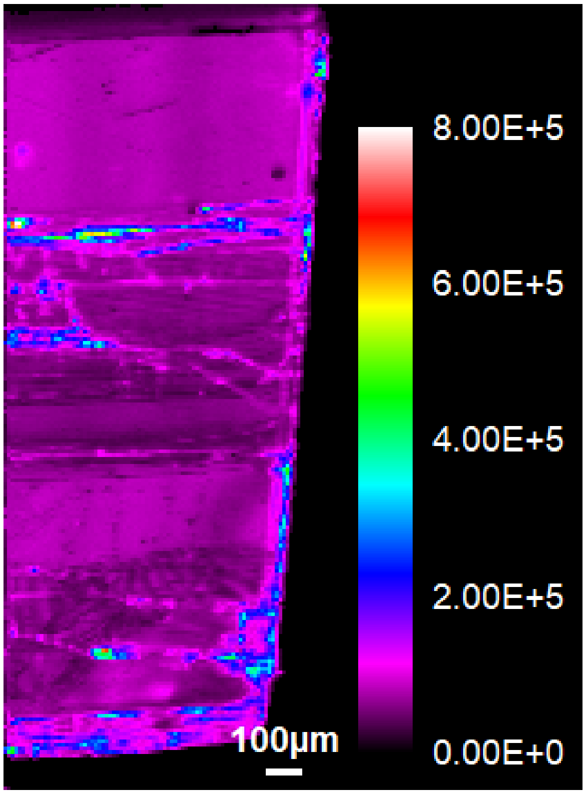

Figure 4.16: PL map of the intensity of the R_2 line in ambient AGO. A false-color intensity scale (arbitrary units) is shown on the right. Note the strongest luminescence along surface defects.

4.5 Pressure dependence of peak intensities in Ga_2O_3 and AGO

As pressure increases, the intensity of the R_1 peak increases relative to R_2. The change in relative intensity of the R_1 and R_2 lines was examined through the integrated peak area ratios. The area of the R_1 and R_2 peaks were measured and the R_2/R_1 intensity ratio was plotted against pressure. Taking the ratio eliminates overall changes in intensity and allows us to focus on the relative intensity of the two peaks. As shown in Figures 4.17 and 4.18, the peak ratio decreases by a factor of 4 in the pressure range studied. An Arrhenius equation for thermal population does not account for this large decrease. To explain the effect, it is necessary to invoke nonradiative recombination.

The peak area ratios as a function of pressure were fit using nonlinear least-squares fitting as in the previous chapter to the following equation:[42]

$$I_{\frac{R_2}{R_1}}(P) = A\, e^{\frac{-E}{kT}} \left(\frac{1 + A_1 e^{\frac{-E_1}{kT}}}{1 + A_2 e^{\frac{-E_2}{kT}}} \right), \tag{9}$$

$$E = 0.01841 + 0.00147 \times P,$$

$$E_1 = E_1(0) + B \times P,$$

$$E_2 = E_2(0) + C \times P,$$

where P is pressure (GPa) and E is the measured line splitting energy as a linear function of pressure. E_1 and E_2 are the pressure-dependent activation energies of the nonradiative recombination channels for R_1 and R_2, respectively. The fit parameters are A, B, and C (Table 4.1). The zero-pressure values $E_1(0)$ and $E_2(0)$, as well as A_1 and A_2, are the values previously obtained from peak area ratio versus temperature fitting (Chapter 3 and Reference 42).

This fit (Equation 9) is the same model used in Chapter 3 to model nonradiative recombination as a function of varying temperature. This model is also valid in the case of varying pressure and for both Ga_2O_3 and AGO, since the same physical process of nonradiative recombination is occurring. Since temperature is constant in this case, the fit parameters have been altered to allow the activation energies E_1 and E_2 to vary linearly with pressure.

	β-Ga_2O_3:Cr^{3+}	**AGO**
A	132.35	50.41
B	0.0047	0.011
C	-0.0026	0.0053
A_1 *	9.9	37.4
A_2 *	50.2	302.3
$E_1(0)$ (eV) *	0.0593	0
$E_2(0)$ (eV) *	0.0166	0.0065

Table 4.1: Fit parameters for peak area ratios versus pressure. Parameters with asterisks are from Reference 42.

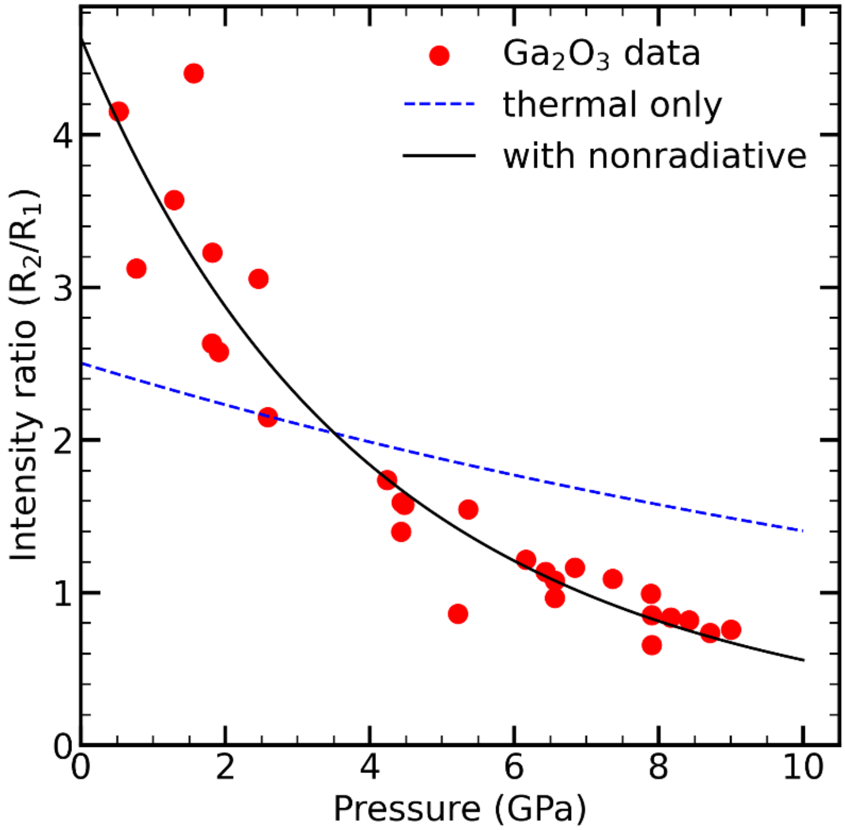

Figure 4.17: Peak area intensity ratio (R_2/R_1) versus pressure for β-Ga_2O_3:Cr^{3+}. The dashed line shows the thermal population Arrhenius fit only, while the solid line shows the fit with thermal population and nonradiative recombination (Equation 9). Fit parameters are listed in Table 4.1.

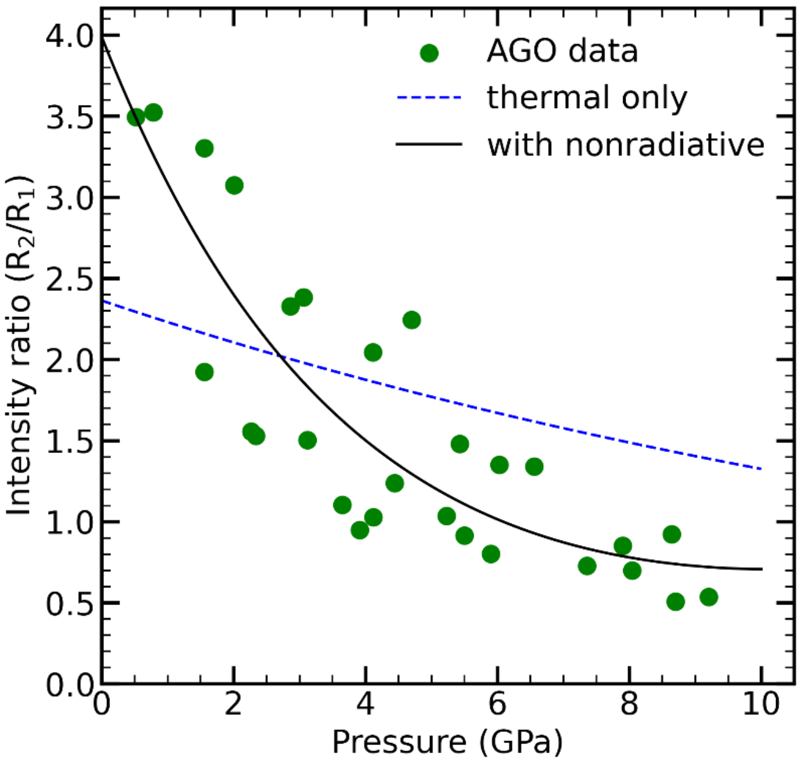

Figure 4.18: Peak area intensity ratio (R_2/R_1) versus pressure for AGO. The dashed line shows the thermal population Arrhenius fit only, while the solid line shows the fit with thermal population and nonradiative recombination (Equation 9). Fit parameters are listed in Table 4.1.

In both β-Ga_2O_3:Cr^{3+} and AGO, the relationship between peak intensities and pressure is dominated by nonradiative recombination and cannot be explained by thermal population alone. At ambient pressure, the R_2 peak has a higher intensity than R_1. The intensity area of R_1 surpasses that of R_2 at ~6 GPa for both materials. The pressure dependent components of the activation energies (B and C) are positive except for C in β-Ga_2O_3:Cr^3.

A potential pathway for the nonradiative recombination in Ga_2O_3 and AGO is shown in Figure 4.19. In this model, electrons in the ^2E state, which is split into R_1 and R_2, must overcome a thermally activated energy barrier to move to the $^4T_2$ state. These energy barriers are represented by E_1 and E_2 and the values are found by fitting to Equation 9. The $^4T_2$ state can decay radiatively, which causes a broad background in the spectrum, or nonradiatively decay to return to the ground state. The activation energies E_1 and E_2 are temperature and pressure dependent. At lower pressures, the nonradiative recombination pathway is more favorable and we see a lower R line luminescence and stronger background. As pressure increases, the activation energies increase, which depopulates the $^4T_2$ state and causes the R line luminescence to increase and the background to be suppressed.

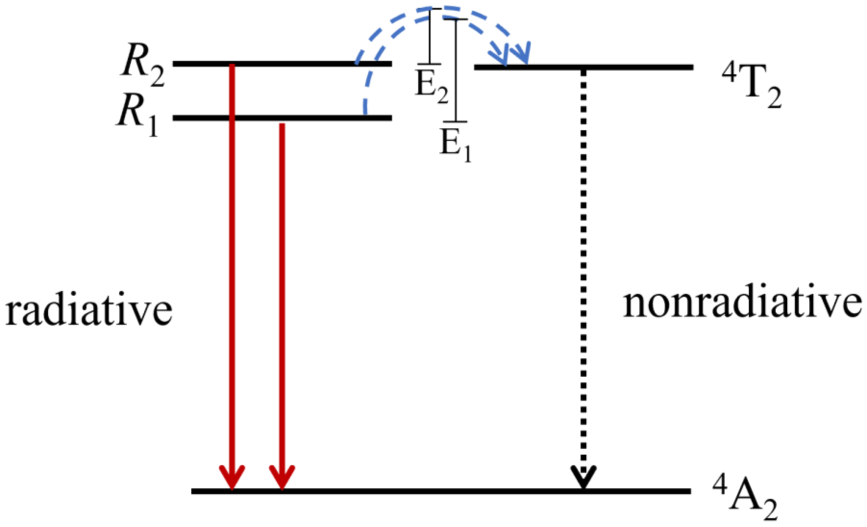

Figure 4.19: Simplified illustration of a possible nonradiative recombination pathway in Ga_2O_3 and AGO. Electrons overcome a thermally activated energy barrier to move to the $^4T_2$ state, then undergo nonradiative decay to return to the ground state.

4.6 Discussion

This work has examined the Cr^{3+} R lines in powder and single crystal gallium oxide and aluminum gallium oxide. The response of the Cr^{3+} R lines in β-Ga_2O_3 to hydrostatic pressure showed significant differences from ruby (Al_2O_3:Cr^{3+}). The R_1-R_2 splitting, which arises due to the crystal field and spin-orbit coupling, is larger in β-Ga_2O_3 and increases further with applied pressure. A similar effect was observed in AGO. However, the R_1 line in AGO shows a smaller shift versus pressure compared to Ga_2O_3, indicating that the R_1 peak shift is sensitive to alloy composition. X-ray diffraction measurements indicate that the AGO equation of state is similar to that of β-Ga_2O_3. Nonradiative recombination contributes significantly to the pressure-dependent intensity of the R lines in both β-Ga_2O_3:Cr^{3+} and AGO. As pressure is increased, the $^4T_2$ state becomes depopulated due to increasing activation energies, which causes the R line luminescence to increase and the background to be suppressed.

β-Ga_2O_3:Cr^{3+} and AGO were examined under nonhydrostatic conditions by using mineral oil as a pressure-transmitting medium, which is nonhydrostatic above ~2.5 GPa. The R_1 line is much more sensitive to nonhydrostatic stress than R_2 in both materials. Spatially resolved PL of a β-Ga_2O_3:Cr^{3+} sample at 8 GPa in mineral oil showed significant variations in the R_1 emission wavelength across the sample, while a sample under hydrostatic pressure showed homogenous emission wavelengths. These results suggest that the position of the R_1 line of β-Ga_2O_3:Cr^{3+} could serve as a sensitive indicator of nonhydrostatic stress.

CHAPTER FIVE: PRESSURE-TRANSMITTING MEDIA

As discussed in Chapter 2, methanol:ethanol was used as a hydrostatic pressure-transmitting medium while mineral oil resulted in nonhydrostatic stress. This chapter details the study of pressure-transmitting media, including the hydrostatic limits of mineral oil and heptane, and evidence of a previously unreported solid-solid phase transition in heptane under pressure. PL results from experiments on gallium oxide in heptane are also reported.

5.1 Mineral oil hydrostatic limit

Although mineral oil has been used as a pressure-transmitting medium in DACs at low pressures,[131–134] the hydrostatic limit of this fluid has not been established in the literature. To address this, experiments were performed to determine the hydrostatic limit of mineral oil. The mineral oil used in this work was sourced from Sigma-Aldrich (see Appendix C for product specifications). A DAC was loaded with several ruby spheres and mineral oil, and the position of both R lines were measured for all ruby spheres at each pressure increment. The pressure indicated by each ruby sphere was determined using the ruby standard[81] and the standard deviation σ of pressures measured by all ruby spheres was calculated. The criterion used for nonhydrostaticity is the standard deviation σ of the pressures P_i as indicated by N ruby spheres, where $\bar{P}$ is the average pressure.[110]

$$\sigma = \sqrt{\frac{1}{N}\sum_{i=1}^{N}(P_i - \bar{P})^2}$$

When the stress is purely hydrostatic, $\sigma = 0$ since all ruby spheres indicate the same pressure. For nonhydrostatic stress, the ruby spheres show a variance in pressure across the sample chamber, resulting in σ > 0. In mineral oil, beyond 2.5 GPa, the *R* lines for the different ruby spheres showed significant deviation (Figure 5.1), which is a signature of nonhydrostatic stress.

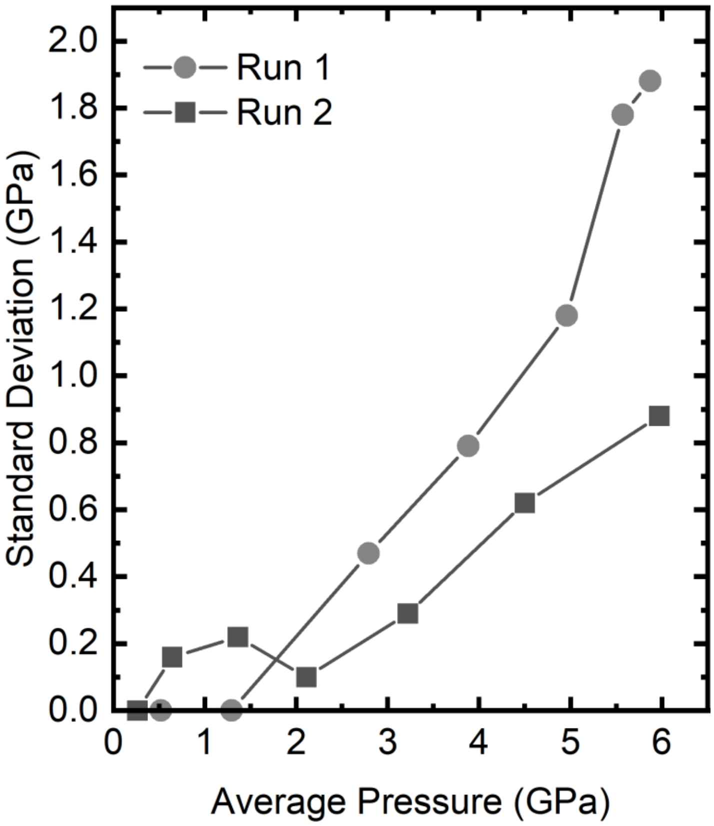

Figure 5.1: Pressure dependence of the standard deviation σ for mineral oil. Above ~2.5 GPa, the standard deviation of pressures increases significantly, indicating nonhydrostaticity.

The *R* line widths or the R_1-R_2 splitting were not used as indicators of nonhydrostaticity, since the positions of the *R* lines of multiple rubies are a more sensitive and reliable indicator.[110] Indeed, the R_1-R_2 splitting for these randomly oriented ruby spheres is constant up to 7 GPa, while the standard deviation of the pressures indicate nonhydrostaticity well below that pressure. The *R* line splitting versus average *R* line wavelengths for mineral oil can be plotted (Figure 5.2) and the slope of a linear fit to the data does not vary significantly from zero, indicating that the *R* line splitting does not change significantly even as mineral oil goes into its nonhydrostatic regime.

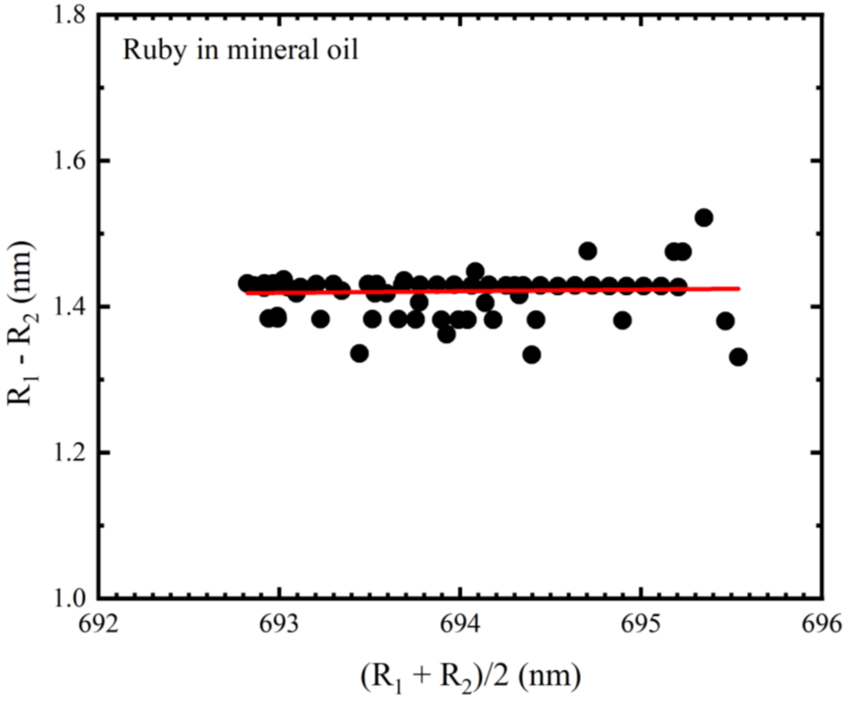

Figure 5.2: R_1 vs R_2 wavelength for ruby in mineral oil up to 7 GPa. The R line splitting is constant despite nonhydrostatic effects appearing above ~2.5 GPa.

5.2 Heptane

Heptane, also known as *n*-heptane, is straight-chain alkane with the chemical formula $H_3C(CH_2)_5CH_3$ or C_7H_{16}. It is a colorless liquid at ambient temperature and pressure and is used in fuel as a component of gasoline and as a laboratory solvent.[135–138] Heptane is used in high pressure physics experiments as a pressure-transmitting medium,[139,140] though its hydrostatic limit has not been established in the literature.

5.2.1 Hydrostatic limit

DAC experiments were performed on heptane to determine its hydrostatic limit, using the same process as for mineral oil. As indicated by the increase in standard deviation of pressures as measured by multiple ruby spheres (Figure 5.3), nonhydrostatic effects in heptane increase at approximately 3.5 GPa. It appears that the nonhydrostatic effects start small and gradually increase with increasing pressure. The hydrostatic limit of 3.5 GPa occurs where heptane is in its solid phase, as heptane freezes at 1.2 GPa.[141,142] Evidently, the solid phase remains viscous enough at lower pressure to serve as a hydrostatic medium below 3.5 GPa.

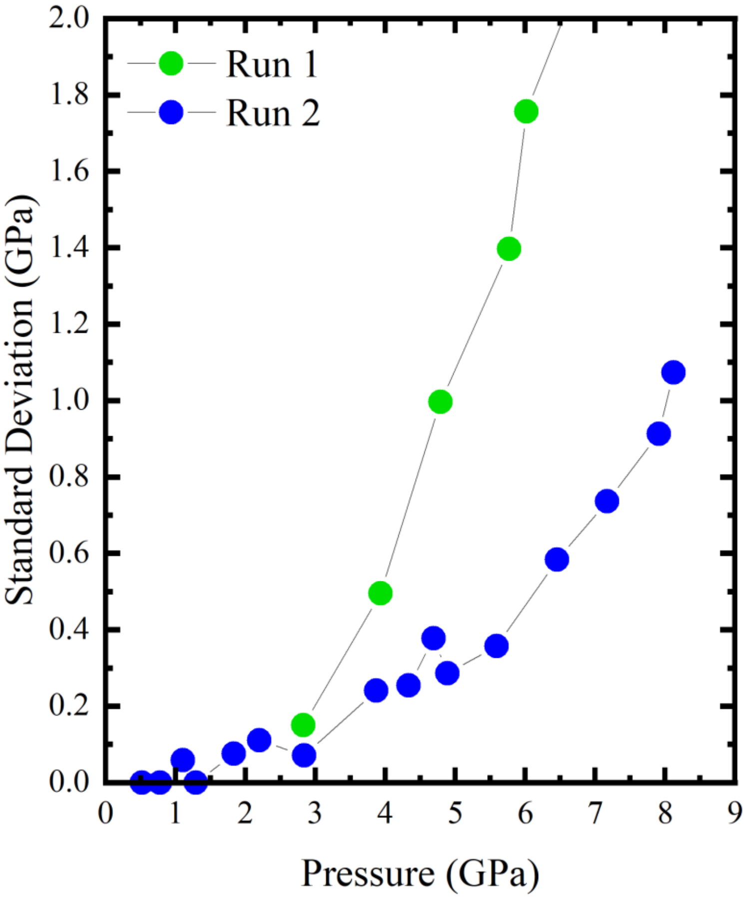

Figure 5.3: Pressure dependence of the standard deviation σ for heptane. Above ~3.5 GPa, the standard deviation of pressures increases significantly, indicating nonhydrostaticity.

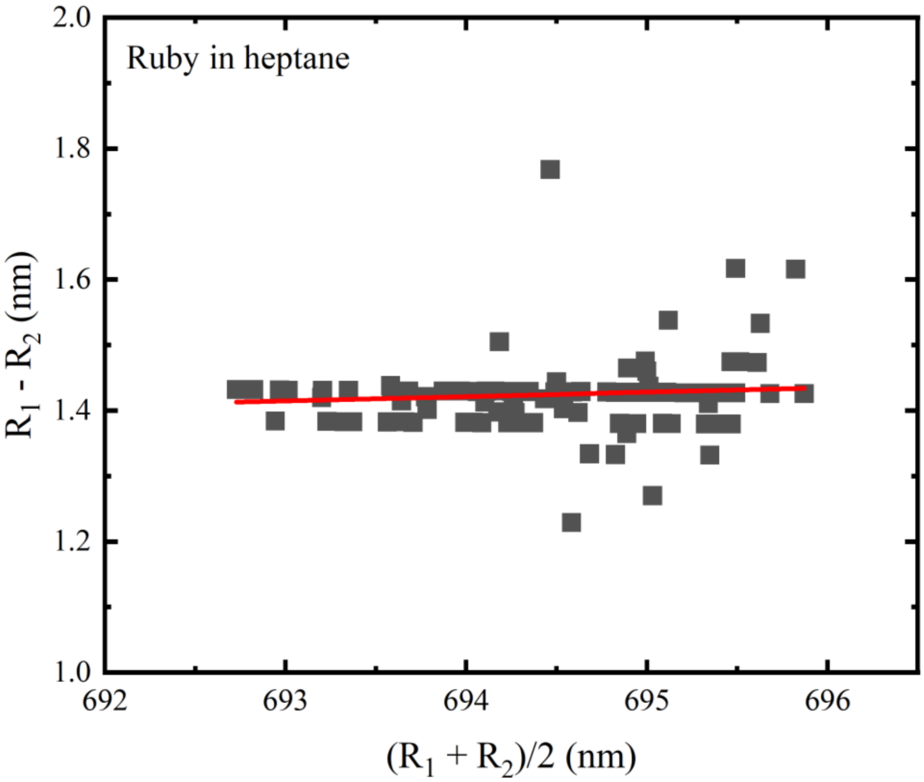

Figure 5.4: R line splitting versus average R line wavelength for ruby in heptane up to 8 GPa.

As with mineral oil, the R_1-R_2 splitting is constant up to 8 GPa despite the onset of nonhydrostatic behavior. The *R* line splitting versus average *R* line wavelengths for heptane was plotted (Figure 5.4) and the slope of a linear fit to the data does not vary significantly from zero, indicating that the *R* line splitting does not change significantly even as heptane goes into its nonhydrostatic regime.

5.2.2 X-ray diffraction

5.2.2.1 Previous work

X-ray diffraction (XRD) experiments were conducted at the Advanced Light Source at Berkeley National Laboratory, beamline 12.2.2[115] by Anya Guy.[143] Samples of n-heptane were loaded into a DAC along with ruby microspheres for in situ pressure measurement using the Mao scale[80] with an estimated precision of 0.1 GPa. The sample was initially compressed to 1.7 GPa and spectra were collected during both loading and unloading using a wavelength of 0.4959 Å and a high resolution MAR3450 plate detector. The XRD data were collected by Anya Guy,[143] and I integrated and analyzed the XRD data.

Heptane has a liquid to solid phase transition at 1.2 GPa.[141,142] Ma et al[111] reported observations of a new peak in the XRD spectra appearing at a d-spacing of ~2.30 Å, attributed to a rotator-rotator phase transition of heptane under pressure at approximately 3 GPa. This phase transition was also observed by Yamaguchi et al.[144] The group also reported two additional peaks at approximately 7.5 GPa, which they considered to be the onset of a rotator-crystalline transition. Kavitha and Narayana[145] observed a change in the Raman modes, suggesting a solid-to-solid phase transition at 7.5 GPa. They stated that because no hysteresis was observed in this transition, there was no volume change or it was a second-order phase transition.

Our XRD spectra for heptane display these peaks (Figure 5.5) that Ma et al. considered to be indicators of the two phase transitions. However, the presence of these peaks in our spectra at pressures below 3 GPa contradict their findings. No XRD evidence was found to support a rotator-rotator transition in n-heptane below 4 GPa.[143] This conclusion is supported by molecular dynamics simulations, which conclude that there is no first-order solid-to-solid phase transition below 7 GPa.[146]

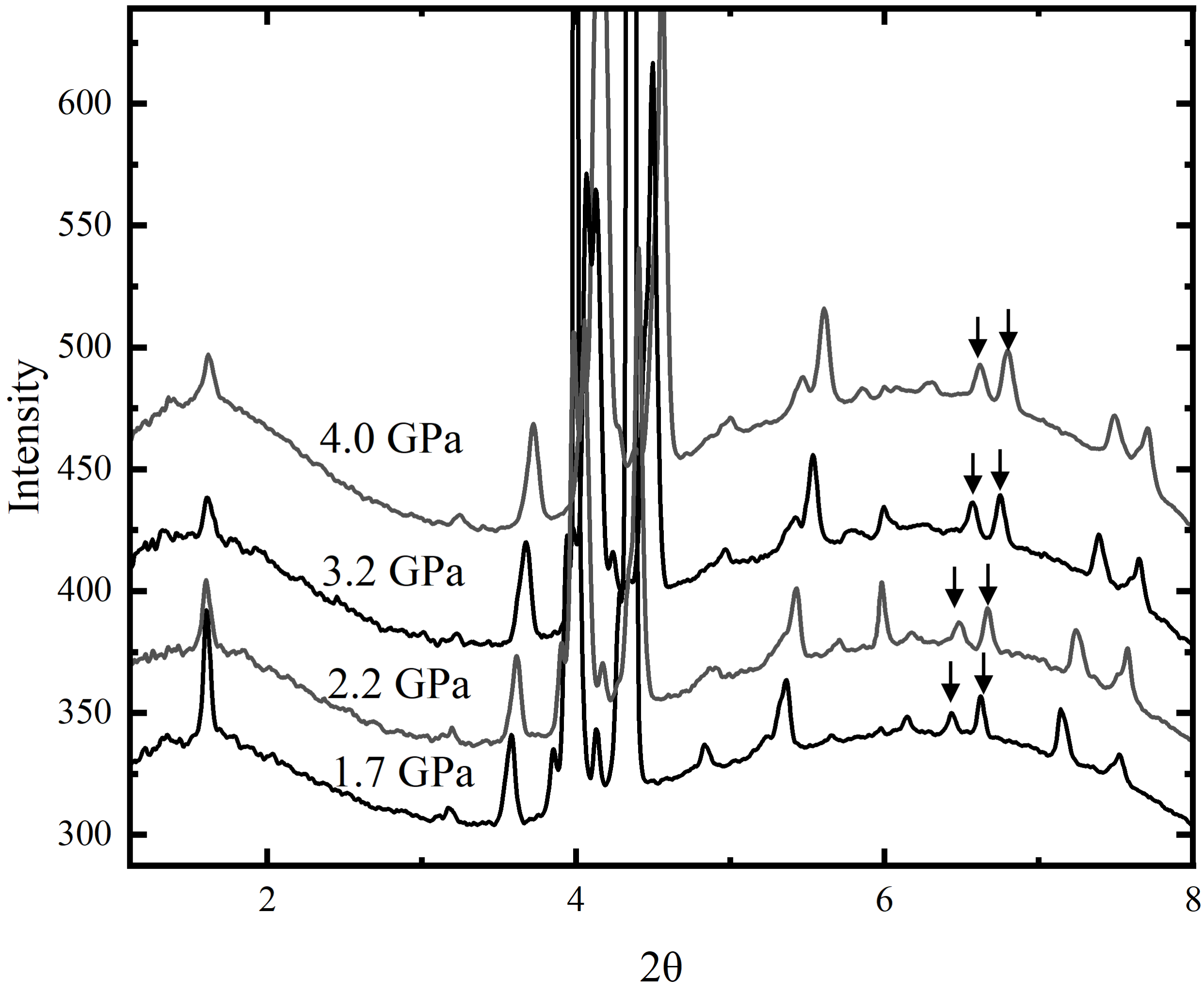

Figure 5.5: Integrated XRD spectra for heptane at elevated pressures. Arrows note the peaks that Ma et al.[111] *considered to be indicative of a phase transition.*[143]

5.2.2.2 Le Bail fitting

To further examine the behavior of heptane under compression, I performed Le Bail fitting on the spectra in order to determine the unit cell parameters and volume. The XRD spectra were integrated and the Le Bail refinement was performed in GSAS-II.[120] The initial refinement used the ambient heptane unit cell parameters $a = 4.15$ Å, $b = 19.97$ Å, $c = 4.69$ Å,[147] and each subsequent step was refined from the previous step in an iterative process as the sample underwent compression. Two experimental runs of heptane from 0 to 10 GPa were collected by Anya Guy and analyzed by me for this work. The unit cell volume versus pressure that I obtained from Le Bail fitting is plotted in Figure 5.6. The $P\bar{1}$ space group phase fit the data well across the entire pressure range.

Of particular interest are the lowest pressure data points in Figure 5.6. These data were collected after decreasing the DAC cell pressure below the heptane solid-to-liquid transition limit, then increasing it slightly to return to the solid phase. The slope of these points more closely matches with the ambient unit cell volume, and there is a discontinuity between these points and the higher pressure (>2 GPa) phase. This indicates that the lower pressure points are a unique phase in the 1.2-1.9 GPa range, just above the liquid-to-solid phase transition. This phase transition occurs below the hydrostatic limit of heptane.

I fit the heptane unit cell volume versus pressure data with a Birch-Murnaghan equation of state, with K_0' fixed at 4:

$$P = \frac{3}{2}K_0\left[\left(\frac{V_0}{V}\right)^{\frac{7}{3}} - \left(\frac{V_0}{V}\right)^{\frac{5}{3}}\right]$$

The resulting fit parameters are $K_0 = 14.5 \pm 1.2$ GPa and $V_0 = 351.9 \pm 5.0$ Å^3. The low bulk modulus is in line with heptane being a very soft solid, enough that it can provide hydrostatic pressure in its solid phase below its hydrostatic limit.

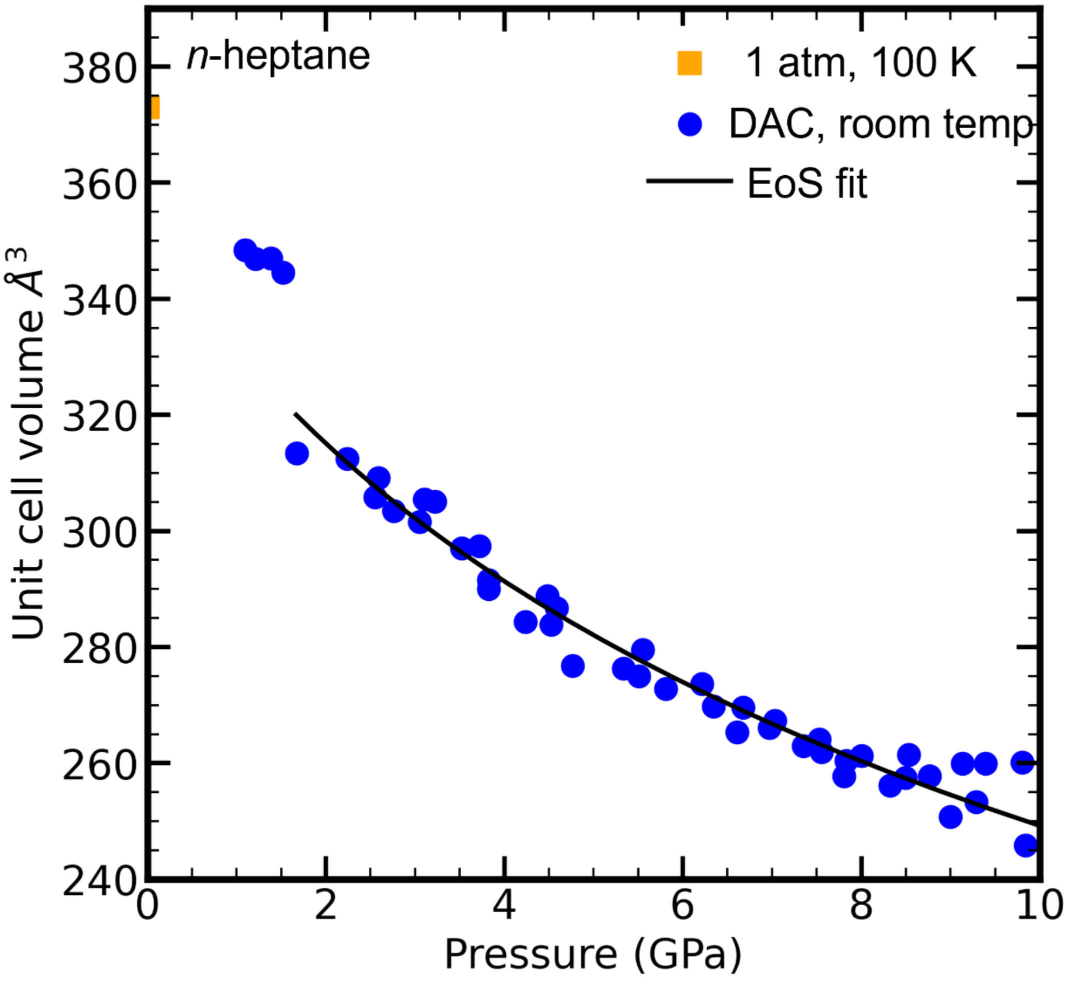

Figure 5.6: Unit cell volume versus pressure for heptane XRD. Ambient data from Ref. 147. Raw XRD data was collected by Anya Guy. I performed the integration, Le Bail fitting to obtain unit cell volume, and Birch-Murnaghan equation of state fitting.

5.2.3 Heptane FTIR spectroscopy

Further evidence to support this phase transition in heptane comes from Fourier transform infrared spectroscopy. Initial FTIR spectroscopy experiments on heptane were performed by Ben Whitfield. I replicated these experiments and performed the fitting and analysis. As discussed in Chapter 2, heptane has two peaks in the IR spectrum (Figure 5.7) that shift approximately linearly with increasing pressure. These peaks, which correspond to combinations of vibrational modes, enable the use of heptane use as a pressure sensor as well as a pressure-transmitting medium. The two peaks display an abrupt frequency shift (Figure 5.8) at 1.5 GPa, the same pressure as the onset of the phase transition detected by XRD. The peak shift is linear below 1.5 GPa, with the linear fits found to be:

$$k_{Peak\ 1}\ (\mathrm{cm}^{-1}) = 4257.4(8) + 10.9(2)\ P\ (\mathrm{GPa})$$

$$k_{Peak\ 2}\ (\mathrm{cm}^{-1}) = 4331.7(6) + 14.0(2)\ P\ (\mathrm{GPa})$$

Above 2 GPa, the peak shifts were fit with third-order polynomial curves:

$$k_{Peak\ 1}\ (\mathrm{cm}^{-1}) = 4265(1) - 1(1)P + 3.6(4)P^2 - 0.29(4)P^3$$

$$k_{Peak\ 2}\ (\mathrm{cm}^{-1}) = 4334(1) + 9(1)P + 1.8(5)P^2 - 0.18(4)P^3$$

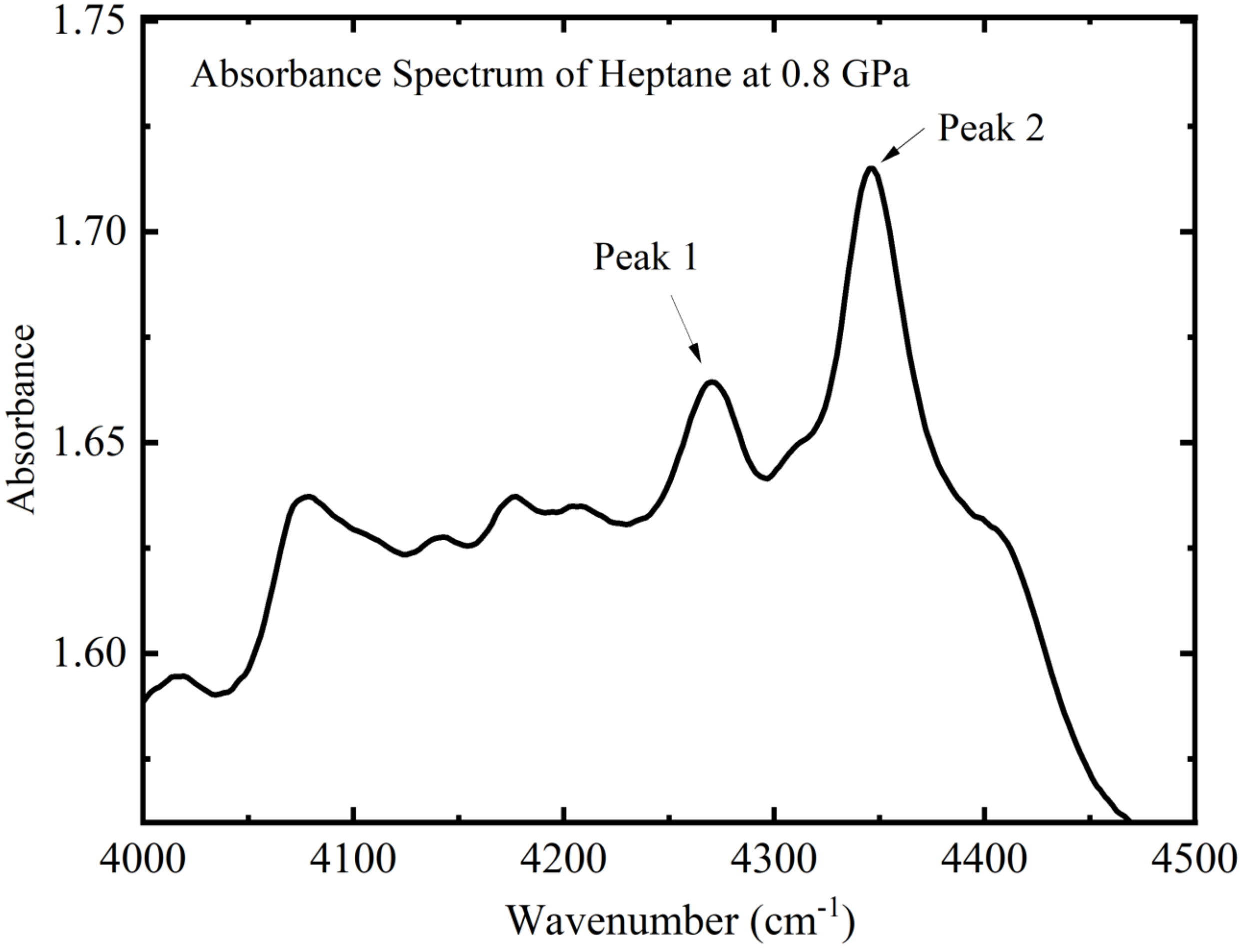

Figure 5.7: Infrared absorbance spectrum of heptane at 0.8 GPa. Spectra collected by Ben Whitfield.

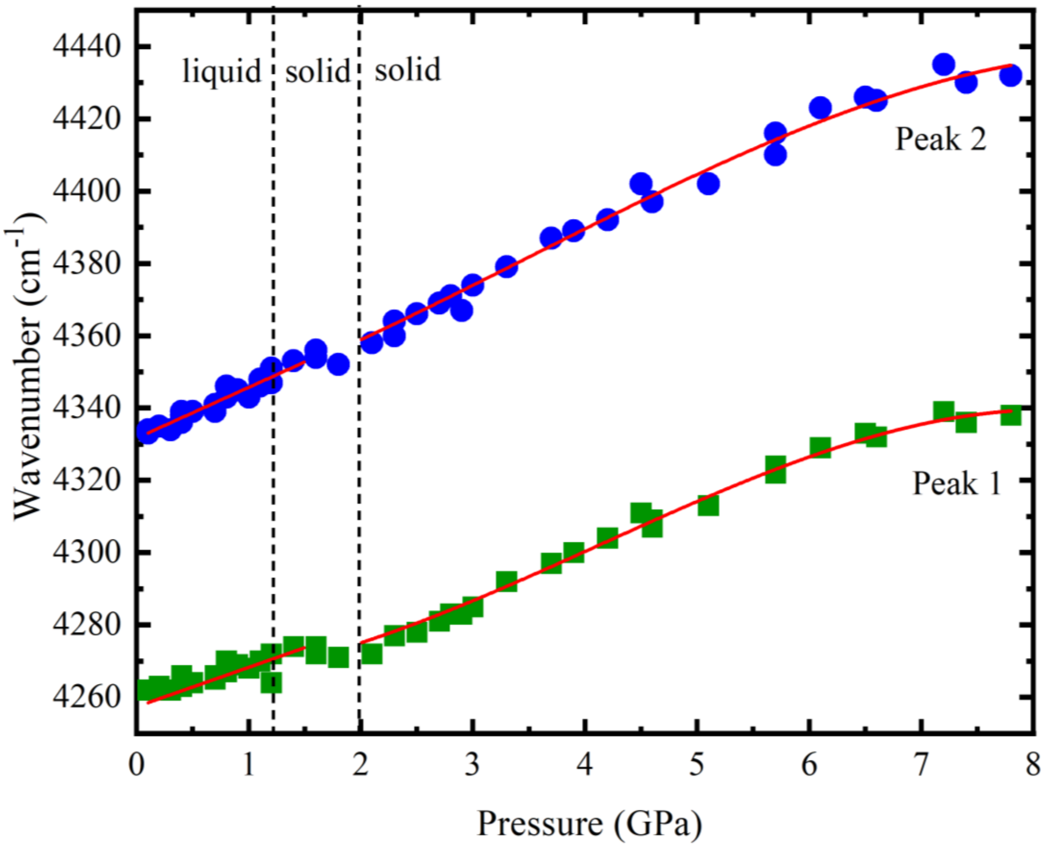

Figure 5.8: IR peak positions versus pressure in heptane.

5.2.4 Gallium oxide in heptane

Both powder and single crystal samples of gallium oxide (β-Ga_2O_3) were studied under pressure with heptane as the pressure-transmitting medium. These experiments were performed to test the use of heptane as a pressure sensor with powder Ga_2O_3, and to examine the effects of heptane as a secondary nonhydrostatic pressure transmitting fluid in addition to mineral oil on single crystal Ga_2O_3.

5.2.4.1 Powder

The PL spectra of powdered Ga_2O_3 was measured in ambient conditions and under pressure in mineral oil and heptane. Alternate pressure sensors (mineral oil and heptane) were used for these experiments. The powder was not intentionally doped with chromium, so the Cr^{3+} ions are present only as an unintentional dopant. The peak shift in powder Ga_2O_3 is similar to that of single crystal Ga_2O_3, with deviations occurring above the hydrostatic limit of the pressure-transmitting media.

In powder Ga_2O_3 in heptane (Figure 5.9), the *R* lines exhibited a larger wavelength scatter than in 4:1 methanol:ethanol, particularly at pressures greater than 4.5 GPa. This is likely due to the higher uncertainties from using heptane as a pressure sensor, as well as the nonhydrostatic effects above heptane's hydrostatic limit.

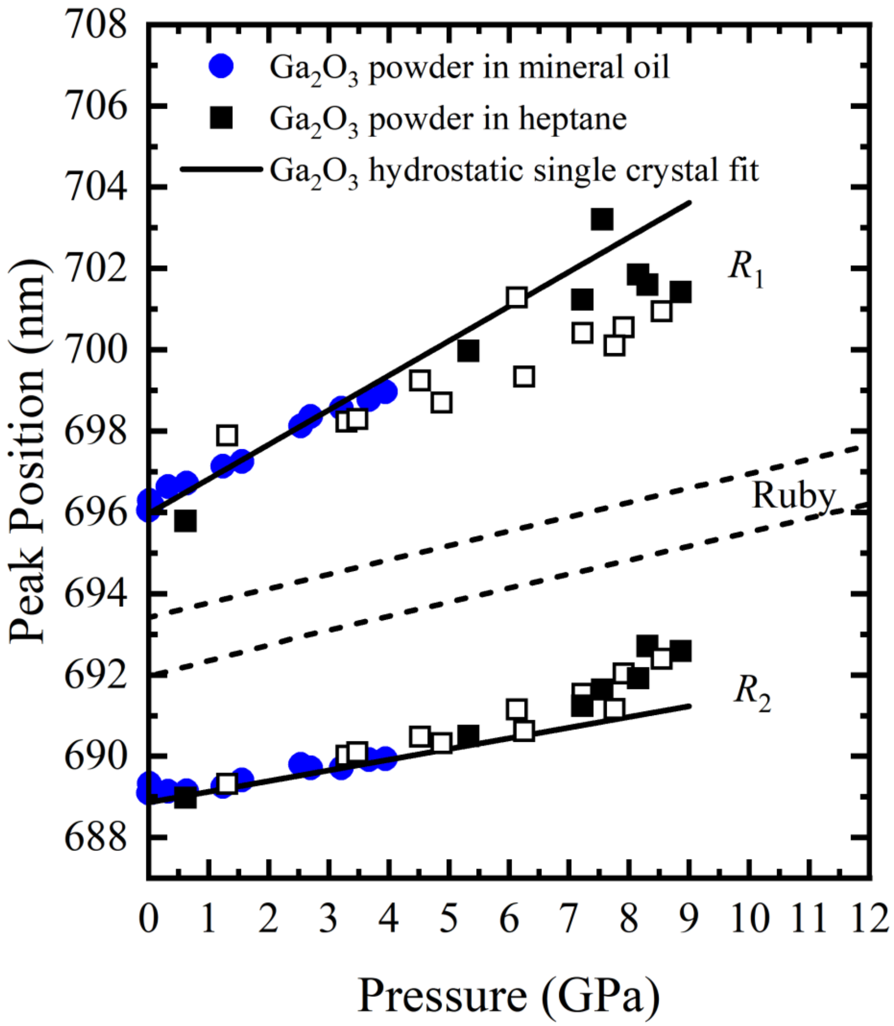

Figure 5.9: R line peak positions versus pressure for gallium oxide powder in heptane (black squares) and mineral oil (blue circles) Filled symbols indicate data taken upon increasing pressure; open symbols indicate data taken upon decreasing pressure. The solid black line is the peak shift from gallium oxide under hydrostatic compression in methanol:ethanol for comparison.

5.2.4.2 Single crystal gallium oxide

Single crystal β-Ga_2O_3:Cr^{3+} was loaded into a DAC with ruby spheres and heptane and compressed (Figure 5.10). At ~3.5 GPa, a new peak appeared in the Ga_2O_3 spectrum between the standard R lines near R_1 (Figure 5.11). The appearance of this peak coincides with the hydrostatic limit of heptane, where heptane is in its solid phase. This additional peak is likely due to the nonhydrostatic compression of Ga_2O_3. It was observed on both the compression and decompression. This peak was not visible when using any other pressure-transmitting medium. The appearance of this peak near R_1 provides further evidence that R_1 is more sensitive to nonhydrostatic stress in Ga_2O_3 than R_2.

In one experimental run, the R_1 and R_2 lines broadened and combined into a single peak. This occurred when increasing the sample pressure to 9.4 GPa, where the two peaks remained distinct, then decreasing the pressure to 8.3 GPa, below which the single broad peak appeared. It has been observed that the R_1 line becomes stronger relative to R_2 as pressure increases, but in this case the effect persists after decreasing the pressure back down as low as 3.3 GPa. This effect could be anomalous as heptane is well into its nonhydrostatic regime when the peaks combine in this case.

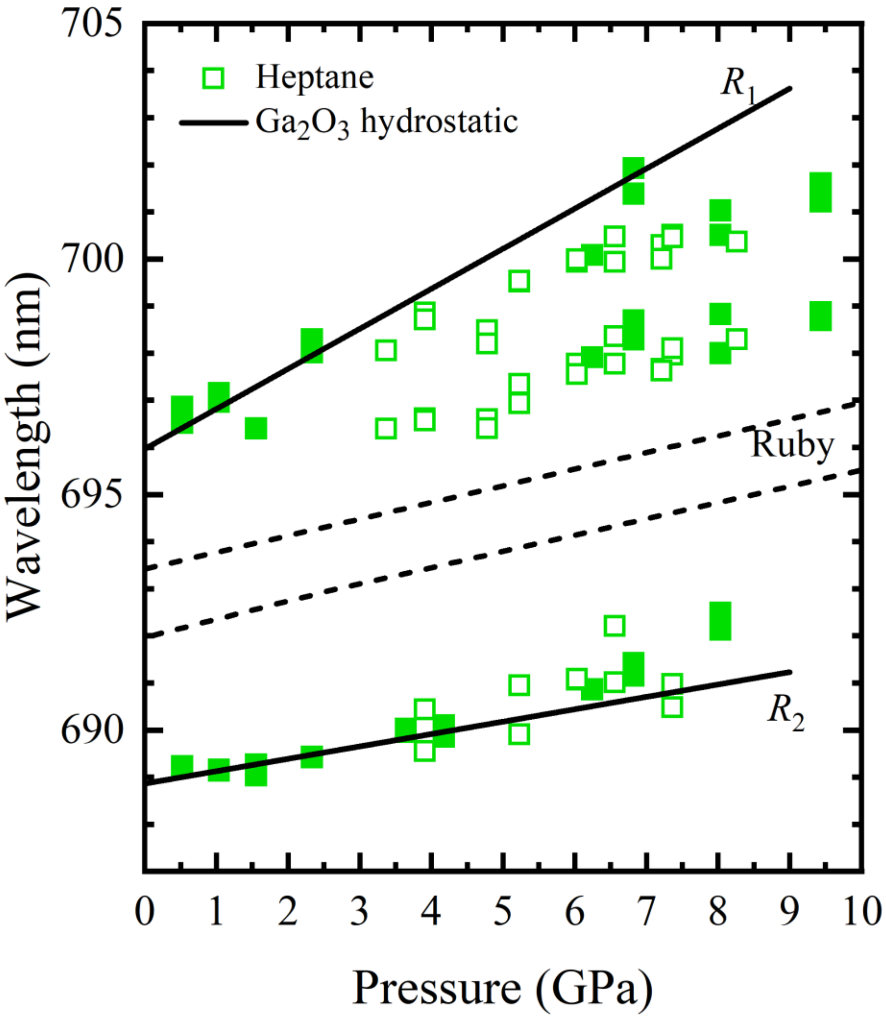

Figure 5.10: Ga_2O_3 R line positions versus pressure in heptane. Note the large spread in peak positions increasing above 3.5 GPa. Filled symbols indicate data taken upon increasing pressure; open symbols indicate data taken upon decreasing pressure.

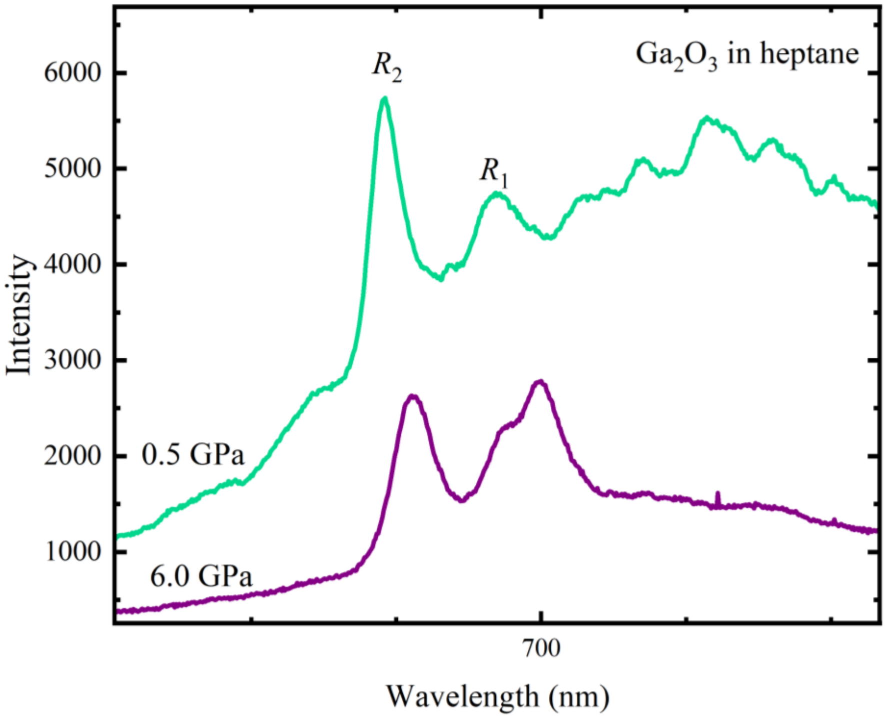

Figure 5.11: PL spectra of Ga_2O_3 *in heptane. The extra peak (small bump in the side of* R_1*) is visible at 6 GPa.*

5.3 Discussion

Mineral oil and heptane can be used as hydrostatic pressure-transmitting media up to 2.5 and 3.5 GPa, respectively. Above these pressures, it is no longer useful for hydrostatic pressure and may produce anomalous results, as was observed with Ga_2O_3 in heptane.

Heptane undergoes a liquid-to-solid phase transition at 1.2 GPa and a solid-to-solid phase transition was determined with onset at approximately 1.5 GPa. Evidence for this phase transition is observed in the X-ray diffraction unit cell volume change, and supported by a discontinuous shift in the IR absorbance peaks. This phase transition occurs below the hydrostatic limit of heptane. No evidence of other phase transitions was observed in heptane up to 10 GPa from the XRD or IR data. Once heptane is in its nonhydrostatic regime, claims of phase transitions should be viewed with skepticism, as the stress state in the diamond anvil cell cannot be determined accurately. Compression of gallium oxide single crystal in heptane shows some anomalous behavior including additional spectral peaks, which are attributed to effects of nonhydrostatic compression.

CHAPTER SIX: CONCLUSIONS

This chapter concludes the findings of this work and provides direction for future work on this subject.

6.1 Findings

This work investigated the effect of chromium ion dopants on the optical spectrum of two ultra-wide bandgap semiconductors, gallium oxide (β-$Ga_2O_3:Cr^{3+}$) and aluminum gallium oxide alloy [$(Al_{0.1}Ga_{0.9})_2O_3$ or AGO].

From the results of variable temperature measurements (20-300 K), we determined that the R lines red-shift with increasing temperature, and below 50 K the R_1 line intensity is dominant due to thermal depopulation of the R_2 line. Above 50 K, R_2/R_1 intensity ratio is strongly affected by nonradiative recombination. AGO has smaller thermal activation barriers to nonradiative energy transfer than Ga_2O_3, likely due to the decreased symmetry of the alloy which provides more nonradiative recombination pathways.

Ga_2O_3 and AGO were studied under static high pressure conditions through the use of diamond anvil cells. The R_1-R_2 splitting, which arises due to the crystal field and spin-orbit coupling, is larger in β-Ga_2O_3 than in ruby ($Al_2O_3:Cr^{3+}$) and increases further with applied pressure. The R_1 line in AGO, however, shows a smaller shift versus pressure than Ga_2O_3, which shows that the R_1 line shift is sensitive to alloy composition. X-ray diffraction measurements indicate that the AGO equation of state is similar to that of β-Ga_2O_3. Nonradiative recombination contributes significantly to the pressure-dependent intensity of the R lines in both β-$Ga_2O_3:Cr^{3+}$ and AGO. Nonhydrostatic stress results suggest that the R_1 line of β-$Ga_2O_3:Cr^{3+}$ or AGO could serve as a sensitive indicator of nonhydrostatic stress. Since chromium luminescence is correlated with *n*-type conductivity, these results allow for the use of chromium as a stress gauge and conductivity probe in gallium oxide and AGO devices.

Additionally, the hydrostatic limits of the pressure-transmitting media mineral oil and heptane were determined. Mineral oil behaves nonhydrostatically at pressures above 2.5 GPa and heptane above 3.5 GPa. A new solid-to-solid phase transition was discovered in heptane at approximately 1.5 GPa, evidenced by X-ray diffraction and supported by a discontinuous shift in the IR absorbance peaks.

6.2 Future work

Future work to extend the pressure range should reveal evidence of the $\beta \rightarrow \alpha$ phase transition in β-Ga_2O_3:Cr^{3+}. This transition is computationally predicted to occur at 2.6-9.5 GPa[85,87] and experimentally reported at 6.5-7 GPa[30] or 20-22 GPa[86]. In AGO, the phase transition has been experimentally observed at ~13.5 GPa for 20% Al.[96] No evidence of the phase transition was found in this work in the PL data below 9 GPa or XRD below 6 GPa.

Further work may involve varying the aluminum percentage in AGO to determine if the nonlinearity in R_1 persists for higher concentrations of Al. In the extreme limit of 70+% Al, the alloy is in the corundum phase[96,148] and it would be expected to behave more similarly to ruby. Further study to extend this work to higher pressures may reveal interesting optical spectroscopy data around the $\beta \rightarrow \alpha$ phase transition. This transition is expected to occur at lower pressures for higher concentrations of Al_2O_3.[96]

REFERENCES

1. Vasyltsiv, V. *et al.* Correlation between electrical conductivity and luminescence properties in β-Ga_2O_3:Cr^{3+} and β-Ga_2O_3:Cr,Mg single crystals. *J. Vac. Sci. Technol. Vac. Surf. Films* **39**, 033201 (2021).
2. Jesenovec, J. *et al.* Alternative alloy to increase bandgap in gallium Oxide, β-(ScxGa1-x)2O3, and rare earth Stark luminescence. *J. Cryst. Growth* **596**, 126823 (2022).
3. Asghar, M. S. J. *Power Electronics*. (PHI learning Pvt. Ltd., 2004).
4. Tiku, D. History: DC Power Transmission Mercury-Arc to Thyristor HVdc Valves. *IEEE Power and Energy Magazine* (2014).
5. Morris, P. R. *A History of the World Semiconductor Industry*. (IET, 1990).
6. Yu, P. & Cardona, M. *Fundamentals of Semiconductors: Physics and Material Properties*. (Springer, 1999).
7. McCluskey, M. D. & Haller, E. E. *Dopants and Defects in Semiconductors*. (CRC Press, 2018).
8. Agrawal, G. P. & Dutta, N. K. Recombination Mechanisms in Semiconductors. in *Semiconductor Lasers* (eds. Agrawal, G. P. & Dutta, N. K.) 74–146 (Springer US, 1993). doi:10.1007/978-1-4613-0481-4_3.
9. Ashcroft, N. W. & Mermin, N. D. *Solid State Physics*. (Cengage Learning, 1976).
10. Holt, D. B. & Yacobi, B. G. *Extended defects in semiconductors*. (Cambridge University Press, 2007).
11. Nye, J. F. *Physical Properties of Crystals*. (Oxford University Press, 1957).

12. Hearmon, R. F. S. *An Introduction to Applied Anisotropic Elasticity*. (Clarendon Press: Oxford University Press, 1961).
13. Sanpaz. *Components stress tensor. Creative commons license. https://en.wikipedia.org/wiki/File:Components_stress_tensor_cartesian.svg*.
14. Horn, P. D. & Gupta, Y. M. Luminescence R-line spectrum of ruby crystals shocked to 125 kbar along the crystal c axis. *Phys. Rev. B* **39**, 973–979 (1989).
15. Gupta, Y. M. & Shen, X. A. Potential use of the ruby R_2 line shift for static high-pressure calibration. *Appl. Phys. Lett.* **58**, 583–585 (1991).
16. Adachi, K. *et al.* Unusual elasticity of monoclinic $\beta-Ga_2O_3$. *J. Appl. Phys.* **124**, 085102 (2018).
17. McCluskey, M. D. Point defects in Ga_2O_3. *J. Appl. Phys.* **127**, 101101 (2020).
18. Higashiwaki, M., Sasaki, K., Kuramata, A., Masui, T. & Yamakoshi, S. Gallium oxide (Ga_2O_3) metal-semiconductor field-effect transistors on single-crystal β-Ga_2O_3 (010) substrates. *Appl. Phys. Lett.* **100**, 013504 (2012).
19. Bilbao, A. V. *et al.* Continuous switching of ultra-high voltage silicon carbide MOSFETs. in *2016 IEEE International Power Modulator and High Voltage Conference (IPMHVC)* 463–466 (2016). doi:10.1109/IPMHVC.2016.8012882.
20. Simonaitis, J. W., Slayton, B., Yang-Keathley, Y., Keathley, P. D. & Berggren, K. K. Precise, subnanosecond, and high-voltage switching enabled by gallium nitride electronics integrated into complex loads. *Rev. Sci. Instrum.* **92**, 074704 (2021).
21. Chowdhury, S. Gallium nitride based power switches for next generation of power conversion. *Phys. Status Solidi A* **212**, 1066–1074 (2015).

22. Green, A. J. *et al.* β-Gallium oxide power electronics. *APL Mater.* **10**, 029201 (2022).
23. Chabak, K. D. *et al.* Lateral β-Ga_2O_3 field effect transistors. *Semicond. Sci. Technol.* **35**, 013002 (2019).
24. Wong, M. H. *et al.* Acceptor doping of β-Ga_2O_3 by Mg and N ion implantations. *Appl. Phys. Lett.* **113**, 102103 (2018).
25. Frodason, Y. K., Johansen, K. M., Vines, L. & Varley, J. B. Self-trapped hole and impurity-related broad luminescence in β-Ga_2O_3. *J. Appl. Phys.* **127**, 075701 (2020).
26. Gustafson, T. D. *et al.* Zn acceptors in β-Ga_2O_3 crystals. *J. Appl. Phys.* **129**, 155701 (2021).
27. Ritter, J. R. *et al.* Compensation and hydrogen passivation of magnesium acceptors in β-Ga_2O_3. *Appl. Phys. Lett.* **113**, 052101 (2018).
28. Yoshioka, S. *et al.* Structures and energetics of Ga2O3 polymorphs. *J. Phys. Condens. Matter* **19**, 346211 (2007).
29. Geller, S. Crystal Structure of β-Ga_2O_3. *J. Chem. Phys.* **33**, 676–684 (1960).
30. Lipinska-Kalita, K. E., Kalita, P. E., Hemmers, O. A. & Hartmann, T. Equation of state of gallium oxide to 70 GPa: Comparison of quasihydrostatic and nonhydrostatic compression. *Phys. Rev. B* **77**, 094123 (2008).
31. Momma, K. & Izumi, F. VESTA 3 for three-dimensional visualization of crystal, volumetric and morphology data. *J. Appl. Crystallogr.* **44**, 1272–1276 (2011).
32. Battiston, G. A., Gerbasi, R., Porchia, M., Bertoncello, R. & Caccavale, F. Chemical vapour deposition and characterization of gallium oxide thin films. *Thin Solid Films* **279**, 115–118 (1996).

33. Sasaki, K. *et al.* Device-Quality β-Ga2O3 Epitaxial Films Fabricated by Ozone Molecular Beam Epitaxy. *Appl. Phys. Express* **5**, 035502 (2012).
34. Ghose, S. *et al.* Growth and characterization of β-Ga2O3 thin films by molecular beam epitaxy for deep-UV photodetectors. *J. Appl. Phys.* **122**, 095302 (2017).
35. Takakura, K. *et al.* Evaluation of the crystalline quality of β-Ga2O3 films by optical absorption measurements. *Phys. B Condens. Matter* **404**, 4854–4857 (2009).
36. Tomm, Y., Ko, J. M., Yoshikawa, A. & Fukuda, T. Floating zone growth of β-Ga2O3: a new window material for optoelectronic device applications. *Sol. Energy Mater. Sol. Cells* **66**, 369–374 (2001).
37. Kuramata, A. *et al.* High-quality β-Ga2O3 single crystals grown by edge-defined film-fed growth. *Jpn. J. Appl. Phys.* **55**, 1202A2 (2016).
38. McCloy, J. S. *et al.* Growth and defect characterization of doped and undoped β-Ga2O3 crystals. in *Oxide-based Materials and Devices XIII* vol. 12002 21–39 (SPIE, 2022).
39. Irmscher, K., Galazka, Z., Pietsch, M., Uecker, R. & Fornari, R. Electrical properties of β-Ga2O3 single crystals grown by the Czochralski method. *J. Appl. Phys.* **110**, 063720 (2011).
40. Galazka, Z. Growth of bulk β-Ga2O3 single crystals by the Czochralski method. *J. Appl. Phys.* **131**, 031103 (2022).
41. Jesenovec, J. *et al.* Alloyed β-$(Al_xGa_{1-x})_2O_3$ bulk Czochralski single β-$(Al_{0.1}Ga_{0.9})_2O_3$ and polycrystals β-$(Al_{0.33}Ga_{0.66})_2O_3$, β-$(Al_{0.5}Ga_{0.5})_2O_3$), and property trends. *J. Appl. Phys.* **131**, 155702 (2022).

42. Remple, C., Barmore, L. M., Jesenovec, J., McCloy, J. S. & McCluskey, M. D. Photoluminescence spectroscopy of Cr3+ in β-Ga2O3 and (Al0.1Ga0.9)2O3. *J. Vac. Sci. Technol. A* **41**, 022702 (2023).

43. Onuma, T. *et al.* Correlation between blue luminescence intensity and resistivity in β-Ga2O3 single crystals. *Appl. Phys. Lett.* **103**, 041910 (2013).

44. Sun, R., Ooi, Y. K., Dickens, P. T., Lynn, K. G. & Scarpulla, M. A. On the origin of red luminescence from iron-doped β-Ga_2O_3 bulk crystals. *Appl. Phys. Lett.* **117**, 052101 (2020).

45. Peelaers, H. & Van de Walle, C. G. Brillouin zone and band structure of β-Ga2O3. *Phys. Status Solidi B* **252**, 828–832 (2015).

46. Peelaers, H., Lyons, J. L., Varley, J. B. & Van de Walle, C. G. Deep acceptors and their diffusion in Ga2O3. *APL Mater.* **7**, 022519 (2019).

47. Mohamed, M. *et al.* The electronic structure of β-Ga2O3. *Appl. Phys. Lett.* **97**, 211903 (2010).

48. Saleh, M. *et al.* Electrical and optical properties of Zr doped β-Ga2O3 single crystals. *Appl. Phys. Express* **12**, 085502 (2019).

49. Saleh, M. *et al.* Degenerate doping in β-Ga2O3 single crystals through Hf-doping. *Semicond. Sci. Technol.* **35**, 04LT01 (2020).

50. Kananen, B. E., Halliburton, L. E., Stevens, K. T., Foundos, G. K. & Giles, N. C. Gallium vacancies in β-Ga_2O_3 crystals. *Appl. Phys. Lett.* **110**, 202104 (2017).

51. Luchechko, A. *et al.* Luminescence spectroscopy of Cr^{3+} ions in bulk single crystalline β-Ga_2O_3. *J. Phys. Appl. Phys.* **53**, 354001 (2020).

52. Vivien, D. *et al.* Optical properties of β-Ga_2O_3:Cr^{3+} single crystals for tunable laser applications. *J. Lumin.* **39**, 29–33 (1987).
53. Tippins, H. H. Optical and Microwave Properties of Trivalent Chromium in β-Ga_2O_3. *Phys. Rev.* **137**, A865–A871 (1965).
54. Tanabe, Y. & Sugano, S. On the Absorption Spectra of Complex Ions. I. *J. Phys. Soc. Jpn.* **9**, 753–766 (1954).
55. Tippins, H. H. Optical and Microwave Properties of Trivalent Chromium in β-Ga_2O_3. *Phys. Rev.* **137**, A865–A871 (1965).
56. Tokida, Y. & Adachi, S. Photoluminescence spectroscopy and energy-level analysis of metal-organic-deposited Ga_2O_3:Cr^{3+} films. *J. Appl. Phys.* **112**, 063522 (2012).
57. Wakai, H., Sinya, Y. & Yamanaka, A. Effect of Cr3+ ions on optical properties in β-Ga2O3 semiconductor. *Phys. Status Solidi C* **8**, 537–539 (2011).
58. Schawlow, A. L. Fine-Line Spectra of Chromium Ions in Crystals. *J. Appl. Phys.* **33**, 395–398 (1962).
59. Stehr, J. E. *et al.* Magneto-optical properties of Cr^{3+} in β-Ga_2O_3. *Appl. Phys. Lett.* **119**, 052101 (2021).
60. Walsh, C. G. *et al.* Luminescence from β-Ga_2O_3: Cr^{3+}. *J. Lumin.* **40–41**, 103–104 (1988).
61. Sugano, S. & Tanabe, Y. Absorption Spectra of Cr^{3+} in Al_2O_3. *J. Phys. Soc. Jpn.* **13**, 880–899 (1958).
62. Vivien, D. *et al.* Optical properties of β-Ga2O3:Cr3+ single crystals for tunable laser applications. *J. Lumin.* **39**, 29–33 (1987).

63. Seat, H. C. & Sharp, J. H. Dedicated Temperature Sensing With C-Axis Oriented Single-Crystal Ruby ($Cr^{3+}:Al_2O_3$) Fibers: Temperature and Strain Dependences of R-Line Fluorescence. *IEEE Trans. Instrum. Meas.* **53**, 15 (2004).

64. Sun, R., Ooi, Y. K., Dickens, P. T., Lynn, K. G. & Scarpulla, M. A. On the origin of red luminescence from iron-doped β-Ga_2O_3 bulk crystals. *Appl. Phys. Lett.* **117**, 052101 (2020).

65. Mariotto, G., Montagna, M. & Rossi, F. THERMAL SHIFT AND BROADENING OF THE ^2E-$^4A_2$ ZERO-PHONON LINES IN β-ALUMINA:CR^{3+} CRYSTALS. *J. Phys. Colloq.* **46**, C7-343-C7-347 (1985).

66. Luhs, W. & Wellegehausen, B. Diode pumped cw ruby laser. *OSA Contin.* **2**, 184–191 (2019).

67. Fang, Y. *et al.* Investigation of temperature-dependent photoluminescence in multi-quantum wells. *Sci. Rep.* **5**, 12718 (2015).

68. Lu, T. *et al.* Temperature-dependent photoluminescence in light-emitting diodes. *Sci. Rep.* **4**, 6131 (2015).

69. Beales, T. P., Goodman, C. H. L. & Scarrott, K. A new high pressure calibrant: β-Ga2O3:Cr. *Solid State Commun.* **73**, 1–3 (1990).

70. Misu, A. Emissions of Ruby. *J. Phys. Soc. Jpn.* **19**, 2260–2270 (1964).

71. Weinstein, B. A. Ruby thermometer for cryobaric diamond-anvil cell. *Rev. Sci. Instrum.* **57**, 910–913 (1986).

72. McCumber, D. E. & Sturge, M. D. Linewidth and Temperature Shift of the *R* Lines in Ruby. *J. Appl. Phys.* **34**, 1682–1684 (1963).

73. Ragan, D. D., Gustavsen, R. & Schiferl, D. Calibration of the ruby R_1 and R_2 fluorescence shifts as a function of temperature from 0 to 600 K. *J. Appl. Phys.* **72**, 5539–5544 (1992).

74. Yen, J. & Nicol, M. Temperature dependence of the ruby luminescence method for measuring high pressures. *J. Appl. Phys.* **72**, 5535–5538 (1992).

75. Gibson, U. & Chernuschenko, M. Ruby Films as Surface Temperature and Pressure Sensors. *Opt. Express* **4**, 443 (1999).

76. Yamaoka, H. *et al.* Ruby pressure scale in a low-temperature diamond anvil cell. *J. Appl. Phys.* **112**, 124503 (2012).

77. Gao, R., Li, H. & Zhao, J. Dependence of R fluorescence lines of rubies on Cr^{3+} concentration at various temperatures, with implications for pressure calibrations in experimental apparatus. *Am. Mineral.* **100**, 1554–1561 (2015).

78. Cook, R. F. & Michaels, C. A. Review: Coefficients for Stress, Temperature, and Composition Effects in Fluorescence Measurements of Alumina. *J. Res. Natl. Inst. Stand. Technol.* **122**, 43 (2017).

79. Piermarini, G. J., Block, S., Barnett, J. D. & Forman, R. A. Calibration of the pressure dependence of the R_1 ruby fluorescence line to 195 kbar. *J. Appl. Phys.* **46**, 2774–2780 (1975).

80. Mao, H. K., Xu, J. & Bell, P. M. Calibration of the ruby pressure gauge to 800 kbar under quasi-hydrostatic conditions. *J. Geophys. Res. Solid Earth* **91**, 4673–4676 (1986).

81. Shen, G. *et al.* Toward an international practical pressure scale: A proposal for an IPPS ruby gauge (IPPS-Ruby2020). *High Press. Res.* **40**, 299–314 (2020).

82. Eggert, J. H., Goettel, K. A. & Silvera, I. F. Ruby at high pressure. I. Optical line shifts to 156 GPa. *Phys. Rev. B* **40**, 5724–5732 (1989).

83. Zhydachevskyy, Y. *et al.* Chemical Tuning, Pressure, and Temperature Behavior of Mn^{4+} Photoluminescence in Ga_2O_3–Al_2O_3 Alloys. *Inorg. Chem.* **61**, 18135–18146 (2022).

84. Kim, B. G. Epitaxial strain effect on the band gap of a Ga2O3 wide bandgap material. *J. Korean Phys. Soc.* (2021) doi:10.1007/s40042-021-00304-x.

85. He, H. *et al.* First-principles study of the structural, electronic, and optical properties of Ga_2O_3 in its monoclinic and hexagonal phases. *Phys. Rev. B* **74**, 195123 (2006).

86. Machon, D., McMillan, P. F., Xu, B. & Dong, J. High-pressure study of the β-to-α transition in Ga_2O_3. *Phys. Rev. B* **73**, 094125 (2006).

87. Kroll, P. Spinel-type gallium oxynitrides attainable at high pressure and high temperature. *Phys. Rev. B* **72**, 144407 (2005).

88. Yan-Mei, M. *et al.* High-Pressure and High-Temperature Behaviour of Gallium Oxide. *Chin. Phys. Lett.* **25**, 1603–1605 (2008).

89. Tu, B. *et al.* The pressure-induced phase transition of Ga2O3. *J. Phys. Condens. Matter* **14**, 10627–10630 (2002).

90. Varley, J. B. First-principles calculations of structural, electrical, and optical properties of ultra-wide bandgap $(Al_xGa_{1-x})_2O_3$ alloys. *J. Mater. Res.* (2021) doi:10.1557/s43578-021-00371-7.

91. Bhattacharjee, J., Gupta, R. K. & Singh, S. D. Assessment of bonding characteristic of β-(AlxGa1−x)2O3 alloys from photoluminescence and x-ray absorption near edge spectroscopy. *Appl. Phys. Lett.* **122**, 152104 (2023).

92. Peelaers, H., Varley, J. B., Speck, J. S. & Van de Walle, C. G. Structural and electronic properties of Ga_2O_3-Al_2O_3 alloys. *Appl. Phys. Lett.* **112**, 242101 (2018).

93. Jesenovec, J. *et al.* Alloyed β-$(Al_xGa_{1-x})_2O_3$ bulk Czochralski single β-$(Al_{0.1}Ga_{0.9})_2O_3$ and polycrystals β-$(Al_{0.33}Ga_{0.66})_2O_3$, β-$(Al_{0.5}Ga_{0.5})_2O_3$), and property trends. *J. Appl. Phys.* **131**, 155702 (2022).

94. Cook, D. S. *et al.* Synthesis and Polymorphism of Mixed Aluminum–Gallium Oxides. *Inorg. Chem.* **59**, 3805–3816 (2020).

95. Cooke, J. *et al.* Effect of extended defects on photoluminescence of gallium oxide and aluminum gallium oxide epitaxial films. *Sci. Rep.* **12**, 3243 (2022).

96. Chen, K.-C. *et al.* Chemical and Mechanical Pressure-Induced Photoluminescence Tuning via Structural Evolution and Hydrostatic Pressure. *Chem. Mater.* **33**, 3832–3840 (2021).

97. Shannon, R. D. Revised effective ionic radii and systematic studies of interatomic distances in halides and chalcogenides. *Acta Crystallogr. A* **32**, 751–767 (1976).

98. Gilliland, G. D. Photoluminescence spectroscopy of crystalline semiconductors. *Mater. Sci. Eng. R Rep.* **18**, 99–399 (1997).

99. Perkowitz, S. *Optical Characterization of Semiconductors: Infrared, Raman, and Photoluminescence Spectroscopy*. (Elsevier, 2012).

100. Dunstan, D. J. & Spain, I. L. Technology of diamond anvil high-pressure cells: I. Principles, design and construction. *J. Phys. [E]* **22**, 913–923 (1989).

101. *Diamond anvil cell cross section. Creative Commons license. https://commons.wikimedia.org/wiki/File:Diamond_Anvil_Cell_-_Cross_Section.svg.*

102. Block, S. & Piermarini, G. The diamond cell stimulates high-pressure research. *Phys. Today* **29**, 44–55 (1976).

103. Jayaraman, A. Diamond anvil cell and high-pressure physical investigations. *Rev. Mod. Phys.* **55**, 65–108 (1983).

104. Silvera, I. F. & Wijngaarden, R. J. Diamond anvil cell and cryostat for low-temperature optical studies. *Rev. Sci. Instrum.* **56**, 121–124 (1985).

105. Dubrovinskaia, N. & Dubrovinsky, L. Whole-cell heater for the diamond anvil cell. *Rev. Sci. Instrum.* **74**, 3433–3437 (2003).

106. Gao, C. *et al.* Accurate measurements of high pressure resistivity in a diamond anvil cell. *Rev. Sci. Instrum.* **76**, 083912 (2005).

107. Matsumoto, R. *et al.* Diamond anvil cells using boron-doped diamond electrodes covered with undoped diamond insulating layer. *Appl. Phys. Express* **11**, 053101 (2018).

108. Chai, M. & Brown, J. M. Effects of static non-hydrostatic stress on the R lines of ruby single crystals. *Geophys. Res. Lett.* **23**, 3539–3542 (1996).

109. Dreger, Z. A. *et al.* Optical response of molecular crystals to non-hydrostatic compression in diamond anvil cell experiments. in 1233–1238 (2008). doi:10.1063/1.2832942.

110. Klotz, S., Chervin, J.-C., Munsch, P. & Marchand, G. L. Hydrostatic limits of 11 pressure transmitting media. *J. Phys. Appl. Phys.* **42**, 075413 (2009).

111. Ma, C. *et al.* Rotator Phases of *n* -Heptane under High Pressure: Raman Scattering and X-ray Diffraction Studies. *J. Phys. Chem. C* **115**, 18310–18315 (2011).

112. Willmott, P. *An Introduction to Synchrotron Radiation: Techniques and Applications*. (John Wiley & Sons, 2019).

113. Ternov, I. M. Synchrotron radiation. *Phys.-Uspekhi* **38**, 409 (1995).

114. *Hydrargyrum (https://commons.wikimedia.org/wiki/File:Bragg_diffraction_2.svg), „Bragg diffraction 2“, https://creativecommons.org/licenses/by-sa/3.0/legalcode*.

115. Kunz, M. *et al.* A beamline for high-pressure studies at the Advanced Light Source with a superconducting bending magnet as the source. *J. Synchrotron Radiat.* **12**, 650–658 (2005).

116. Prescher, C. & Prakapenka, V. B. DIOPTAS: a program for reduction of two-dimensional X-ray diffraction data and data exploration. *High Press. Res.* **35**, 223–230 (2015).

117. Le Bail, A., Duroy, H. & Fourquet, J. L. Ab-initio structure determination of LiSbWO6 by X-ray powder diffraction. *Mater. Res. Bull.* **23**, 447–452 (1988).

118. Rietveld, H. M. A profile refinement method for nuclear and magnetic structures. *J. Appl. Crystallogr.* **2**, 65–71 (1969).

119. Bail, A. L. Whole powder pattern decomposition methods and applications: A retrospection. *Powder Diffr.* **20**, 316–326 (2005).

120. Toby, B. H. & Von Dreele, R. B. GSAS-II: the genesis of a modern open-source all purpose crystallography software package. *J. Appl. Crystallogr.* **46**, 544–549 (2013).

121. Moré, J. J. The Levenberg-Marquardt algorithm: Implementation and theory. in *Numerical Analysis* (ed. Watson, G. A.) 105–116 (Springer, 1978). doi:10.1007/BFb0067700.

122. Tokida, Y. & Adachi, S. Photoluminescence spectroscopy and energy-level analysis of metal-organic-deposited Ga_2O_3:Cr^{3+} films. *J. Appl. Phys.* **112**, 063522 (2012).

123. Vivien, D. *et al.* Optical properties of β-Ga2O3:Cr3+ single crystals for tunable laser applications. *J. Lumin.* **39**, 29–33 (1987).

124. Shockley, W. & Read, W. T. Statistics of the Recombinations of Holes and Electrons. *Phys. Rev.* **87**, 835–842 (1952).

125. Barmore, L. M., Jesenovec, J., McCloy, J. S. & McCluskey, M. D. Photoluminescence of Cr3+ in β-Ga2O3 and (Al0.1Ga0.9)2O3 under pressure. *J. Appl. Phys.* **133**, 175703 (2023).

126. Luchechko, A. *et al.* Luminescence spectroscopy of Cr^{3+} ions in bulk single crystalline β-Ga_2O_3. *J. Phys. Appl. Phys.* **53**, 354001 (2020).

127. Remple, C., Huso, J. & McCluskey, M. D. Photoluminescence and Raman mapping of β-Ga_2O_3. *AIP Adv.* **11**, 105006 (2021).

128. Murnaghan, F. D. Finite Deformations of an Elastic Solid. *Am. J. Math.* **59**, 235–260 (1937).

129. Birch, F. Finite Elastic Strain of Cubic Crystals. *Phys. Rev.* **71**, 809–824 (1947).

130. Birch, F. Finite strain isotherm and velocities for single-crystal and polycrystalline NaCl at high pressures and 300°K. *J. Geophys. Res. Solid Earth* **83**, 1257–1268 (1978).

131. Westerfield, C. & Agnew, S. IR study of the chemistry of boundary lubrication with high temperature and high pressure shear. *Wear* **181–183**, 805–809 (1995).

132. Bertani, R., Mali, M., Roos, J. & Brinkmann, D. A diamond anvil cell for high-pressure NMR investigations. *Rev. Sci. Instrum.* **63**, 3303–3306 (1992).

133. Zha, C.-S. & Boehler, R. Melting of sodium and potassium in a diamond anvil cell. *Phys. Rev. B* **31**, 3199–3201 (1985).

134. Serra-Crespo, P. *et al.* Experimental evidence of negative linear compressibility in the MIL-53 metal–organic framework family. *CrystEngComm* **17**, 276–280 (2015).

135. Demirbas, A., Balubaid, M. A., Basahel, A. M., Ahmad, W. & Sheikh, M. H. Octane Rating of Gasoline and Octane Booster Additives. *Pet. Sci. Technol.* **33**, 1190–1197 (2015).
136. Uyumaz, A. An experimental investigation into combustion and performance characteristics of an HCCI gasoline engine fueled with n-heptane, isopropanol and n-butanol fuel blends at different inlet air temperatures. *Energy Convers. Manag.* **98**, 199–207 (2015).
137. Conkerton, E. J., Wan, P. J. & Richard, O. A. Hexane and heptane as extraction solvents for cottonseed: A laboratory-scale study. *J. Am. Oil Chem. Soc.* **72**, 963–965 (1995).
138. Drueckhammer, D. G., Gao, S. Q., Liang, X. & Liao, J. Acetone–Heptane as a Solvent System for Combining Chromatography on Silica Gel with Solvent Recycling. *ACS Sustain. Chem. Eng.* **1**, 87–90 (2013).
139. Muringer, M. J. P., Trappeniers, N. J. & Biswas, S. N. The Effect of Pressure on the Sound Velocity and Density of Toluene and n-heptane up to 2600 bar. *Phys. Chem. Liq.* **14**, 273–296 (1985).
140. Yakushi, K., Lauchlan, L. J., Clarke, T. C. & Street, G. B. Optical study of polypyrrole perchlorate. *J. Chem. Phys.* **79**, 4774–4778 (1983).
141. Offen, H. W., Tanquary, R. L. & Sterrett, K. F. High-Pressure Apparatus for Optical Studies at 77°K. *J. Appl. Phys.* **38**, 5245–5248 (1967).
142. Qiao, E., Zheng, H. & Long, C. In Situ High-Pressure and High-Temperature Experiments on n-Heptane. *Appl. Spectrosc.* **66**, 233–236 (2012).
143. Rasmussen, A. Pressure-induced phase transitions of indium selenide. (Washington State University, 2016).

144. Yamaguchi, M., Serafin, S. V., Morton, T. H. & Chronister, E. L. Infrared Absorption Studies of n-Heptane under High Pressure. *J. Phys. Chem. B* **107**, 2815–2821 (2003).

145. Kavitha, G. & Narayana, C. Raman Scattering Studies on n-Heptane under High Pressure. *J. Phys. Chem. B* **110**, 8777–8781 (2006).

146. Krishnan, M. & Balasubramanian, S. n-Heptane under Pressure: Structure and Dynamics from Molecular Simulations. *J. Phys. Chem. B* **109**, 1936–1946 (2005).

147. Merle, A. M. *et al.* Study of the multiplet nature in shpol'skii effect: Host n-heptane crystalline structure by X-ray diffraction and guest coronene position by ESR. *Chem. Phys.* **22**, 207–214 (1977).

148. Varley, J. B. First-principles calculations of structural, electrical, and optical properties of ultra-wide bandgap $(Al_xGa_{\{1-x\}})_2O_3$ alloys. *J. Mater. Res.* **36**, 4790–4803 (2021).

149. Townsend, J. S. *A modern approach to quantum mechanics*. (University Science Books, 2000).

150. Blanco, M. A., Flórez, M. & Bermejo, M. Evaluation of the rotation matrices in the basis of real spherical harmonics. *J. Mol. Struct. THEOCHEM* **419**, 19–27 (1997).

151. Belford, R. *The shapes of atomic orbitals. (CC BY-NC-SA 4.0).*

APPENDICIES

APPENDIX A: D ORBITAL PERTURBATION THEORY

A.1 d orbital perturbation theory

This section provides an approximation of the effect on the d orbitals of the chromium (Cr^{3+}) atoms in octahedral coordination caused by the neighboring six oxygen atoms using perturbation theory. This appendix draws on earlier works by Sugano and Tanabe[61] and Sun et al[44] regarding the electronic states of octahedrally coordinated Cr^{3+}. For simplification, the following approximations will be made:

1. The O atoms are point masses modeled by Dirac delta functions (ignore spin),
2. The atoms are located exactly on the axes (Figure A.1), (symmetry group O_h),
3. The atoms are all distance *d* from the origin, where the substitutional Cr^{3+} atom is located.

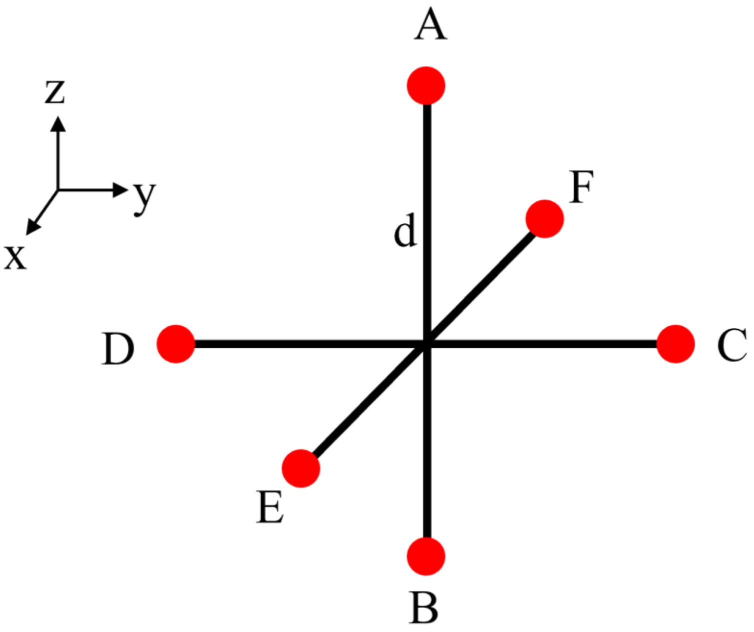

Figure A.1: Model of the atomic positions.

The delta functions have strength given by a constant (*A*, *B*, *C*, *D*, *E*, *F*). As we know from basic quantum mechanics, the wavefunction of the hydrogen atom is

$$\psi_{nlm} = R_{nl}Y_{lm}$$

where *n*,*l*,*m* are the principal quantum numbers, *R* is the radial part of the wavefunction, and *Y* are the spherical harmonics. The d orbitals are defined as the wavefunctions where *l* = 2. There are five d orbitals for *m* = -2, -1, 0, 1, 2, since $-m \leq l \leq m$.

First we will calculate the radial part of the 3d wavefunction. The radial part of the d orbital wavefunction is R_{32}, since $n = 3$ and *l* = 2. R_{32} is given by[149]

$$R_{32} = \frac{2\sqrt{2}}{27\sqrt{5}}\left(\frac{Z}{3a_0}\right)^{3/2}\left(\frac{Zr}{a_0}\right)^2 e^{-Zr/3a_0}$$

where a_0 is the Bohr radius ($a_0 = \frac{\hbar}{\alpha mc}$) and Z is the atomic number. Let $K = \frac{2\sqrt{2}}{27\sqrt{5}}\left(\frac{Z}{3a_0}\right)^{3/2}\left(\frac{Z}{a_0}\right)^2$, so that $R_{32} = Kr^2e^{-Zr/3a_0}$. Then, squaring R_{32}, we have

$$R_{32}^2 = K^2r^4e^{-2Zr/3a_0}$$

This radial part will be the same for all wavefunctions, so it will be referred to as simply R_{32}^2.

In Cartesian coordinates, there are five orthonormal spherical harmonics for the d orbitals:[150]

$$Y_{xy} = \frac{1}{2}\sqrt{\frac{15}{\pi}}\frac{xy}{r^2}$$

$$Y_{yz} = \frac{1}{2}\sqrt{\frac{15}{\pi}}\frac{yz}{r^2}$$

$$Y_{z^2} = \frac{1}{4}\sqrt{\frac{5}{\pi}}\frac{3z^2 - r^2}{r^2}$$

$$Y_{xz} = \frac{1}{2}\sqrt{\frac{15}{\pi}}\frac{xz}{r^2}$$

$$Y_{x^2-y^2} = \frac{1}{4}\sqrt{\frac{15}{\pi}}\frac{x^2 - y^2}{r^2}$$

where $r^2 = x^2 + y^2 + z^2$.

To find the probability density, that is, the likelihood of finding an electron at a specific position, we can take the complex conjugate of the wavefunction. Since our wavefunction is real, we can simply square the radial and spherical harmonic parts separately and then multiply them together:

$$|\psi|^2 = R_{32}^2 Y^2$$

Thus, the five d orbital probability densities become:

$$\left|\psi_{xy}\right|^2 = R_{32}^2 \frac{15}{4\pi} \frac{x^2 y^2}{r^4}$$

$$\left|\psi_{yz}\right|^2 = R_{32}^2 \frac{15}{4\pi} \frac{y^2 z^2}{r^4}$$

$$|\psi_{z^2}|^2 = R_{32}^2 \frac{5}{16\pi} \frac{(9z^4 - 6z^2 r^2 + r^4)}{r^4}$$

$$|\psi_{xz}|^2 = R_{32}^2 \frac{15}{4\pi} \frac{x^2 z^2}{r^4}$$

$$\left|\psi_{x^2-y^2}\right|^2 = R_{32}^2 \frac{15}{16\pi} \frac{(x^4 - 2x^2 y^2 + y^4)}{r^4}$$

Now that the five d orbitals have been determined, we can include the delta function perturbations. Each term will follow the form

$$\int |\psi|^2 A \delta(\vec{r} - \overrightarrow{r_0})\, dv = |\psi(\overrightarrow{r_0})|^2 A$$

where *A* is the strength of the delta function. The delta function essentially picks the value of the electron probability $|\psi|^2$ at the position $\vec{r} = \overrightarrow{r_0}$. Then we can determine the probability density from the sum of the six perturbing atoms. Take

$$P = |\psi(\overrightarrow{r_A})|^2 A + |\psi(\overrightarrow{r_B})|^2 B + |\psi(\overrightarrow{r_C})|^2 C + |\psi(\overrightarrow{r_D})|^2 D + |\psi(\overrightarrow{r_E})|^2 E + |\psi(\overrightarrow{r_F})|^2 F$$

where $\overrightarrow{r_A}$ is the position of atom A, which is (0, 0, d) in this case. The positions of all six perturbing atoms are listed in Table A.1. We will have five of these probability density expressions for the five d orbitals. Three of these wavefunctions (ψ_{xy}, ψ_{yz}, and ψ_{xz}) will go to zero whenever any two of the coordinates are zero, as they are in this case. We can see in Figure A.2 that for these three orbitals, no part lies on the axes, therefore a perturbing atom on the axes will not have any effect. Two wavefunctions are nonzero; these are ψ_{z^2} and $\psi_{x^2-y^2}$.

	A	B	C	D	E	F
position	(0, 0, d)	(0, 0, -d)	(0, d, 0)	(0, -d, 0)	(d, 0, 0)	(-d, 0, 0)

Table A.1:Cartesian coordinate positions of all six perturbing atoms.

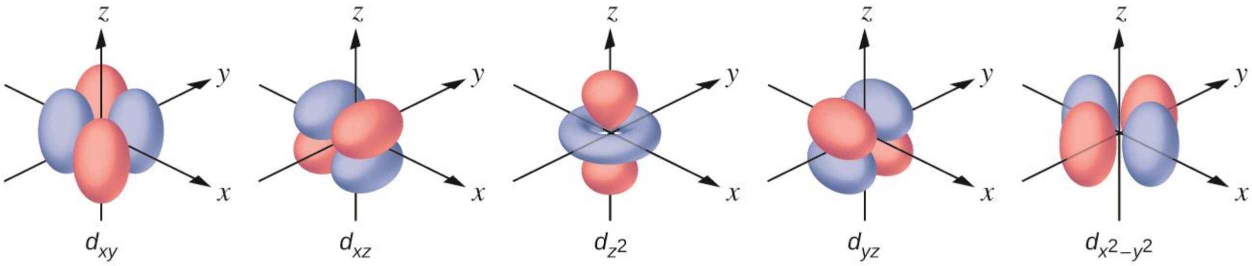

Figure A.2: The shapes of d orbitals defined in the Cartesian coordinate system.[151]

We can determine the probability density for the two nonzero wavefunctions. With $r^4 =$ $= (x^2 + y^2 + z^2)^2 = \mathrm{x}^4 + 2\,\mathrm{x}^2\,\mathrm{y}^2 + 2\,\mathrm{x}^2\,\mathrm{z}^2 + \mathrm{y}^4 + 2\,\mathrm{y}^2\,\mathrm{z}^2 + \mathrm{z}^4$, we have

$$P_{z^2} = R_{32}^2 \frac{5}{16\pi} \frac{[9\mathrm{z}^4 - 6z^2(x^2 + y^2 + z^2) + \mathrm{x}^4 + 2\,\mathrm{x}^2\,\mathrm{y}^2 + 2\,\mathrm{x}^2\,\mathrm{z}^2 + \mathrm{y}^4 + 2\,\mathrm{y}^2\,\mathrm{z}^2 + \mathrm{z}^4]}{\mathrm{x}^4 + 2\,\mathrm{x}^2\,\mathrm{y}^2 + 2\,\mathrm{x}^2\,\mathrm{z}^2 + \mathrm{y}^4 + 2\,\mathrm{y}^2\,\mathrm{z}^2 + \mathrm{z}^4}$$

Plugging in the six particle positions and simplifying, we find:

$$P_{z^2} = R_{32}^2 \frac{5}{16\pi}\left[A\left(\frac{9d^4 - 6d^4 + d^4}{d^4}\right) + B\left(\frac{9d^4 - 6d^4 + d^4}{d^4}\right) + C\left(\frac{d^4}{d^4}\right) + \ D\left(\frac{d^4}{d^4}\right) + E\left(\frac{d^4}{d^4}\right) + F\left(\frac{d^4}{d^4}\right)\right]$$

$$P_{z^2} = R_{32}^2 \frac{5}{16\pi}[4A + 4B + C + \ D + E + F]$$

Repeating this process for $\left|\psi_{x^2-y^2}\right|^2$, we have

$$P_{x^2-y^2} = R_{32}^2 \frac{15}{16\pi} \frac{(x^4 - 2x^2y^2 + y^4)}{(\mathrm{x}^4 \ + \ 2\,\mathrm{x}^2\,\mathrm{y}^2 \ + \ 2\,\mathrm{x}^2\,\mathrm{z}^2 \ + \ \mathrm{y}^4 \ + \ 2\,\mathrm{y}^2\,\mathrm{z}^2 \ + \ \mathrm{z}^4)}$$

$$P_{x^2-y^2} = R_{32}^2 \frac{15}{16\pi}\left[A\left(\frac{0}{d^4}\right) + B\left(\frac{0}{d^4}\right) + C\left(\frac{d^4}{d^4}\right) + \ D\left(\frac{d^4}{d^4}\right) + E\left(\frac{d^4}{d^4}\right) + F\left(\frac{d^4}{d^4}\right)\right]$$

$$P_{x^2-y^2} = R_{32}^2 \frac{15}{16\pi}[C + \ D + E + F]$$

Thus, the two non-zero perturbations are

$$P_{z^2} = R_{32}^2 \frac{5}{16\pi}[4A + 4B + C + \ D + E + F]$$

$$P_{x^2-y^2} = R_{32}^2 \frac{15}{16\pi}[C + \ D + E + F]$$

If we assume all the delta functions have the same strength (that is, *A*=*B*=*C*=*D*=*E*=*F*), then the perturbations become:

$$P_{z^2} = R_{32}^2 \frac{5}{16\pi}[12A] = R_{32}^2 \frac{15A}{4\pi}$$

$$P_{x^2-y^2} = R_{32}^2 \frac{15}{16\pi}[4A] = R_{32}^2 \frac{15A}{4\pi}$$

which are equal to each other.

A.2 Discussion

The d orbital energy levels can be used to predict electronic structures and crystal field effects, which give rise to some of the properties of crystals. In both ruby (Al_2O_3:Cr^{3+}) and chromium-doped gallium oxide (Ga_2O_3:Cr^{3+}), the chromium impurity resides in an octahedral environment surrounded by six oxygen ions. The Cr-O bonds are chemically the same in both crystals, but the bond lengths differ because of the different composition and structure of the host lattice. These bond lengths affect the d orbital interactions and change which affect the absorption bands, resulting in different colors of the crystal. The ground state in the octahedral field with cubic O_h symmetry is $^4A_2$, which corresponds two the three degenerate lower energy levels *xy, yz, xz,* which are equal to 0 in this case. The higher energy level is ^2E, which corresponds to the x^2-y^2 and z^2 energy levels, which are degenerate in the cubic symmetry case that all perturbing atoms are identical. If the cubic symmetry is broken by non-identical perturbing atoms, the x^2-y^2 and z^2 energy levels are no longer degenerate. The degeneracy may also be lifted by accounting for spin and introducing spin-orbit coupling, which would split the ^2E energy level and lead to the *R* line fluorescence.[82]

These wavefunctions depend on the distance of the perturbing atoms from the origin *d*. When this crystal is under pressure, the distance *d* will decrease. Since the probability densities are proportional to d^4e^{-d} in the radial part of the wavefunction, as *d* decreases, the probability density increases. Therefore we can expect the surrounding atoms to more strongly influence the d orbital as pressure is applied. This may help explain the observed phenomena of the *R* line splitting increasing strongly with increasing pressure in Ga_2O_3 and AGO.

APPENDIX B: MINERAL OIL SPECIFICATIONS

We performed experiments to establish the hydrostatic limit of mineral oil. The specifications for the mineral oil (purchased from Sigma-Aldrich) are:

- Product Name: Mineral Oil for IR Spectroscopy
- Product Number: 161403
- CAS Number: 8042-47-5
- Appearance (Color): Colorless
- Appearance (Form): Viscous Liquid
- Specific Gravity 0.818- 0.880 at 25ºC
- Viscosity, Kinematictic @ 40ºC, Centistokes: 15.6- 18.8
- Viscosity, Saybolt @ 100ºF, SUS: 85.0- 100.0
- Specification Date : 11/17/2010

APPENDIX C: CODE

This appendix contains the code used in this work for nonlinear fitting. This includes equation of state fits and temperature- and pressure-dependent intensity ratio fitting. All code is written in Python using Jupyter Notebook as an interactive computing platform.

C.1 Equation of state fit

```
#Birch-Murnaghan equation of state fit to volume and pressure
import matplotlib.pyplot as plt
import numpy as np
from scipy.optimize import curve_fit


#import data
AGOPath = r"C:\filepath\AGO_DACD.csv"
A_nparray=np.loadtxt(AGOPath, delimiter=',', skiprows=1)
AGO_pressures=A_nparray[:,0] #Pressures of AGO DAC D
AGO_vols=A_nparray[:,1] #unit cell volumes of AGO DAC D

AGO2Path = r"C:\filepath\AGO_DACA.csv"
A2_nparray=np.loadtxt(AGO2Path, delimiter=',', skiprows=1)
AGO2_pressures=A2_nparray[:,0] #Pressures of AGO DAC A
AGO2_vols=A2_nparray[:,1] #unit cell volumes of AGO DAC A

#combine DAC D and DAC A for ALL AGO data
all_press = np.append(AGO_pressures, AGO2_pressures)
all_vols = np.append(AGO_vols, AGO2_vols)


#import increasing and decreasing data to distinguish when plotting
AGOincPath = r"C:\filepath\AGO_DACD_inc.csv"
Ainc_nparray=np.loadtxt(AGOincPath, delimiter=',', skiprows=1)
AGOinc_pressures=Ainc_nparray[:,0] #Pressures of AGO DAC D increasing pressure
AGOinc_vols=Ainc_nparray[:,1] #unit cell volumes of AGO DAC D

AGOdecPath = r"C:\filepath\AGO_DACD_dec.csv"
Adec_nparray=np.loadtxt(AGOdecPath, delimiter=',', skiprows=1)
AGOdec_pressures=Adec_nparray[:,0] #Pressures of AGO DAC D decreasing pressure
AGOdec_vols=Adec_nparray[:,1] #unit cell volumes of AGO DAC D
```

```
AAGOincPath = r"C:\filepath\AGO_DACA_inc.csv"
AAinc_nparray=np.loadtxt(AAGOincPath, delimiter=',', skiprows=1)
AAGOinc_pressures=AAinc_nparray[:,0] #Pressures of AGO DAC A increasing pressure
AAGOinc_vols=AAinc_nparray[:,1] #unit cell volumes of AGO DAC A

AAGOdecPath = r"C:\filepath\AGO_DACA_dec.csv"
AAdec_nparray=np.loadtxt(AAGOdecPath, delimiter=',', skiprows=1)
AAGOdec_pressures=AAdec_nparray[:,0] #Pressures of AGO DAC A decreasing pressure
AAGOdec_vols=AAdec_nparray[:,1] #unit cell volumes of AGO DAC A


#define Birch-Murnaghan equation of state
def BM_(V, K0, V0): #let K0 and V0 vary
    P = (3/2)*K0*((V0/V)**(7/3) - (V0/V)**(5/3))
    return P

#do the fitting
all2_popt, all2_pcov = curve_fit(BM_, all_vols, all_press, p0=[199,209],
maxfev=10**6)#bounds=([1,208], [np.inf,212]))
print("fit to all: parameters are [K0, V0]")
print(all2_popt)

#To compute one standard deviation errors on the parameters use
perr = np.sqrt(np.diag(all2_pcov))
print("errors are")
print(perr)
print("\n")


#plot the data
volumes=np.linspace(0.00001,500,100)

#plot the measured data
plt.scatter(0,210.248, marker="s", s=90, c="orange", label="ambient")
plt.scatter(AGOinc_pressures, AGOinc_vols, marker="o", s=90, edgecolor="blue",
facecolor="blue", label="AGO Run 1") #run 1
plt.scatter(AGOdec_pressures, AGOdec_vols, marker="o", s=90, edgecolor="blue",
facecolor="none")
plt.scatter(AAGOinc_pressures, AAGOinc_vols, marker="o", s=90, edgecolor="green",
facecolor="green", label="AGO Run 2")
plt.scatter(AAGOdec_pressures, AAGOdec_vols, marker="o", s=90, edgecolor="green",
facecolor="none")
```

```
#plot the fitted curve
plt.plot(BM_(volumes, *all2_popt), volumes, 'k-',linewidth=2, label="EoS fit")

#everything below here affects how the plot looks
plt.xlim(0, 8)
plt.ylim(201,212)
plt.ylabel(r"Unit cell volume $\AA^3$")
plt.xlabel("Pressure (GPa)")
plt.legend()
font = {'weight' : 'normal', 'size'   : 18}
matplotlib.rc('font', **font)
matplotlib.rcParams['axes.linewidth'] = 3
plt.tick_params(which='major',
direction='in',length=10,width=2,top=True,bottom=True,left=True,right=True)
plt.tick_params(which='minor',
direction='in',length=5,width=1,top=True,bottom=True,left=True,right=True)
plt.legend(loc="upper right",frameon=False)
plt.minorticks_on()
plt.rcParams["figure.figsize"] = (7,7)
#plt.text(x=0,y=190, s=r"fit params: K$_0$=%5.3f, V$_0$=%5.3f" % tuple(all_popt))
plt.rcParams["figure.figsize"] = (7,7)
plt.savefig(r"C:\filepath\041823_AGO_EoS.eps",bbox_inches='tight', dpi=300)
plt.show()
```

C.2 *R* line intensity ratio fitting

```
#Nonlinear curve fit to R2/R1 intensity area ratio versus temperature or pressure
import matplotlib.pyplot as plt
import matplotlib
import numpy as np
import scipy.constants as sp
from scipy.optimize import curve_fit


#import AGO and Ga2O3 raw data with intensity ratios (r2/r1)
A_nparray=np.loadtxt(r"C:\filepath\AGO_intensity_ratios.csv", delimiter=',',
skiprows=1)
aTs=A_nparray[:,0] #temperature in kelvin (independent variable)
aER1=A_nparray[:,1] #energy of R1
aIR1=A_nparray[:,2] #intensity of R1/R2
aER2=A_nparray[:,3] #energy of R2
aIR2=A_nparray[:,4] #intensity of R2/R1 (this is the data we are fitting to)
```

```
aerr=A_nparray[:,5] #error bars on intensity ratio of R2/R1

G_nparray=np.loadtxt(r"C:\filepath\GaO_intensity_ratios.csv", delimiter=',',
skiprows=1)
gTs=G_nparray[:,0] #temperature in kelvin (independent variable)
gER1=G_nparray[:,1] #energy of R1
gIR1=G_nparray[:,2] #intensity of R1/R2
gER2=G_nparray[:,3] #energy of R2
gIR2=G_nparray[:,4] #intensity of R2/R1 (this is the data we are fitting to)
gerr=G_nparray[:,5] # error bars on intensity ratio R2/R1


#define boltzmann constant and temperature fit functions
k=sp.physical_constants["Boltzmann constant in eV/K"][0]

def newfit(T,A,A1,A2,E1,E2):
    #A*exp(-E/x)*(1+A1*exp(-E1/x))/(1+A2*exp(-E2/x))
    #the fit parameters already include k (boltzmann constant) so x=T. i.e. E =
230 K *kB = 19.82 meV
    #E=230 (fixed)
    return (A*np.exp(-230/T))*(1+(A1*np.exp(-E1/T)))/(1+(A2*np.exp(-E2/T)))

def thermalpop(T,A):
    return A*np.exp(-230/T)

#define pressure fit equations
def newfit_GaO(P,A,B,C): #use this one
    E = 0.01841 + 0.00147*P #fit to linear peak splitting (experimental)
    E1= 0.0593 + B*P #values for GaO from reference fit with temperature
    E2= 0.0166 + C*P
    #A=63.6
    A1=9.9
    A2=50.2
    return (A*np.exp(-E/(k*295)))*(1+(A1*np.exp(-E1/(k*295))))/(1+(A2*np.exp(-
E2/(k*295))))

def newfit_AGO(P,A,B,C): #use this one
    E = 0.01841 + 0.00147*P
    E1= 1.3*10**-8 + B*P #1.3*10**-8 + B*P #values for GaO from reference fit
with temperature
    E2= 0.0065 + C*P #0.0065 + C*P
    #A=31.9
    A1=37.4 #37.4
```

```
    A2=302.3 #302.3
    return (A*np.exp(-E/(k*295)))*(1+(A1*np.exp(-E1/(k*295))))/(1+(A2*np.exp(-
E2/(k*295))))


#do the fitting and plot the results
temps=np.linspace(0.00001,300,100)

plt.errorbar(aTs,aIR2,yerr=aerr,fmt='s', color='black',elinewidth=0.5,capsize=3)
plt.errorbar(gTs,gIR2,yerr=gerr,fmt='o', color='red',elinewidth=0.5,capsize=3)

#Constrain the fit:
guesses=[38,21,24,330,330]
#add maxfev=10**6 into the curve_fit parameters to increase max number of
iterations if needed (doesn't work with bounds)

#fit AGO
a2popt, a2pcov = curve_fit(newfit, aTs, aIR2, p0=[38,21,24,330,330], bounds=(0,
np.inf))
plt.plot(temps, newfit(temps, *a2popt), 'k-',linewidth=1.5)
print('AGO R2/R1 fit: A=%5.5f, A1=%5.5f, A2=%5.5f, E1=%5.5f, E2=%5.5f' %
tuple(a2popt))
print("AGO error matrix:")
print(a2pcov) #errors on fit parameters are the diagonal of the error matrix

#fit Ga2O3
g2popt, g2pcov = curve_fit(newfit, gTs, gIR2, p0=guesses, bounds=(0, np.inf))#(1,
[100, 30, 100,700, 700]))
plt.plot(temps, newfit(temps, *g2popt), 'r-',linewidth=1.5)
print('Ga2O3 R2/R1 fit: A=%5.5f, A1=%5.5f, A2=%5.5f, E1=%5.5f, E2=%5.5f' %
tuple(g2popt))
print("Ga2O3 error matrix:")
print(g2pcov)

#plot real data points
plt.scatter(gTs,gIR2, marker='o',color='red',label=r"Ga$_2$O$_3$")
plt.scatter(aTs,aIR2, marker='s',color='black',label="AGO")

#plot thermal population line only
plt.plot(temps, thermalpop(temps,g2popt[0]), "r--")#, label="GaO thermal pop.")
plt.plot(temps, thermalpop(temps,a2popt[0]), "k--")#, label="AGO thermal pop.")
```

```
#everything below here is for the formatting of the plot
font = {'weight' : 'normal',
        'size'   : 18}
matplotlib.rc('font', **font)
plt.tick_params(which='major',direction='in',length=10,width=2,top=True,bottom=Tr
ue,left=True,right=True)
plt.tick_params(which='minor',direction='in',length=5,width=1,top=True,bottom=Tru
e,left=True,right=True)
plt.xlabel("Temperature (K)")
plt.ylabel(r"Intensity ratio (R$_2$/R$_1$)")
plt.legend(loc="lower right",frameon=False)
plt.minorticks_on()
plt.text(y=-0.65,x=5,fontsize=10,s='AGO fit: A=%5.2f, A1=%5.2f, A2=%5.2f,
E1=%5.2f, E2=%5.2f\n' % tuple(a2popt)+'GaO fit: A=%5.2f, A1=%5.2f, A2=%5.2f,
E1=%5.2f, E2=%5.2f' % tuple(g2popt))
plt.xlim(left=0)
plt.ylim(0,3)
plt.rcParams["figure.figsize"] = (7,7)

#save the figure to the location at this filepath
plt.savefig(r"C:\filepath\101122_both_newfit.png",bbox_inches='tight', dpi=300)
plt.show()
```